In-Situ observation of New Particle Formation (NPF) in the tropical tropopause layer of the 2017 Asian Monsoon Anticyclone - Part I: summary of StratoClim results

Ralf Weigel[1], Christoph Mahnke[2, 8], Manuel Baumgartner[1,3], Antonis Dragoneas[1,2], Bärbel Vogel[4], Felix Ploeger[4], Silvia Viciani[5], Francesco D'Amato[5]; Silvia Bucci[6], Bernard Legras[6], Beiping Luo[7], and Stephan Borrmann[1, 2]

[1]Institut für Physik der Atmosphäre, Johannes Gutenberg Universität, Mainz, Germany
[2]Partikelchemie, Max-Planck-Institut für Chemie, Mainz, Germany
[3]Zentrum für Datenverarbeitung, Johannes Gutenberg University, Mainz, Germany
[4]Institute of Energy and Climate Research (IEK-7), Forschungszentrum Jülich, Jülich, Germany
[5]National Institute of Optics - National Research Council (CNR-INO), Florence, Italy
[6]Laboratoire de Météorologie Dynamique, UMR 8539, CNRS – École Normale Spérieure / Université Pierre et MarieCurie / École Polytechnique, Paris, France
[7]Swiss Federal Institute of Technology, Institute for Atmospheric Science, ETH Zurich, Switzerland
[8]now at the Institute of Energy and Climate Research (IEK-8), Forschungszentrum Jülich, Jülich, Germany

Correspondence to: R. Weigel (weigelr@uni-mainz.de)

Abstract

During the monsoon season of the year 2017 the airborne StratoClim mission took place in Kathmandu, Nepal with eight mission flights of the M-55 *Geophysica* in the upper troposphere / lower stratosphere (UT/LS) of the Asian Monsoon Anticyclone (AMA) over northern India, Nepal and Bangladesh. More than hundred events of New Particle Formation (NPF) were observed. In total, more than two hours of flight time were spent under NPF conditions as indicated by the abundant presence of nucleation-mode aerosols, i.e. with particle diameters d_p smaller than 15 nm, which were *in-situ* detected by means of condensation nuclei counting techniques. Mixing ratios of nucleation-mode particles (n_{nm}) of up to ~ 50000 mg^{-1} were measured at heights of 15 – 16 km ($\theta \approx 370$ K). NPF was most frequently observed at ~ 12 - 16 km altitude ($\theta \approx 355$ – 380 K) and mainly below the tropopause~~,~~. Resulting~~but~~ n_{nm} remained elevated (~ 300 – 2000 mg^{-1}) up to altitudes of ~ 17.5 km ($\theta \approx 400$ K) while under NPF conditions the fraction (f) of submicrometre-sized non-volatile~~ particle~~ residues ($d_p > 10$ nm) remained below 50 %. At ~ 12 - 14 km ($\theta \approx 355 – 365$ K) the minimum of f (< 15 %) was found, and underneath, the median f generally remains below 25 %. The persistence of particles at nucleation-mode sizes is limited to a few hours, mainly due to coagulation, as demonstrated by a numerical simulation. ~~Thus, NPF is detectable only for a limited period of time and~~ The frequency of NPF events observed during StratoClim 2017 underlines the importance of the ~~UT/LS within the~~ AMA as a source region for UT/LS aerosols and for the formation and maintenance of the ATAL~~aerosols. The effective *in-situ* production of aerosol in the tropopause region and subsequent coagulation and/or condensation likely contribute to the formation and maintenance of the Asian~~

~~Tropopause Aerosol Layer (ATAL)~~. The observed abundance of NPF-produced nucleation-mode particles within the AMA is not unambiguously attributable to (a) specific source regions in the boundary layer (according to backward trajectory analyses), or (b) the direct supply with precursor material by convective updraught (from correlations of NPF with carbon monoxide), or (c) the recent release of NPF-capable material from the convective outflow (according to air mass transport times in the TTL). Temperature anomalies with ΔT of 2 K (peak-to-peak amplitude), as observed at a horizontal wavelength of ~ 70 - 100 km during a level flight of several hours match with NPF detections and represent an a~~lternative~~dditional mechanism for local increases in supersaturation of the NPF precursors. Effective precursor supply and widely distributed temperature anomalies within the AMA can explain the higher~~The~~ frequency of intense NPF observed during StratoClim 2017 ~~exceeds~~ than all previous NPF detections with COPAS at TTL levels over Brazil, Northern Australia, or West Africa. ~~The observed NPF abundance and productivity of fresh aerosols during StratoClim 2017 indicates that NPF is capable of directly affecting the extent and persistence of the ATAL.~~

1. Introduction

Aerosol particles in the upper troposphere / lower stratosphere (UT/LS) influence the radiative balance of the Earth's atmosphere, stratospheric ~~ozone~~ chemistry, and properties of cirrus clouds near the tropopause (Kremser et al., 2016). UT/LS aerosols are mainly composed of sulphuric acid (H_2SO_4), nitric acid (HNO_3), water (H_2O), and organic compounds. Additionally, the particles include fractions of non-volatile (or refractory) material (e.g. ~~Murphy et al. (1998); Murphy et al. (2006); Curtius et al. (2001); Heald et al. (2005);~~ Froyd et al. (2010); Borrmann et al. (2010); Murphy et al. (2014); Schneider et al. (2020)). Non-volatile components of stratospheric aerosol particles originate from (1) natural tropospheric sources, e.g., volcanoes, biomass burning, or pyro-cumulonimbus, (2) from meteoric ablation, or (3) they are anthropogenic, as, for instance, space debris, rocket exhaust fumes, and products from combustion (Kremser et al. (2016)). Chemical and microphysical processes, which involve the stratospheric aerosol, could be influenced by solutes that, e.g., had previously been constituents of the refractory aerosol compounds. Soot, mineral dust, fly ashes, metal-containing condensates ~~aerosol from biomass combustion, meteoric ablation material,~~ inorganic salts, and other species probably make up the largest share of the non-volatile components of aerosol particles in the UT/LS. In the tropics, underneath the tropopause, the number of non-volatile fine-mode particles (i.e. smaller than 1 µm and larger than 10 nm in diameter d_p) typically exhibits a

characteristic minimum, resulting in a fraction of ~ 20 % (and less) of non-volatile aerosol particles (cf. Borrmann et al. (2010); Weigel et al. (2011)). Above the tropopause, at potential temperatures greater than 390 - 400 K, a maximum contribution of non-volatile aerosol constituents seldom exceeds 50 % (*ibid.*). Schneider et al. (2020) recently provided laser ablation mass spectrometric analyses of refractory particles in the LS region between the equator and the Arctic, which indicate detectable signatures of meteoric ablation material at all sample locations in the LS. They assume that the meteoric ablation material is partly present as solute or as insoluble inclusion within stratospheric H_2SO_4-H_2O-droplets.

In general, the typical particle size distribution of the stratospheric aerosol is characterised by processes such as formation of new particles and their coagulation, the condensation of saturated vapours, and the evaporation as well as removal ~~from the stratosphere into the troposphere~~when largest particles sediment. In the tropics, above the level of zero net radiative heating where scavenging is lacking in the absence of clouds, aerosol particles are available for isentropic dispersion or upward transport into the stratosphere. Sedimentation or isentropic transport and mixing remove particles from the stratosphere (Thomason and Peter (2006); Kremser et al. (2016)). Moreover, the aerosol removal from the stratosphere occurs with particular efficiency via large-scale air mass subsidence in the polar winter vortex in both, the Arctic (Weigel et al., 2014) and the Antarctic (Campbell and Deshler, 2014).

The process of ~~homogeneous nucleation (also known as gas-to-particle-conversion), herein referred to as~~ New Particle Formation (NPF), is considered as one of the most important sources of the H_2SO_4-H_2O solution droplets prevailing in the UT and Tropical Tropopause Layer (TTL) (Brock et al., 1995). The reservoir of stratospheric H_2SO_4 is maintained by oxidation of gaseous precursors like sulphur dioxide (SO_2), carbonyl sulphide (OCS), and carbon disulphide (CS_2), or dimethyl sulphide (C_2H_6S) (Thomason and Peter (2006); Kremser et al. (2016)). These species can originate from sea surface emissions, from volcanism or from anthropogenic pollution, and they often undergo long range transport before reaching the TTL (e.g. Law et al., 2010). Sporadically, explosive volcanism injects large quantities of SO_2 directly into the stratosphere. Weaker volcanic eruptions (with a mean vertical explosion index of about four) also contribute significantly by delivering volcanic sulphur species indirectly via the TTL into higher altitudes (Vernier et al. (2011b); Kremser et al. (2016)). ~~Within the planetary boundary layer, SO_2 is found~~

~~in mixing ratios from 20 pmol mol^{-1} to more than 1 nmol mol^{-1}. SO_2 mixing ratios of up to several hundreds of nmol mol^{-1} are found in the vicinity of cities and highly polluted areas (Seinfeld and Pandis, 2016). From the boundary layer, SO_2 can be transported very efficiently by deep convection within cumulonimbus (Cb) clouds to UT heights.~~ Although SO_2 is efficiently bound within clouds during convective uplift and dissolved in cloud hydrometeors, cloud-resolving model calculations suggest that ~~a~~ SO_2 proportions, which range from only 30 % (Ekman et al., 2006) until up to ~~of~~ 40-90 % ~~of SO_2~~(Barth et al., 2001), ~~may~~ reach the outflow region of deep convection ~~(Barth et al., 2001), and these calculations are~~ largely consistent with estimates by Crutzen and Lawrence (2000)~~. However, other model studies (Ekman et al., 2006) show that only 30 % of SO_2 from the boundary layer reaches the cloud top~~. Laboratory investigations by Jost et al. (2017) yielded a comparatively moderate retention coefficient (0.2 – 0.5) of SO_2 in the ice phase of clouds, compared to a retention of 100 % for hydrochloric acid (HCl) and for nitric acid (HNO_3) (*ibid.*). Hence, large fractions of the in-cloud dissolved SO_2 leave the cloud ice composite as soon as the cloud particles freeze or when riming occurs. Alternatively, the SO_2, which remains in the cloud ice composite, is entirely released when the ice particles sublimate in the convective outflow region, or below, while the ice particles sediment. ~~Crutzen and Lawrence (2000), as well as Barth et al. (2001), however, clarified that cloud's acidity determines its capacity to remove a soluble gas (such as SO_2). Results from airborne *in-situ* measurements of SO_2 at altitudes between 8 and km were compiled by Thornton et al. (1999). Remote MIPAS observations were compared by Höpfner et al. (2015) with SO_2 data from *in-situ* measurements between 8 and 12 km altitude, which were carried out before the year 2001.~~ Rollins et al. (2017) presented the results of *in-situ* SO_2 measurements at up to 19 km altitude over the Gulf of Mexico and compared these with both model results and satellite observations. Generally, a~~A~~t altitudes between 8 and 15 km, the mean values of SO_2 mixing ratio vary between 5 and 800 pmol mol^{-1} in the northern hemisphere, between 8 and 120 pmol mol^{-1} in the tropics, and between 5 and 20 pmol mol^{-1} in the southern hemisphere (Kremser et al., 2016). Enhanced SO_2 mixing ratios in the vicinity of the tropopause are often observed in connection with the uplift of polluted air masses by Warm Conveyor Belts (WBC) (*ibid.*). Apart from sulphuric acid, ~~potentially~~ also other species contribute to particle nucleation and growth, such as organics (Metzger et al. (2010); Kerminen et al. (2010)), amines (Kürten et al. (2018)) or ammonia (e.g. Kirkby et al. (2011); Kürten (2019)). Given the amount of organics (Murphy et al. (2006)) and ammonia species

(Höpfner et al. (2019); Stroh and the StratoClim group (2021)), which were found in aerosol particles at UT/TTL heights in the AMA during the StratoClim 2017 mission, such compounds can act as agents promoting NPF in the UT and TTL region.

1.1 New particle formation

New Particle Formation (NPF), comprises (1) the initial combination of molecules into clusters (of ~ 1 nm diameter) and (2) their subsequent growth to larger diameters (Kulmala et al., 2013). Nucleation mode ~~(ultrafine)~~ aerosol particles with diameter (d_p) of at least 3 nm frequently form in considerable quantities from gaseous precursors. Once formed, the particles are subject to altering processes (e.g. coagulation, growth by condensation of water vapour and other gases, evaporation, and scavenging). Within the entire atmosphere, NPF seems ubiquitous as was demonstrated by various studies and observations of NPF's occurrence:

- at or close to the surface (Kulmala et al. (2004); Nieminen et al. (2018)),
- at elevated altitudes within the boundary layer (e.g. Bianchi et al. (2021); Sellegri et al. (2019); ~~-~~Wehner et al. (2015), Crumeyrolle et al. (2010); Venzac et al. (2008)),
- in the boundary layer and in the free troposphere under the direct influence by volcanic activity (e.g. Sahyoun et al. (2019)),
- up to tropopause altitudes and the TTL region (Kerminen et al. (2018); Williamson et al. (2018); Williamson et al. (2019).

Modelling studies suggest that the NPF process constitutes one of the most important contributions (up to 45 %) to global mean tropospheric concentrations of Cloud Condensation Nuclei (CCN) activated at 0.2 % supersaturation (Merikanto et al., 2009). Uncertainties remain concerning the effectiveness of NPF, which complicates the implementation of the NPF mechanism in global scale simulations of aerosol number densities (Yu et al. (2010), Zhang et al. (2010)). Chamber experiments, conducted at temperatures similar to those prevailing in the UT, and also numerical simulations ~~also~~ confirm that the UT constitutes an important source region for atmospheric particles (Kürten et al. (2016), Dunne et al. (2016)).

Based on airborne *in-situ* observations of high particle number concentrations together with high levels of particle volatility in the cloud-free tropical UT, the conditions of NPF occurrence were described for the first time by Brock et al. (1995). Between 7 and 20 km altitude, fields of

recent NPF events were encountered in about 20 % of the probed flight segments (Lee et al. (2004)). High NPF productivity with ~~of~~ largest ~~*intensity*~~ n_{nm} was observed particularly at the bottom TTL, as shown by airborne measurements during missions over Brazil and over North Australia (Weigel et al. (2011)). Recently, a survey of NPF occurrence in the free troposphere (~ 0.2 - 12 km altitude) suggests that the NPF-produced particles persist (zonally almost invariant) as a globally extending band within the tropical UT, thereby covering 40 % of the Earth's surface (Williamson et al., 2019). At altitudes between 12 and 20 km within the tropics, this had also been reported by Borrmann et al. (2010).

Between 27 July and 10 August 2017, during the Asian monsoon season, a total of eight scientific flights with the high-altitude research aircraft M-55 *Geophysica* over parts of the Indian subcontinent were performed from Kathmandu, Nepal (27° 42' 3'' N, 85° 21' 42'' E) during the StratoClim 2017 mission (see Figure 1, and see also Stroh and the StratoClim group (2021)). Some of these flights partly spanned out of Nepalese airspace, to East India, Bangladesh, and to the northern part of the Bay of Bengal. During StratoClim 2017, NPF was frequently observed in the presence of ice cloud particles within cirrus or in anvils of the convective outflow and is discussed in detail in the companion paper (Weigel et al., 2021b). Based on these observations during StratoClim 2017, NPF turned out as largely unaffected by faint ice clouds that typically occur in TTL (*ibid.*). This study aims at discussing the NPF encounters in their entirety as observed during the StratoClim 2017 mission ~~(Weigel et al., 2020b)~~in the UT and TTL region at altitudes of up to 20 km in the Asian Monsoon Anticyclone.

1.2 The Asian Monsoon Anticyclone and the ATAL

The Asian Monsoon Anticyclone (AMA) represents one of the most important circulation systems in the UT/LS~~, mostly~~ associated with deep convection~~, which mainly determines the circulation in the UT/LS during the monsoon season~~ over the Indian subcontinent and beyond. From the beginning of June until about the end of August, the large-scale anticyclone persists at altitudes from the UT to the LS regions (e.g. Randel and Park (2006), Park et al. (2007)), extending over longitudes from East Asia to the Middle East/ East Africa (e.g. Vogel et al. (2014), Vogel et al. (2019)). The anticyclonic rotation of the system induces confinement of air inside the AMA's interior ~~induces a horizontal transport barrier inside the UT/LS~~ (Ploeger et al. (2015))~~,~~ ~~which abates the isentropic exchange between the AMA's interior and its surrounding~~. Air

masses in the region of the Asian monsoon are rapidly lifted by convection up to the maximum level of convective outflow (~ 360 K, corresponding to ~ 13 km) followed by a slow diabatic lift superimposed on the anticyclonic motion (e.g. Vogel et al. (2019)). ~~This mechanism~~Within the AMA ~~transports,~~ young air is transported to UT/LS altitudes during boreal summer and in this way various pollutants and other gaseous material (Glatthor et al. (2015); Chirkov et al. (2016); Pan et al. (2016); Santee et al. (2017)) and in particular water vapour (Ploeger et al. (2013)) are lifted into the UT/LS region ~~within the AMA~~. Based on satellite studies, the existence of the aerosol layer at tropopause altitudes within the AMA region (ATAL – Asian Tropopause Aerosol Layer) was ~~proven and investigated~~demonstrated (Vernier et al. (2011a); Thomason and Vernier (2013)). The existence of the ATAL ~~is~~ was further confirmed by *in-situ* balloon-borne backscatter measurements between 2013 and 2017 at different locations nearby the AMA centre (Vernier et al. (2015); Vernier et al. (2018); Brunamonti et al. (2018); Hanumanthu et al. (2020)) ~~as well as recently by~~and recent aircraft measurements of Mahnke et al. (2021) or Fujiwara et al. (2021).

Hence, the constituents of the rising young air ~~may~~ also include precursor material from anthropogenic (Vernier et al. (2015), Yu et al. (2015)) and other sources~~, which maintain the observed ATAL.~~ The NPF process in the TTL region could contribute significantly to the formation and persistence of ATAL as a source of additional aerosol material (He et al., 2019). Once the boundary layer material has reached UT/LS levels within the AMA, the elevated tropopause potential temperature during the monsoon season allows the material's isentropic dispersion into the "overworld" stratosphere (Pan et al. (2016)). ~~Thereby, it is under debate whether the upward transport is best described with the model of a draughting "chimney" or of a pushing "blower" (Pan et al. (2016)). However, t~~Three-dimensional simulations with the Chemical Lagrangian Model of the Stratosphere (CLaMS) and backward trajectory analyses show that by end of August, during the 2008 monsoon season, ~~comparatively young~~ air masses ~~(~~younger than 6 months~~)~~ reach the top of the AMA at about 460 K potential temperature (corresponding to ~ 60 hPa). According to these simulations (Vogel et al. (2019)), air masses are lifted due to diabatic (~~mainly~~ radiative) heating in an anticyclonic large-scale upward spiral with ascent rates of about 1 K potential temperature per day~~. The anticyclonic lift of air in the AMA occurs~~ across the tropopause ~~while elsewhere, in the extra-tropics, the tropopause typically acts as an obstacle for the immediate vertical transport (Vogel et al. (2019)). This capability of the~~

~~tropopause to cap the troposphere seems largely diminished in connection with the AMA (*ibid.*), and is~~ consistent with the conclusions of previous works (Bergman et al. (2012), Garny and Randel (2016), Ploeger et al. (2017)).

2 *In-situ* instrumentation

2.1 Total number concentration of sub-micrometre sized particles

Particle number concentrations were *in-situ* measured in 1 Hz resolution by means of a 4-channel condensation nuclei (CN) counter COPAS (COndensation PArticle counting System, cf. Weigel et al. (2009)). For reduction of the statistical noise, the COPAS 1 Hz-raw data (direct signal of the scattered-light-detectors) are preprocessed by applying a 15-second running average. Three of the four COPAS channels operate with different 50 % detection particle diameters d_{p50} (i.e. 6 nm, 10 nm and 15 nm). The fourth COPAS channel (with d_{p50} = 10 nm) detects particles downstream of a heated (270°C) sample flow line, resulting in measured particle mixing ratios of non-volatile (nv) particle residues or refractory particles (e.g. soot, mineral dust, metallic particle material, etc.).

2.1.1 COPAS operation during StratoClim 2017

The sampling is carried out via the forward facing aerosol inlet of COPAS well outside the boundary layer of the aircraft. For stratospheric particle concentrations, the COPAS measurement uncertainty of the StratoClim 2017 data discussed herein is about 15%, which is due to particle counting statistics and uncertainties in the volume flow. The measurement properties of COPAS are described in detail by Weigel et al. (2009), and its performance has been demonstrated by several studies (Curtius et al. (2005); de Reus et al. (2009); Borrmann et al. (2010); Frey et al. (2011); Weigel et al. (2011), and Weigel et al. (2014)).

For StratoClim 2017, a new inlet configuration was used, allowing both COPAS instruments to sample through a single aerosol inlet, resulting in an almost doubled flow velocity through the sample tubes and reduced diffusional particle loss. This setup required the reanalysis of the corrections to account for particle loss (

Table 1) using the method introduced by von der Weiden et al. (2009) with modifications for low-pressure application. One of the four COPAS channels detects particle number densities of

non-volatile particle residues downstream of a heated stainless steel tube (at ~270°C) (Appendix A)

~~2.1~~2.1.2 NPF identification: definitions and notations

~~Particle number concentrations were *in-situ* measured by means of a 4-channel condensation nuclei (CN) counter COPAS (COndensation PArticle counting System, cf. Weigel et al. (2009)) with continuous flow, using the chlorofluorocarbon FC-43 as working fluid. COPAS measurements and data storage are performed at a frequency of 1 Hz. To reduce the statistical noise of the directly recorded raw signal of the scattered-light-detectors integrated in COPAS, the 1 Hz raw data are preprocessed by applying a 15-second running average. Three of the four COPAS channels operate with different 50 % detection particle diameters d_{p50} (i.e. 6 nm, 10 nm and 15 nm). The fourth COPAS channel (with d_{p50} = 10 nm) detects particles downstream of a heated (270°C) sample flow line, resulting in measured particle mixing ratios of non-volatile (nv) or refractory particles (e.g. soot, mineral dust, metallic material, etc.).~~

~~COPAS operation during StratoClim 2017~~

~~The forward facing aerosol inlet of COPAS is located well outside the boundary layer of the aircraft. The inlet consists of two serial diffusers, which slow down the ambient air velocity to the flow speed of the instruments' sampling. For stratospheric particle concentrations, the COPAS measurement uncertainty of the StratoClim 2017 data discussed herein is about 15%, which is due to particle counting statistics and uncertainties in the volume flow. The measurement properties of COPAS are described in detail by Weigel et al. (2009), and its performance has been demonstrated by several studies (Curtius et al. (2005); de Reus et al. (2009); Borrmann et al. (2010); Frey et al. (2011); Weigel et al. (2011), and Weigel et al. (2014)). Compared to previous missions (*ibid.*), during StratoClim 2017 a new inlet configuration was required, which caused both COPAS instrument units to sample via a single aerosol inlet.~~

~~, which effectively reduces diffusional particle loss (cf. Weigel et al. (2009)). However, this new instrument setup required a reanalysis of the corrections to account for particle loss as compared to the previous values documented in (Weigel et al. (2009)). Equivalently to the previously described procedure (*ibid.*), the pressure-dependent corrections for the used aerosol lines and given volume flows were re-calculated (Table 1) using the method introduced by von der Weiden et al. (2009) with modifications for low-pressure application. These corrections are applied to the number densities of particles (cf. Section 2.1.3).~~

~~COPAS detection of non-volatile (refractory) aerosol particles~~

~~COPAS includes a denuder-type device based on an established and commonly used technique for exposing atmospheric aerosol samples to heat in order to obtain indications concerning the chemical properties a) of the volatile compounds of aerosol particles (when analysed e.g. by gas chromatography) or b) of the remnants, which survive the heat exposure. One of the four COPAS channels is equipped with a heated stainless steel tube, which is used to vaporise volatile compounds upstream of one of the particle detectors. In this way, the preheated COPAS channel detects the residual aerosol component by number per sample volume. The particles that remain after passing through the heated tube (at ~ 270°C) are considered and designated hereafter as non-volatile (or refractory) at given temperature (see Curtius et al. (2005), Weigel et al. (2009), and Borrmann et al. (2010)). The specific heating temperature is chosen with the aim to vaporise mainly stratospheric particle species, which typically consist of aqueous solutions of acid (H_2SO_4-H_2O) and/or nitric acid (HNO_3-H_2O), which reportedly volatilise at 180°C (Rosen, 1971). In addition, most of volatile and several semi-volatile organic compounds can evaporate at temperatures below 270°C. Kurtén et al. (2008)Riccobono et al. (2014)Tang et al. (2014)~~

~~The working principle of the COPAS aerosol vaporiser was demonstrated by means of laboratory experiments with pure H_2SO_4-H_2O particles of several sizes and at pressure conditions between 70 – 300 hPa (Weigel et al., 2009); more than 98 % of the sub-micrometre sized H_2SO_4-H_2O particles were volatilised. As refractory material, which could be detectable with COPAS, is unlikely to be generated by the heater itself, instrumental artefacts may be excluded as a potential cause of false observation. To avoid artefacts as a result, e.g., of re-suspension of aerosol material, which had been deposed on the tube's inner walls during previous operations, the sample lines were flush-cleaned with ethanol and distilled water, at least before every second mission flight. Inefficiencies of the vaporiser, e.g. due to diminished heat transfer from the tube's inner wall to the passing aerosol particles, particularly at low atmospheric pressures, would cause the number (fraction) of detected refractory particles to be unexpectedly high (f ≈100 %) over extended measurement periods, which was not observed throughout the field missions (cf. Borrmann et al. (2010); Weigel et al. (2011)). Conversely, instrumental artefacts inherent with the vaporiser's tube length, e.g. particle loss, would lead to comparatively low number concentrations of detected refractory particles. Diffusional loss effects increase with decreasing pressure, but thermophoresis should counteract the particles' diffusion towards the hot tube walls. With the same vaporiser system, Weigel et al. (2014) observed rising mixing ratios of refractory aerosol, most likely from meteoric ablation, with altitude at stratospheric levels inside the polar vortex, while outside the vortex the amount of refractory aerosols nearly stagnated over the corresponding altitude range. This may additionally confirm the principle function of the vaporiser.~~

~~NPF criterion and event definition~~The particle densities are typically measured by COPAS in particle number concentrations N (in cm^{-3}, ambient conditions), but are also presented here as mixing ratio n in units of particles per milligram of air (mg^{-1}) for consistent comparisons of measurements from different pressure levels and for correlations with the mixing ratios of gaseous tracers. Hereafter, the notation n_{10} refers to the mixing ratio of sub-micrometre sized particles with diameters greater than 10 nm. The measurement of n_6 (of particles with $d_p > 6$ nm) and n_{15} ($d_p > 15$ nm) allows for the identification of recent NPF. The notation n_{10}nv refers to the mixing ratio of non-volatile particles (Appendix A) with corresponding size range as specified for n_{10}. The proportion f of non-volatile particles is given as the ratio $\frac{n_{10}\mathrm{nv}}{n_{10}}$ in percent.

~~To serve as an indication of recent NPF (within hours prior to the observation),~~ Elevated ~~the~~ number concentrations N_{nm} of nucleation-mode particles ~~(hereafter referred to as N() results from the difference~~ defined as $N_6 - N_{15} = N_{6\text{-}15}$) ~~–~~serve as an indication of recent NPF when additionally ~~which moreover requires the meeting the~~ NPF criterion (Equ. 1) is met:

$$0.8 \cdot N_6 - 1.2 \cdot N_{15} > 0\,. \qquad (1)$$

This criterion was reassessed for the StratoClim 2017 data set based on the definition used by Weigel et al. (2011) to account for the COPAS detectors' signal-to-noise ratio and the counting statistics. The NPF criterion therefore sets a conservative threshold (*ibid.*) that additionally accounts for the full range of data scattering (i.e. 20 % over periods of invariable N ~~per at least 15 data points~~) that exceeds the 15 % uncertainty of the concentrations measured with COPAS. The strict criterion suppresses artificial features that mainly result from the scattering of the measured concentrations and the criterion constrains the data set to the most significant of those that were interpreted as NPF events~~The NPF criterion therefore sets a conservative threshold (*ibid.*) to take an overall uncertainty of up to 15 % of the individual COPAS channels into account~~. ~~Resulting~~ Calculated $N_{6\text{-}15}$ are then ~~subject to corrections~~corrected concerning particles' diffusional loss inside the aerosol lines as described in Section 2.1.1~~Section 2.1.1~~ (cf. also Table 1~~Table 1~~). The calculated number concentrations $N_{6\text{-}15}$ are corrected by multiplying the factor κ_L (Table 1~~Table 1~~), which is a function of the static pressure during the measurements.

Provided that the NPF criterion is met, a series of measurement points is denoted as ~~an~~ NPF event if the measured number concentration (or mixing ratio) of nucleation-mode particles remains continuously greater than zero for at least ~~5~~ five ~~measurement~~ seconds of measurement. ~~Limitations of this event definition concern observations.~~ In total, 25 cases out of 130 individual events had a duration of less than five seconds, therefore for these 25 the number of newly formed particles and the feature duration are uncertain~~Overall,~~. Mainly those features that are much too short (e.g. lasting only one second) are filtered out by applying the NPF event definition ~~Note, during one second the measurement platform has moved a horizontal distance of ~ 150 m and a vertical distance of up to ~ 10 m assuming cruising speed and a maximum ascent/descent rate of 10 m s^{-1}~~. Based on the mean airspeed and maximum ascent/descent rates of the M-55 *Geophysica* (~ 154 ± 39 m s^{-1}; up to 10 m s^{-1}), this definition implies that a feature of

elevated N_{nm} lasting over five seconds extends over a horizontal distance of ~ 770 m (at constant course) or vertically over up to 50 m. ~~The corresponding event definition applies also for investigations concerning the occurrence of NPF in the presence of cloud ice elements during the StratoClim 2017 mission (see Weigel et al. (2020b)).~~

~~The time period during which the event criterion (Equation 1) is fulfilled, i.e. during which the number of ultrafine particles remains at significantly elevated levels,~~ The period of flight time during which the event criterion (Equation 1) is met is referred to ~~hereafter~~ as the NPF event duration. From this ~~primary~~ information ~~of measured data~~, the mean airspeed is used to infer the horizontal extent of NPF fields - with caveats. ~~the horizontal extent of NPF fields is derivable with caveats. On the one hand, s~~Such estimates are limited by the assumption that an encounter of elevated N_{nm} (over tens of seconds and minutes) is actually due to a single NPF event and does not consist of a series of possibly overlapping events. ~~On the other hand~~In addition, the determined horizontal distances refer to ~~the~~ an average flight speed (~ 154 ± 39 m s^{-1}) and the flight attitude is assumed as unchanged during the event duration.

NPF events are distinguished by the peak number density of detected nucleation-mode particles and~~NPF event~~ are denoted as

- *intense* (often used synonymously with *most recent* NPF) if n_{nm} exceeds 10000 mg^{-1}~~.~~,
- *intermediate*~~-~~ for NPF with 1000 mg^{-1} < n_{nm} < 10000 mg^{-1}, and
- *weak* NPF when detected n_{nm} remained below 1000 mg^{-1}, respectively.

This classification refers to laboratory studies by (Kirkby et al. (2011), Kürten et al. (2016))~~;~~, according to ~~to these~~which ~~the~~ the NPF-rate and ~~, hence,~~ the NPF intensity (i.e. its new particle productivity) varies with the degree of supersaturation of the vapour from which the new particles form. Due to the short persistence of the freshly formed particles in the nucleation mode (cf. Section 4.5), an intense NPF event is still proceeding when observed, or it had phased-out very recently (within hours) before the detection. For encounters of weak or intermediate NPF the conclusions concerning the event's age remain ambiguous.

2.2 Particle size distributions from the~~The~~ Ultra-High Sensitive Aerosol Spectrometer UHSAS-A

The measurements of the aerosol particle size distributions during ~~the~~ StratoClim 2017 ~~field campaign (Höpfner et al. (2019); Stroh et al. (2021))~~ were performed with an in-house modified airborne version of the Ultra High Sensitive Aerosol Spectrometer (UHSAS-A; manufacturer DMT Inc., Longmont, CO, USA). The modifications ~~made to~~ on the flow and pumping system of the UHSAS-A enabled maintaining constant system-flows (sample-, sheath-, purge-flow) through the instrument even under ambient ~~(stratospheric)~~ pressures as low as 50 hPa. Details concerning the modified ~~The~~ airflow system of the UHSAS-A, the ~~was c~~characterise~~d~~ation of the instrument's particle sizing performance and its calibration during the campaign period is provided by Mahnke et al. (2021). ~~ed in the laboratory prior to the StratoClim 2017 field campaign using a controlled low-pressure chamber. The size binning of the aerosol particle size distributions results from instrument's laboratory characterisations with size-classified particles (by means of a Differential Mobility Analyzer; DMA), such as Polystyrene Latex (PSL), , and . The particle sizing performance of the UHSAS-A throughout the field campaign was monitored by means of calibrations prior to each mission flight. For these calibrations, exclusively PSL particle standards were used.~~ The uncertainty of the number concentration measured by the UHSAS-A with 1 Hz resolution was determined to be ~~approximately~~ ~ 10 % for the particle diameter range of 65 nm < d_p < 1000 nm~~. This uncertainty is~~, ~~-~~based on laboratory characterisations of the sample-flow measurement and of the counting efficiency of the instrument ~~(*ibid.*)(Mahnke et al., 2021)~~. Due to the unknown in-line temperature of the sample and the wide ambient temperature range throughout StratoClim 2017, a maximum uncertainty of the UHSAS-A measurements is estimated at 25 %. Some of the results from the measured particle size distributions and a comparison with other instruments and the Cloud-Aerosol Lidar with Orthogonal Polarization (CALIOP) are ~~also~~ presented by Mahnke et al. (2021).

2.3 Carbon monoxide (CO) measurements

~~At tropospheric altitudes, the role of carbon monoxide (CO) is understood as a pollutant (Park et al. (2009))COZahn et al. (2002)Hoor et al. (2005)is often used as a representative pollution tracer (e.g. Pan et al. (2016)). In the free troposphere, CO mixing ratios typically range between 50 nmol mol^{-1} (unpolluted) and values of up to 700 nmol mol^{-1} (polluted) next to emission~~

~~sources (Clerbaux et al. (2008); Park et al. (2009)). CO mixing ratios remain comparatively high (≳ 100 nmol mol^{-1}) within the AMA and up to altitudes of ~ 15 km. Between 15 km and 20 km altitude, CO mixing ratios gradually decrease down to ~ 40 nmol mol^{-1} (Park et al. (2009)).~~

During the StratoClim 2017 mission, CO mixing ratios were determined by means of the tunable diode laser (TDL) detection principle, which the analyser Carbon Oxide Laser Detector-2 (COLD-2) spectrometer is based on. According to comprehensive comparisons to the previous instrument version COLD (Cryogenically Operated Laser Diode, 4 s temporal resolution, (Viciani et al., 2008)), the new system implies several improvements (Viciani et al., 2018) ~~The laser source is now a room temperature Quantum Cascade Laser (QCL) that no longer requires a liquid nitrogen cooling, which also reduces size, weight and operational complexity~~. The measurement's temporal resolution is improved by a factor of four, the in-flight sensitivity of the COLD-2 spectrometer ranges at about 2 nmol mol^{-1} at integration times of 1 s, and an accuracy of 3 % is specified for the CO measurement with COLD-2 (Viciani et al., 2018).

2.4 Meteorological measurements

Atmospheric temperature and pressure data were taken from the Unit for Connection with the Scientific Equipment (UCSE, Sokolov and Lepuchov (1998)), which is a part of the ~~navigational~~ avionic system of the M-55 *Geophysica*. UCSE data are available as 1 Hz-resolved ambient pressure (accuracy: ± 1 hPa) and temperature (± 2 K accuracy). Based on these UCSE data, the potential temperature θ along the mission flight tracks is calculated in compliance with the definition by the World Meteorological Organization (WMO (1966)). For the given vertical temperature gradients and for the θ -range over which the StratoClim 2017 flights extended (i.e. up to ~ 477 K), the WMO recommended calculation of θ differs at the most by up to ~ 1 K from the values obtained when using the recently reappraised θ -calculation (Baumgartner et al., 2020).

3 Analytical methods

3.1 The height of the lapse-rate tropopause and the equivalent latitude

Meteorological data were also taken from ERA-Interim reanalyses by the European Centre of Medium-Range Weather Forecasts (ECMWF) (Dee et al., 2011). Hybrid reanalysis levels in the TTL are located at various pressure heights (i.e. around 177, 154, 133, 113, 96, 80, 67, 55 hPa, respectively) representing a vertical resolution of about one kilometre in this region.

The aircraft data are analysed in coordinates relative to the tropopause height and to the monsoon anticyclone center, respectively. The height of the lapse-rate based thermal tropopause was determined based on ERA-Interim data and following the WMO criterion (WMO, 1957) ~~as the lowest altitude (z_0) where the temperature lapse-rate falls below 2 K km^{-1}, if the average lapse-rate within an overlying layer of 2 km thickness (i.e. z_0+2 km) remains below 2 K km^{-1}. The cold point tropopause definition often yielded ambiguous results for the tropopause heights within the AMA for the StratoClim 2017 period (cf. von Hobe et al. (2020)).~~ The potential temperature θ at tropopause level was interpolated to the 1 Hz-resolved position along the flight track of the M-55 *Geophysica*, and the measurement data were sorted as a function of ~~potential temperature~~ θ ~~-~~distance ($\Delta\theta$) to the local tropopause as vertical coordinate.

The centre of the AMA was determined based on the anomalous potential vorticity distribution within the monsoon region at the 380 K potential temperature level, where lowest values of the potential vorticity (PV) are found in the AMA centre. ~~For that reason, t~~The AMA-centred equivalent latitude was calculated for a given closed PV contour as a projection onto polar coordinates (Ploeger et al., 2015). ~~Therefore, a~~An equivalent latitude of 90° North corresponds to the center of the anticyclone (lowest PV), and the equivalent latitude decreases with increasing distance from the centre, or rather, towards the anticyclone's edge. Note, that the calculation of AMA-centred equivalent latitude is ~~rigorously~~ valid within a layer of about ± 10 K around 380 K potential temperature, where a clear negative PV anomaly occurs. The uncertainties of calculated equivalent latitude become significant at levels beyond the ± 30 K range above/below 380 K.

3.2 The Coagulation Model for investigating the particles' persistence in the nucleation mode

~~Particle coagulation comprises the processes of particle collisions and their subsequent coalescence. More specifically, if two particles with masses m_i and m_j collide and coalesce, a new particle with mass $m_i + m_j$ is formed. The coagulation rate of particles with masses m_i and m_j is described by $\beta_{i,j}\, n_i\, n_j$, where n_i and n_j are the number concentrations of particles with masses m_i and m_j, respectively. The coagulation kernel $\beta_{i,j}$ characterises the coagulation rate. The choice of the coagulation kernel depends on the type of coagulating particles, in particular, on their size. Coagulation of aerosol particles is sufficiently well described by a Brownian coagulation kernel~~

~~(Jacobson (2005), Equation 15.33 therein). The kernel includes a correction term to account also for particles in the transition regime, i.e. the transition between the free-molecular regime, where the particles are small compared to their mean free path, and the continuum regime, where the particles are large compared to their mean free path.~~

The model employed in this study numerically solves the discretised coagulation equation (cf., e.g., Jacobson (2005) and Equation 15.2 therein) as formulated in the numerical chemistry-climate model SOCOL (SOlar Climate Ozone Links; Stenke et al. (2013)). For the coagulation of nucleation-mode aerosol particles the Brownian coagulation kernel (Jacobson (2005), Equation 15.33 therein) is used. The particles are assumed as spherical, and the model is based on a discretisation of the volume space, wherein the ratio of two subsequent volume size bins is constant, $\frac{V_{k+1}}{V_k} = 1.4$. The particle size range of the first volume size-bin V_1 corresponds to particle diameters of 7.5 nm < $d_{p,1}$ < 8.5 nm. With a total number of 40 size bins, ~~hence~~ the largest particle size included in this investigation is about 635 nm ($= d_{p,40} = (1.4)^{\frac{39}{3}} \cdot d_{p,1}$).

The coagulation rate and, thus, the persistence of the nucleation-mode particles, was simulated under given background conditions during observation. As input for the simulation, the aerosol size distribution detected by the UHSAS-A (nominally covering 65 nm < d_p < 1000 nm, cf. Section 2.2 and Mahnke et al. (2021)) was extended towards smaller diameters by further particle size bins obtained from the measurements with COPAS. For the simulation presented herein, the NPF event on 04 August 2017 (KTM 5) over 26 seconds between 04:04:40 and 04:05:06 UTC (pressure altitude: 110 hPa; ambient air temperature: 196 K) was selected. Each of the two size size intervals of the COPAS measurements in the nucleation mode, i.e. 6 nm < d_p < 10 nm and 10 nm < d_p < 15 nm, is divided into three subintervals to adapt to the higher particle size resolution of the coagulation model.~~The detection ranges of three COPAS channels determine two regimes in the mode, i.e. 6 nm < d_p < 10 nm and 10 nm < d_p < 15 nm, each of which is divided into three sub-bins, to exploit a higher particle size resolution of the coagulation model.~~ The three sub-bins within the size classes 6 – 10 nm and 10 – 15 nm were uniformly set to one third of the respective concentration $N_{6\text{-}10}$ ~~(~ 10000 cm^{-3})~~ and $N_{10\text{-}15}$ ~~(~ 3600 cm^{-3})~~. The difference between the total number concentrations N_{15} (COPAS) and N_{65} (UHSAS-A) yields the number concentration of $N_{15\text{-}65}$. The number concentration $N_{15\text{-}65}$ (~ 5000 cm^{-3}) was interpolated over 13 sub-bins (with exponential degradation on increasing particles size) such that the size

distribution ~~to achieve~~exhibits a ~~continued~~ continuous transition ~~of the size distribution~~ towards the detection size range of the UHSAS-A. The size-segregated aerosol concentrations measured with the UHSAS-A were interpolated (with respect to particle size) to the resolution of the remaining 21 sub-bins of the coagulation simulation. The particle concentrations $N(d_p)$ over the entire particle size range from the nucleation-mode sizes to up to d_p = 1 µm were converted into an aerosol size distribution d N / d log d_p in cm^{-3} as a representation of an initial state and input for the coagulation simulation (for more details see the results in Section 4.5).

It is worth noting, that for the coagulation simulation, the NPF event is considered as expired, i.e. any fresh supply of nucleation-mode particles due to continuous or renascent NPF is excluded for the simulated runtime of the coagulation process over 24 hours. Generally, constant conditions of atmospheric pressure (p) and temperature (T) are assumed over the 24-hours period for the simulation, as the air is lifted very slowly at TTL levels within the AMA (by ~ 1 K potential temperature per day, cf. Vogel et al. (2019), corresponding to $\Delta p \approx$ 1-1.5 hPa and ΔT < 1 K per day). ~~However,~~

3.3 Analyses of trajectories and the air mass transport history

Fifty – days backward trajectories were calculated for each sampling position along *Geophysica*'s flight track in 1 Hz resolution during the StratoClim 2017 mission using the trajectory module of the Chemical Lagrangian Model of the Stratosphere (CLaMS; McKenna et al. (2002), Konopka et al. (2012), Pommrich et al. (2014)). ~~The CLaMS backward trajectory calculations are~~ driven by horizontal winds ~~and are based on the new high resolution~~ from ERA-5 reanalysis (Hersbach and Dee (2016)). ~~which was recently released by the ECMWF. The improved resolution of the ERA-5 data compared to the ERA interim data set should increase the reliability of tropospheric transport processes along the backward trajectory analysis and may strengthen the assignment to possible source regions.~~ With the vertical resolution of the ERA-5 data ~~are given on a horizontal grid of about 0.3° × 0.3° , in 1-hour temporal resolution, in 137 hybrid levels from the surface to the 0.01 hPa pressure altitude. Hence,~~ a much better representation of convective updraught and tropical cyclones is realised ~~with the ERA-5 dataset~~ (Hoffmann et al. (2019)) compared to earlier re-analyses (Dee et al. (2011)), in particular, in the region of the Asian summer monsoon (Li et al. (2020)). Further detailed validation of the very new ERA-5 products is required, so ERA interim re-analyses still represent the state of the art until ERA-5 becomes

the new standard. ~~However, further validation of the ERA-5 products is required, thus ERA-Interim reanalyses still represent the state-of-the-art.~~

For vertical air mass transport velocities, the diabatic approach was applied using the total diabatic heating rate to extract the vertical velocity, thereby including the release of latent heat (for details, see Ploeger et al. (2021)). ~~The model boundary layer is set at ~ 2 – 3 km above the surface following orography (cf. Pommrich et al. (2014), Vogel et al. (2015)).~~

~~In general, trajectory calculations have limitations due to trajectory dispersion depending on the trajectory length. However, the frequently employed trajectory length to study transport processes in the Asian monsoon region is ranging from a couple of weeks to a few months (e.g. Chen et al. (2012); Bergman et al. (2013); Garny and Randel (2016); Müller et al. (2016); Li et al. (2017) and Li et al. (2018)). The CLaMS trajectory products based on the ERA-5 dataset were extensively investigated concerning their spatial and temporal resolution in connection with strong vertical transport (e.g. Hoffmann et al. (2019)). However, Li et al. (2020) demonstrated, by means of satellite-borne (FY-2D) brightness temperature data and balloon measurements in China, that convective events over the Pacific Ocean associated with tropical cyclones are resolved by CLaMS trajectory calculations with high accuracy.~~

The CLaMS backward trajectory calculations, which were initialised from each sampling position along the flight track in 1 Hz resolution, were used to allocate the air's latest contact with the model boundary layer at 2 – 3 km above the ground. This allows for investigating the location of the sources influencing the mixing ratios in the air samples taken aboard the M-55 *Geophysica*. ~~To include the uncertainty of a certain backward trajectory, ERA-5 backward trajectories were calculated for each second of air sampling during the flight.~~

3.4 The age of air since release from convective outflow

~~This approach aims at investigating the possible influence of recent convection on NPF, filtering out small contributions from matured air, which may be mixed in an air parcel but have only a minor influence on the overall air mass composition.~~ The history of a convective air mass is analysed by making use of the TRACZILLA Lagrangian model (Pisso and Legras, 2008), which is a variation of FLEXPART (Stohl et al., 2005). ~~In its recent version the model interpolates velocities and heating rates directly from the hybrid grid to the position of the parcel using~~

~~logarithmic pressure or potential temperature as vertical coordinate.~~ The simulations were based on the release of a cluster of 1000 back-trajectories, representative of a generic aerosol tracer, each launched ~~at respective, each trajectory cluster~~ from a ~~1~~one-second resolved time step along the flight path. The trajectories were traced back over a period of 30 days in the geographical domain (between 10°W~~-~~ and 160°E and between equator and 50°N, respectively). The meteorological fields (horizontal winds and radiative heating rates) are taken from ~~the ECMWF reanalysis~~ ERA-5 reanalyses ~~with 1-hour-resolution, assuming diabatic vertical motion~~. The convective influence is then distinguished from uninfluenced cases by ~~the~~ high-frequency images (one image per 10 – 15 minutes) of cloud top altitudes from the geostationary satellites MSG1 and Himawari (for details see Bucci et al. (2020)). ~~For computational reasons Himawari images were analysed in time steps of 20 minutes. The cloud top height of convective clouds is derived from the cloud top temperature and height (CTTH) product, developed within the European Organisation for the Exploitation of Meteorological Satellites (EUMETSAT) Satellite Application Facility (SAF) by support of Nowcasting Very Short Range Forecasting (NWC) products (Derrien et al. (2010); Schulz et al. (2009)).~~

Investigations by Weigelt et al. (2009) previously approached the influence of convective cloud processes on the number concentrations of aerosols and in particular of nucleation-mode particles in the upper troposphere. In present study, the convective sources were identified as such if the course of a TRACZILLA-modelled trajectory within a certain geographical area ~~coincides with~~ is found below the cloud top level, as similarly done by Tzella and Legras (2011) and Tissier and Legras (2016)~~. The possible convective sources are classified into major source region categories~~. It is noteworthy that, while the adopted trajectory method bypasses the uncertainties related to the convective representation in the reanalysis by using observation-based information on the convective events, uncertainties still remain. Those arise mainly from uncertainties in the identification of the cloud top from image data of geostationary satellites, the impossibility to account for the entrainment – detrainment – processes, and reanalysis-related uncertainties concerning advection (for more details ~~on the trajectory-convective clouds coupling methods~~ see Bucci et al. (2020)). In the presented analysis, the air mass age is computed as the difference between the time of release of the cluster and the convective cloud crossing. Since the trajectory cluster can spread in space and bring different contributions from different regions, only the mean age from the dominant convective source (i.e. the mean age

from the regions with the highest percentage of convective clouds crossings) is considered in this analysis.

4 Observations and results

Figure 1~~Figure 1~~ shows the flight tracks of the eight mission flights conducted during StratoClim 2017. The vertical indices (visible in Panel b) highlight the flight sections where significantly increased mixing ratios of nucleation–mode particles n_{nm} were encountered, which are ~~most likely~~ attribut~~ed~~ able to NPF. NPF of varying intensity occurred near or above the southern flank of the Himalayan ~~mountain chain~~ (features over Nepal and towards Northeast India) and in a distance of more than 500 km away from the mountains (near the coastline of Bangladesh or the Northeast Indian coast towards the Sea of Bengal). Of the entire COPAS measurement time (~ 22.5 hours) at altitudes above 10 km (≳ 350 K potential temperature) ~~over almost~~about one third (i.e. ~ 9 hours) of the air samples were taken north of 26° N, i.e. mainly in the immediate vicinity of the Himalayan Mountains, over Nepal and neighbouring areas of northeast India. Hence, over the period of the StratoClim field mission during the 2017 monsoon season, the main transport of NPF precursor material into the UT/LS was ~~apparently~~ by convection above the foothills of the Himalayas. The present study aims at a classification of encountered NPF events with regard to:

1. the height intervals and geographical positions of NPF observations,
2. the time limits (event duration and day time of occurrence),
3. spatial dependencies with regard to tropopause height and AMA geometry~~.~~,
~~3.~~4. the relationship between NPF and the air's origin and age.

~~Moreover, the relationship between NPF and the air's origin and age is investigated.~~ It is noteworthy that, during StratoClim 2017, NPF was frequently observed in the presence of ice cloud particles at the bottom TTL of the AMA. The conditions under which ~~The particular occurrence of~~ in-cloud NPF occurred during StratoClim ~~is~~ are discussed in Weigel et al. (2021b). Since the NPF turned out to be almost undisturbed by the presence of cloud elements (until a certain number density and size of the ice particles are reached), for the present study the NPF encounters remain ~~unseparated~~ undifferentiated concerning clear-air or in-cloud conditions ~~and are instead discussed in their entirety~~.

4.1 Vertical distribution of particle number concentrations with respect to observations in ~~the~~ different tropical~~tropic~~ regions~~s~~

Vertical profiles of the total particle number concentration obtained from various field campaigns in the tropics are shown as median with percentiles in Figure 2~~Figure 2~~. The vertical CN ~~CN~~ profiles from tropical regions of South America and West Africa (TROCCINOX, 2005 and SCOUT-AMMA, 2006, Figure 2~~Figure 2~~, Panels a and b) exhibit merged data of two independent CN-detectors with individual d_{p50} (i.e. N_6 for $\theta > 350$ K and N_4 for $\theta < 350$ K), which were deployed on individual aircraft, the M-55 *Geophysic*a and the DLR Falcon-20 (cf. Borrmann et al. (2010) and Weigel et al. (2011)). ~~The observations from measurements within the AMA over the Indian subcontinent (StratoClim 2017) at altitudes of about 320 K < θ < 475 K potential temperature exclusively result from COPAS measurements aboard the M-55 *Geophysica*.~~ The dark shaded areas of the vertical profiles illustrate the scatter of number concentrations between the 90th and 99th percentiles. At tropopause altitudes around 380 K (indicated by vertical bars), or rather at the bottom TTL, the variability of detected concentration reaches a maximum between 90th and 99th percentile ~~(note the logarithmic scale of *N*)~~. The increased data scatter indicates the influence of NPF on the class of sub-micrometre sized particles at these TTL levels, resulting in increased and fluctuating particle number concentrations due to the variable production rate of particles by NPF (cf. Section 0~~2.1.3~~). Exclusively above the tropopause within the AMA (Figure 2~~Figure 2~~ c), the scatter of the concentration values of sub-micrometre sized particles remains elevated ~~at~~ up to heights of ~ 400 K potential temperature. Up to this point within the AMA, the scatter of the peak number concentrations (90th to 99th percentile range) is significantly increased in reference to the median values ~~Up to this point, the dark shaded area (90th to 99th percentile range) of the AMA profile is visibly increased compared to median values~~, while ~~aerosol concentrations measured above the tropopause~~ in other regions above the tropopause (Figure 2~~Figure 2~~ a and b) ~~–~~ the profiles of aerosol concentrations show~~exhibit~~ a smoother transition into the stratosphere.

For comparison, in Panel d of Figure 2~~Figure 2~~, particle number concentrations $N_{5.3}$ are compiled as a vertical median profile (with percentiles) obtained from airborne measurements with the Nuclei Mode Aerosol Spectrometer (NMASS; Brock et al. (2000)) during several years (2004 – 2007, including winter and summer season) over Central America. These observations

~~additionally~~ differentiate the bottom TTL (here 350 – 379 K) as the region where NPF predominantly occurs with the largest impact on the fine-mode (sub-micrometre sized) aerosol particle concentration (e.g. Borrmann et al. (2010) or Weigel et al. (2011)). However, this vertical profile (Figure 2~~Figure 2~~ d) ~~implies~~ illustrates additional features at altitudes above the mean tropopause altitude (assumedly located at ~ 380 K). The locally increased concentrations with respect to the median become apparent at ~ 380 – 390 K and at ~ 400 - 410 K, respectively. Above tropopause levels, significantly increased number concentrations of fine-mode particles, potentially caused by local NPF, were observed over both, Central America (Figure 2~~Figure 2~~ d) and the Indian subcontinent within the AMA (Figure 2~~Figure 2~~ c).

4.2 Mixing ratio~~s~~ of submicron particles, abundance and fraction of refractory particles from StratoClim 2017 observations

The entire StratoClim 2017 data set of measured (1 Hz-resolved) particle mixing ratios n_6 and n_{10} is summarized in Figure 3~~Figure 3~~ a as function of potential temperature. The resulting median profile n_6 of the StratoClim 2017 measurements is shown with 25th and 75th percentile (blue profile). This allows for a direct comparison with the corresponding median profiles from earlier COPAS measurements at tropical regions (in red: TROCCINOX, Brazil, 2005 and in dark green: SCOUT-AMMA, West Africa, 2006, cf. Borrmann et al. (2010) and Weigel et al. (2011)). Figure 3~~Figure 3~~ a includes also the median vertical profile of the mixing ratios of fine-mode particles (bright green line), which was obtained from measurements over Central Pacific, at tropical latitudes (Brock et al., 1995).

The profiles (n_6, n_{10}, and n_{nm} in Figure 3 a and b) ~~appear to be~~ are structured as:

1) ~ 350 – 380 K: characterised by the largest scatter of the particle mixing ratios and the highest values of up to $5 \cdot 10^4$ mg^{-1}, thus, representing the height level of the profile's maximum.
2) ~ 380 - ~~400~~ 415 K: the scatter of the particle mixing ratios is still increased though less ~~expressed~~prominent.
3) Above ~ ~~400~~ 415 K: characterised by a comparatively weak but extant scatter level of particle mixing ratios, which also includes features of the median n_6 profile at 410 – 415 K within the AMA.

The ~~general~~ course of the median profiles exhibits ~~largely~~ similar characteristics. The common feature of all median profiles from the tropics is their ~~almost consistently located~~ maximum at about 350 – 360 K, while the AMA observations indicate a corresponding maximum at slightly higher altitudes (i.e. 355 – 365 K). Further ~~up~~aloft, the particle mixing ratios obtained from different locations decrease with altitude ~~with an almost corresponding~~on similar gradient. In the altitude range between 360 K and 400 K, the tropical data obtained over South America (red) constitute the lowest particle mixing ratios (by median values), whereas all other profiles are almost in line with each other up to ~~400~~ 400 K. The vertical median profile of particle mixing ratios determined in the AMA (blue) during StratoClim 2017 exhibit~~,~~ ~~however,~~ the highest mixing ratios at each height level up to ~ 415 K. Additionally, the AMA profile features a substantial increase of the median mixing ratio at altitudes of ~ 410 - 415 K, where the values exceed those from the tropical regions by ~~almost~~ about 35 %. Above 415 K, the continuation of the tropical profiles from West Africa and Central America (coloured green) with altitude is largely consistent with the particle mixing ratios measured throughout StratoClim 2017, while at these altitudes the measurements from South America (red) show comparatively increased values. Above 440 K, the particle mixing ratio over West Africa (dark green) significantly deviates from those of all other vertical profiles, as ~~it is expressed by a~~visible from the gradual increase of the particle mixing ratio with altitude. This deviation ~~, which~~ was attributed to the influence of the high-reaching volcanic injections of Soufriere Hills (Borrmann et al., 2010). The 1 Hz-resolved StratoClim 2017 data (grey dots in Figure 3 a) are added to the graph to~~additionally~~ illustrate how the scatter of measured particle mixing ratios relates to corresponding median profiles.

Figure 3~~Figure 3~~ b shows the vertical distribution of the mixing ratio of the nucleation-mode particles n_{nm} (cf. Subsection 0~~2.1.1~~). The flight-by-flight colouration of the data points indicates that increased n_{nm} values were observed during each of the eight StratoClim 2017 mission flights. In addition, Figure 3~~Figure 3~~ b shows the wide range of altitudes over which the layers of increased n_{nm} were observed during the individual flights. Remarkably ~~high~~ increased values of n_{nm} were detected up to altitudes as high as 400K.

Figure 3 c ~~exhibits~~ depicts the 1 Hz-resolved mixing ratios of the non-volatile particles n_{10}nv (cf. Appendix A~~Subsection 2.1.2~~) ~~as a function of the potential temperature. The graphic also~~

~~includes~~as also the resulting median profile of n_{10}nv with 25th and 75th percentiles. Figure 3~~Figure 3~~ c additionally shows the median profile of n_6 as in Figure 3~~Figure 3~~ a, which illustrates the vertical progression of n_{10}nv in direct relationship to the NPF-influenced total particle mixing ratio.~~.~~ ~~In~~ Figure 3 d illustrates~~,~~ the vertical distribution of the fraction f of non-volatile particles, i.e. the ratio $\frac{n_{10}\mathrm{nv}}{n_{10}}$ (cf. Subsection 2.1.2), ~~is shown~~ which is presented in 1 Hz-resolution ~~as well~~ as also the profiles ~~the~~ of resulting median ~~profile~~ with 25th and 75th percentiles. At lower altitudes (< 350 K), the mixing ratio of non-volatile particles appears ~~predominantly~~ low with a relatively large scatter. The local minima of the n_{10}nv profile and of the fraction f coincide with the local maximum of n_6 (i.e. ~ 355 - 375 K). Above 370 K, the n_{10}nv profile follows the general decline with height. Above 390 K, both mixing ratios (n_6 and n_{10}nv) decrease uniformly and the fraction f remains almost constant at ~ 45 – 50 % up to altitudes of 430 K. Towards 435 K, the total mixing ratio n_6 nearly stagnates whereas n_{10}nv exhibits slightly dropping mixing ratios.

~~At altitudes where n_6 exhibits the maximum particle mixing ratio (i.e. ~ 355 - 365 K), the n_{10}nv profile almost stagnates or even decreases slightly. The local minimum in the fraction f is reached at about the same height (355 – 375 K), as result of the significantly increased total particle mixing ratio (likely due to NPF) with simultaneously declining n_{10}nv. On transition to 370 K, the mixing ratio n_{10}nv is again slightly elevated, and above 370 K, the n_{10}nv profile follows the general decline with height. Nevertheless, up to 380 K, the decrease of n_6 with altitude is steeper compared to that of n_{10}nv. On transition to the 390 K level, a sharp drop in the median f profile mainly results from the sudden change of the n_6 gradient at this altitude, whereas the n_{10}nv profile exhibits no obvious feature at the same height. Above 390 K, both mixing ratios (n_6 and n_{10}nv) decrease uniformly and the fraction f remains almost constant at ~ 45 – 50 % for the altitude range up to 430 K. Towards 435 K, the total mixing ratio n_6 almost stagnates whereas n_{10}nv exhibits slightly dropping mixing ratios. Thus, at this point, the shape of the median f profile is mainly determined by a decrease of the non-volatile proportion of the particle population. Further above, in transition to 440 K potential temperature, both mixing ratios (n_6 and n_{10}nv) commonly exhibit a steep decrease.~~

In essence, the vertical profiles of the total particle mixing ratio n_6 and those of the non-volatile particles n_{10}nv are divided into three ranges:

A) At the bottom TTL region ($\theta < 375$ K), both n_6 and n_{10}nv ~~seem to be~~are mainly characterised by NPF as indicated by the high mixing ratios of nucleation-mode particles n_{nm}. NPF causes a significant addition to the scatter of the total mixing ratios towards high values, which exceed the median by more than one order of magnitude. In this altitude range, a local deficit of the non-volatile particle compounds ~~is a favourable~~ favours the occurrence of ~~precondition for~~ NPF ~~to occur~~.

B) Further above, i.e. ~ 375 K $< \theta < 415$ K, continued albeit attenuated NPF is identified at tropopause levels within the AMA. The non-volatile particle compounds (n_{10}nv) ~~are~~ slightly ~~elevated~~ decrease compared to levels below 375 K. The fraction f however rises towards 40 %. Nevertheless, n_{nm} of 400 - 2000 mg^{-1} at heights of up to $\sim$ 400 K indicate ~~unimpededly proceeding~~ sustainably effective NPF.

C) Above 415 K, the values of the total mixing ratio n_6 approach~~es a course that corresponds to~~ previous observations (e.g. Brock et al. (1995)). The scatter of n_6 and n_{10}nv is considerably decreased at these altitudes. NPF appears to have entirely abated, since at these heights sufficiently high n_{nm} were not observed at all. The median proportion f of non-volatile particles ~~of~~ remains at ~40 – 50 % ~~remains~~ up to the highest altitude.

The steeply dropping vertical profile of the total mixing ratio of the sub-micrometre sized aerosols above $\sim$ 415 K ~~may~~ subtly indicates the upper limit of the AMA's influence on the vertical mixing of the UT/LS. From the CO, ozone, and nitrous oxide content in air samples taken throughout StratoClim 2017, von Hobe et al. (2020) concluded that the AMA's interior was largely isolated from stratospheric in-mixing up to altitudes of 10 to 20 K above the tropopause (i.e. $\theta \approx 400$ K). Moreover, they found that mixing processes with stratospheric air are of increasing significance at levels between 400 K and 420 K (*ibid.*). At altitudes above $\theta \approx 440$ K, the median mixing ratios n_6 exhibit a vertically stable continuation after another sharp drop between 435 K and 440 K (Figure 3~~Figure 3~~ a and b). Brunamonti et al. (2018) specified the 440 K level as the top of confinement (TOC) of the AMA for the 2017 monsoon season. So, according to this TOC definition, above 440 K potential temperature ($\gtrsim$ 18.5 – 19 km), the median n_6 (Figure 3~~Figure 3~~ a and b) ~~may~~ represents stratospheric background values.

The ATAL (Vernier et al. (2011a), and see also Höpfner et al. (2019); Mahnke et al. (2021)) is mainly attributed to the uplift of pollution from the boundary layer as concluded from balloon-borne and satellite-based observations (Vernier et al., 2018). The described drop in the aerosol concentration (*ibid.*) at potential temperatures of ~ 400-420 K (well above tropopause levels) coincides with the uppermost altitude limit of main NPF activity at ~ 400 K (~ 17.5 km) observed during StratoClim 2017 (cf. Figure 3~~Figure 3~~). Here, the most substantial decrease of both mixing ratios n_6 and n_{10}nv was observed on transit from ~ 410 K to ~ 415 K (at ~ 18 km).

4.3 Occurrence frequency of NPF events

~~In compliance with the event definition (cf. Subsection 2.1.3), all observed NPF events (130 individual events) are sorted by their duration and the result is displayed in~~ Figure 4~~Figure 4~~ shows the 130 individual NPF events sorted according to their duration. Based on the average flight speed (Section 0~~2.1.3~~), and assuming a constant heading during flight, the mean horizontal distance per 10 seconds flight time ranges at about 1.5 km. The spatially most extended uninterrupted NPF signature throughout StratoClim 2017 spanned a mean horizontal distance of ~ 110 km.~~ The majority of observed NPF events cover durations of several tens of seconds or less. About 50 NPF events had very short durations of less than 10 s (Figure 4 a and b), while an almost equal number of NPF events was observed over a continuous period of 10 – 55 s (~ 1.5 – 8.5 km; Figure 4 b). Longer lasting NPF events of about 40 – 80 s (~ 6 – 13 km) occurred less than six times during the entire campaign period. All NPF events of even longer duration (up to ~ 12 minutes) occurred mostly once, but never more than two times in total throughout the mission period~~ The hitherto most extended NPF event observed with COPAS at TTL level over South America (Weigel et al. (2011)) lasted over a continuous duration of 262 seconds (~ 35.5 km of covered flight distance). Another three individual NPF events were observed above West Africa (*ibid.*) over 20, 83, and 98 seconds (~ 3 km, ~ 12 km, and ~ 13 km) respectively. Approximately 45 % of 130 NPF events observed throughout StratoClim 2017 were of less than 20 seconds duration (~ 3 km), while the majority (~ 75 %) of NPF observations above the Indian subcontinent extended over less than 80 seconds (~ 12 km, Figure 4~~Figure 4~~ a~~)~~. The vertical profile (Figure 4~~Figure 4~~ b) ~~clearly shows~~show that above 380 K predominantly short events of less than two minutes duration with comparatively low mixing ratios n_{nm} were encountered. Here, observed NPF events rarely lasted for several

minutes (i.e. 5-6 minutes). In the lower TTL range, i.e. below the tropopause, the number of persistent NPF events was higher than above the tropopause, and the mixing ratio of nucleation-mode particles was also more often increased. The highest mixing ratios of nucleation mode particles were measured in events lasting from one to a few (up to about seven) minutes.

~~The diurnal distribution of observed NPF events is exhibited in~~ Figure 5~~Figure 5~~ depicts the diurnal distribution of observed NPF events. The frequency of NPF event observations is analysed as a function of the local daytime (LT) at Kathmandu, Nepal (Figure 5~~Figure 5~~ a). Apart from one exception, the occurrence frequency of the NPF events seems evenly distributed over the course of a day. The exception is a time window ~~at about~~between 10:00 and 10:30 a.m. (LT) when recent particle formation was observed up to 2.5 times more often than at other times of the day. In this time window, about one third of all NPF events (31 of 105 events with durations of more than 5 seconds) was observed, most of which (25 of 31 events) lasted for less than 80 seconds (< 12 km mean horizontal distance). The measurements in this time window occurred at two distinct altitude layers, ~ 360 - 370K and ~ 390 – 400 K. The majority of the StratoClim NPF events in this period (20 of 31 events) were from altitudes above 390 K while ascertained mixing ratios $\overline{n_{\mathrm{nm}}}$ never ranged outside ~ 500 - 5000 mg^{-1} during this day time. Throughout the StratoClim 2017 mission, no further NPF event was observed above 390 K at any earlier day time and only two single events were encountered at these heights during different flights at a later day time (~ 12:20 and ~ 17:30 LT, respectively). ~~Definitive elucidation of w~~Whether this pronounced frequency of NPF occurrence at a particular time of day is due to bias effects would require a larger database. Beyond this, preferred day times when NPF was observed with particular frequency were not identified in the StratoClim observations, while instead, within the same region, a diurnal dependence of NPF was previously concluded based on a larger data set (Hermann et al., 2003). The diurnal dependence of NPF would be expected if H_2SO_4 is assumed to be the main nucleating compound whose production maximum (from the reaction SO_2 + OH) at the local noon time correlates with the solar zenith (cf. Weigel et al. (2011)).

Throughout StratoClim 2017, NPF was predominantly observed before local noontime during the mission flights KTM 2, KTM 3, KTM 5 and KTM 7, while all other observations were made mainly during the afternoon. All NPF events, which lasted longer than five seconds, were almost

~~homogeneously~~evenly distributed over the day. Furthermore, Figure 5~~Figure 5~~ c ~~also~~ indicates that the longest NPF events are not generally associated with highest mean mixing ratios $\overline{n_{\mathrm{nm}}}$. The duration of an event is therefore primarily an indicator of the spatial extent of a region where NPF takes place. The derivation of the spatial extent from the duration of individual events, however, bears significant uncertainties, since changes in flight attitude, such as curve manoeuvres or changing flight levels during an event, are not taken into account.

~~However, t~~The NPF events observed during StratoClim 2017 are among the most frequent and spatially most extended of all those, which have been identified by means of COPAS measurements during previous missions (cf. Borrmann et al. (2010); Weigel et al. (2011)). Only a few events were observed during StratoClim 2017, which lasted more than 100 seconds, but it cannot be excluded that they were actually composed of individual events of smaller extent. Very short events (< 10 s) make up almost 40 % of all NPF events observed. Consequently, hereafter, all events shorter than five seconds (i.e. 25 out of 130 events) are discarded from further analyses ~~for the reasons described in Subsection 2.1.3 and for avoiding biasing effects~~. In this way, individual 1-2 second features are filtered from the data. In addition, for the evaluation of individual NPF events, the reliability of the results increases if the arithmetic averaging occurs over more than five data points. Finally, the accuracy of the specified event duration improves as the raw signal processing (Subsection 2.1.3) smooths the temporal salience of short events.

4.4 The occurrence of NPF relative to the tropopause height and the AMA's centre

~~ERA-interim reanalysis data were used to determine the altitude of the lapse-rate tropopause in accordance with the definition by the WMO (1957) for each measurement point along the flight path (cf. Section 3.1). For the individual NPF events, a mean tropopause height was obtained together with mean values of detected . The relationship between the measurement height and the lapse-rate tropopause height is expressed as difference $\Delta\theta$ in K. In addition to the vertical position of NPF events (i.e. in terms of absolute height or distance from the tropopause), the individual NPF events were examined with respect to their position within the AMA by means of the equivalent latitudes ϕ_{equ} (cf. Section 3.1).~~

Figure 6~~Figure 6~~ illustrates the mean mixing ratio of nucleation mode particles $\overline{n_{\mathrm{nm}}}$ measured during the individual NPF events as a function of (1) the vertical distance $\overline{\Delta\theta}$ to the lapse rate

tropopause (Figure 6~~Figure 6~~, Panels a and c) and (2) the mean equivalent latitude $\overline{\phi_{equ}}$ (Figure 6~~Figure 6~~, Panels b, and d). NPF events above the lapse-rate tropopause (Figure 6~~Figure 6~~ a, positive $\overline{\Delta\theta}$ and up to + 30 K) were mainly observed during the first half of the StratoClim 2017 mission (KTM 2, KTM 3, and KTM 5; on 29 July, 31 July, and on 04 August 2017, respectively, with maximum ceiling > 475 K) or during the last mission flight (KTM 8, on 10 August 2017, maximum ceiling ~ 435 K). All further observations up to θ > 425 K were located below the lapse-rate tropopause (negative $\overline{\Delta\theta}$, down to - 35 K) or in its close vicinity ($\overline{\Delta\theta}$ ≈ 0 K, e.g. KTM 6, 06 August 2017, maximum ceiling ~ 380 K), i.e. in or above the region of the main convective outflow. As indicated by Stroh and the StratoClim group (2021), the first half of the StratoClim 2017 mission was characterised by weak convection, while the convective activity increased as the campaign progressed.

~~NPF event observations throughout StratoClim 2017 were limited to an altitude interval between about – 35 K and + 30 K potential temperature around tropopause heights, corresponding to a pressure range of 70 – 340 hPa and ambient temperatures between 187 K and 257 K according to observational data.~~ With respect to the AMA centre, most NPF events were encountered north of 60° equivalent latitude (Figure 6~~Figure 6~~ b). An exception is a flight segment of flight KTM 3 (on 31 July 2017), where weak NPF with mixing ratios $\overline{n_{nm}}$ of ~ 500 - 1300 mg^{-1} were detected at the farthest distance from the AMA centre (near the turning point at about 21.5° N and 80° E geographic coordinates, see Figure 1~~Figure 1~~). These measurements (at $\overline{\phi_{equ}}$ < 60° N) were made well above the tropopause since at positive $\overline{\Delta\theta}$ (up to + 10 K) mean CO mixing ratios of 45 - 50 nmol mol^{-1} (Figure 6~~Figure 6~~, Panels c and d) ~~are commonly~~in agreement with ~~found at positive $\overline{\Delta\theta}$ between + 5 K and (up to + 10 K)~~ satellite-based CO observations for altitudes of ~ 16-19 km within the AMA (Park et al., 2009).

Towards the AMA centre ($\overline{\phi_{equ}}$ > 60°N), the NPF events are distributed over the entire range of $\overline{\Delta\theta}$. Here, weak NPF with several hundreds of nucleation-mode particles per milligram were observed ~~at $\overline{\Delta\theta}$ of up to about + 28 K~~ well above the lapse-rate tropopause ($\overline{\Delta\theta}$ ≈ + 28 K). The vertical distribution of the NPF events indicates that those events with the highest $\overline{n_{nm}}$ and mainly elevated CO mixing ratios (65 nmol mol^{-1} to ~ 137 nmol mol^{-1}) were encountered exclusively below the lapse-rate tropopause (to minimum $\overline{\Delta\theta}$ of - 35 K). ~~However, none of these NPF events with elevated n was detected at equivalent latitudes $\overline{\phi_{equ}}$ < 60°N~~. Regarding a

relationship between (a) the relative position to the AMA centre and (b) the effectiveness of vertical transport or the NPF rate, the StratoClim 2017 data show: between 60°N and 90°N equivalent latitude, there is no indication ~~apparent~~ that the mixing ratios of $\overline{n_{nm}}$ and CO depend on the position with respect to the AMA centre. ~~Panel e of shows the NPF event distribution in the combined coordinate space of the equivalent latitude and the vertical distance from the lapse-rate tropopause. NPF events with highest ($\gtrsim$ 1300 mg^{-1}) were found exclusively between 60° N and 90° N with respect to the AMA centre and often immediately underneath the lapse-rate tropopause ($\overline{\Delta\theta} \lesssim$ - 3 K, colour range from blue to yellow). NPF events with low ($\lesssim$ 1300 mg^{-1}) were exclusively found at tropopause levels ($\overline{\Delta\theta} \approx 0 \pm 5$ K, orange colours) or well above the lapse-rate tropopause ($\overline{\Delta\theta} >$ 10 K, red data points).~~ Close to the AMA centre (60°N - 90° N) and in an altitude range of almost ± 30 K around tropopause heights, both the distribution of CO-enriched air masses and the occurrence of NPF appear as largely independent from $\overline{\phi_{equ}}$.

4.5 Persistence of particles in the nucleation mode

~~Coagulation constitutes one of the main processes, which limits the persistence of nucleation-mode particles~~Coagulation represents one of the main processes limiting the persistence of nucleation mode particles, i.e. the duration during which freshly formed particles remain in the size range of the nucleation mode. At elevated number densities, the highly diffusive nucleation-mode particles collide and coagulate with each other and with the present background aerosols on short time scales. Gaseous precursors, which are ~~highly saturated~~saturated or supersaturated under NPF conditions, may condense and additionally contribute to the growth of particles out of the nucleation-mode size range, which is considered ~~hereafter, however,~~ as a secondary process.

The aerosol size distribution, which was compiled from the measurements during a NPF event as input for the coagulation simulation (cf. Section 3.2), is depicted in Figure 7~~Figure 7~~ (black circles with horizontal bars indicating the width of their respective particle size bins of the model). The simulated change of the initial aerosol size distribution due to coagulation is shown in ~~1~~one-hour steps in different colours and line types (Figure 7~~Figure 7~~ a). From this simulation, the temporal decay of N_{nm} was derived (Figure 7~~Figure 7~~ b, solid black line), whereby the gradient of this decay illustrates the coagulation rate. The sequence of the simulated size

distributions indicates that the initial amount of nucleation-mode particles is reduced by coagulation within a few hours~~. Coagulation is most effective particularly in the particle size range of d_p < 15 nm~~. Within the first hour after an expired NPF event the nucleation mode is no longer predominant in the overall size distribution, as seen from the maximum of the distribution at d_p > 15 nm after one hour of simulated coagulation (solid red line in Figure 7~~Figure 7~~ a). Hence, with adopted instruments for the detection of~~based on number concentrations of particles in the~~ nucleation mode particles~~, a clear signature of NPF is detectable only~~ a clear NPF signature is identified only ~~when~~ while a NPF~~ event~~ is just proceeding or for a very short time immediately~~right~~ after an expired NPF event.

The concentration of nucleation-mode particles N_{nm} decreases steeply over time (Figure 7~~Figure 7~~ b). From initially ~ 13000 cm^{-3} of nucleation-mode particles (~ 75 % of N_{total}) at the earliest stage, N_{nm} falls below 1000 cm^{-3} (~ 20 % of N_{total}) within about 1 hour (the grey shaded areas ~~may~~ serve~~s~~ for reference). The detection of 1000 cm^{-3} of nucleation-mode particles, however, ~~could~~ would be interpreted as a NPF event of intermediate strength (cf. Section 0~~2.1.3~~). In addition, coagulation leads to N_{nm} below 100 cm^{-3} (< 5 % of N_{total}) during less than four hours and to N_{nm} of less than 10 cm^{-3} within nine hours.~~, which significantly~~The efficiently proceeding coagulation impedes the identification of NPF based on *in-situ* detections and it is required to be at the NPF site at the right time. This circumstance is corroborated by tests concerning the sensitivity of the simulation to varying input parameters. For these tests,~~. N_{nm} of less than 10 cm^{-3} (reached within nine hours) would not be identified as NPF event by means of COPAS measurements.~~

~~The sensitivity of this simulation was investigated by varying the simulation input. Therefore, exclusively the~~ the input in the nucleation mode was modified while keeping constant background aerosol conditions. In three further simulation runs, the initial N_{nm} was multiplied by the factors 0.1, 10 and 100, respectively ($N_{nm,\,0.1}$, $N_{nm,\,10}$, $N_{nm,\,100}$, dashed lines in Figure 7~~Figure 7~~ b). Increased initial concentrations of nucleation-mode particles, $N_{nm,\,10}$ and $N_{nm,\,100}$, last only for about 15 minutes compared to the original N_{nm} (black line in Figure 7~~Figure 7~~ b). The initial values ~ 10^5 or ~ 10^6 cm^{-3} drop very quickly due to elevated coagulation rates, and in both of these cases, $N_{nm,\,10}$ and $N_{nm,\,100}$ fall below 1000 cm^{-3} within less than one hour. The threshold of 100 cm^{-3} is crossed after less than 2 hours ($N_{nm,\,10}$) or after 30 minutes ($N_{nm,\,100}$). Therefore, NPF

events, which produce much higher concentrations of nucleation-mode particles, require even shorter time periods for a successful detection (e.g. by COPAS) after their expiration. However, for the simulation of decreased concentrations ($N_{nm,\,0.1}$), the coagulation rates remain nearly constant, as indicated from the almost identical decays of $N_{nm,\,0.1}$ and N_{nm} (Figure 7~~Figure 7~~ b). Simulated concentration of nucleation-mode particles fall below 100 cm^{-3} within almost the same time from the initial values $N_{nm,\,0.1}$ or $N_{nm,\,10}$, respectively. Further investigations on the sensitivity of the simulation to the assumed pressure and temperature conditions as simulation input did not reveal any significant dependence, unless the input is varied by more than ± 10 hPa and ± 18 K from used values of respective parameter (not shown herein).

Based on these estimations, the detection of elevated N_{nm} ~~strongly~~ indicates that an event with high NPF-rates is currently proceeding, or a recently expired NPF event was observed~~. Due to the short persistence of nucleation-mode particles (a few hours), the observations of events with elevated N_{nm} are considered as made "well in time"~~. Detections of lower values of N_{nm} could indicate a) intermediate or weak (currently proceeding) NPF at low supersaturation of the NPF precursor or b) a NPF event (e.g. of high particle productivity) that has phased-out several hours before the observation. NPF is measured *in-situ* while the formation event is currently in progress or at most a few hours later. Therefore, the short periods of time available for a clear NPF detection and the yet frequent NPF encounters on each measurement flight during StratoClim 2017 indicate the prevalence of such events within the AMA.

5 NPF's connection to ground sources and vertical transport

5.1 NPF in relationship to CO as pollution indicator

NPF events with moderate numbers of nucleation-mode particles (< 1000 cm^{-3}) in the lower TTL region were previously attributed to CO mixing ratios above ~ 70 nmol mol^{-1} (60 - 70 nmol mol^{-1} were assumed as a typical CO background in the pristine marine boundary layer, cf. Weigel et al. (2011)). Elevated amounts of nucleation-mode particles (of up to ~ 6000 cm^{-3}) at altitudes of 350 K < θ < 360 K were associated with significantly increased CO mixing ratios of more than 85 nmol mol^{-1} (*ibid.*). These results, mainly based on two single NPF events over West Africa (SCOUT AMMA 2008), could have indicated a correlation between NPF rates and CO- load from pollution. However, almost a hundred of individual event observations (Section 4.4 and Figure 6~~Figure 6 ,~~ (Panels c and d) indicate, that the relationship between pollution level and NPF-rates

is less direct than expected. In Figure 8~~Figure 8~~, the 1 Hz-resolved data of synchronous detections of CO and particle mixing ratio during the entire StratoClim 2017 mission are compared. To illustrate the relative scattering of both n_6 and n_{nm}, the total particle mixing ratio n_6 is shown in the background (grey dots) and the mixing ratio of particles in nucleation mode n_{nm}, (dots coloured with respect to θ) is displayed in the foreground.~~The total particle mixing ratio n_6 is shown in the background (grey dots) of the mixing ratio of nucleation mode particles n_{nm}, (coloured data points in reference to θ) to illustrate the scatter range of both n_6 and of n_{nm}.~~

At altitudes below the tropopause (below ~ 380 K), where NPF-rates ~~causes the~~ lead to highest n_{nm}, the relationship between the 1 Hz-resolved n_6 or n_{nm} and the CO mixing ratio is highly variable. At CO levels of 80 – 100 nmol mol^{-1}, the scatter of n_{nm} ranges from 700 mg^{-1} to the absolute maximum of about 50000 mg^{-1}. This maximum n_{nm} is exclusively reached at CO mixing ratios of 100 ± 2.5 nmol mol^{-1}. At the maximum CO mixing ratio (i.e. ~ 150 nmol mol^{-1}), particle mixing ratios n_{nm} of about 6000 mg^{-1} (median value) were detected. Within a range of CO content between 85 and 130 nmol mol^{-1}, the n_{nm} (median) mixing ratios ranged consistently between 2000 and 10000 mg^{-1}, apart from the notable exception at about 100 nmol mol^{-1}. CO mixing ratios between 60 nmol mol^{-1} and 80 nmol mol^{-1} were detected just below or at tropopause levels (yellow to orange colours) coincidently with decreasing n_{nm} from about 3000 mg^{-1} to values below 1000 mg^{-1}. For CO mixing ratios below 60 nmol mol^{-1}, ~~however,~~ n_{nm} almost stagnates between 300 and 1300 mg^{-1}. At tropopause levels and aloft, the decreasing CO mixing ratio as well as abating NPF (expressed in decreasing n_{nm} values) ~~very~~ likely result from both the de~~pletion~~ gradation of CO (cf. von Hobe et al. (2020)) and the lacking supply of NPF precursor material by direct transport. According to von Hobe et al. (2020) any indication is missing that convection penetrated the tropopause during the StratoClim 2017 period. However, Lee et al. (2019) investigated the TTL-hydrating influence of an overshooting event that occurred in the Sichuan Basin about 1.5 days before the StratoClim measurements southbound of Kathmandu over northeast India (M-55 *Geophysica*, KTM 7 on 8 August, 2017).

Hence, there is no clear indication for a direct relationship between CO enriched (polluted) air and the NPF rate. ~~Nucleation mode particles in high n_{nm} mixing ratios (> 10000 mg^{-1} and up to 50000 mg^{-1}) persist only over hours in the atmosphere (cf. Section 4.5). Thus, on observation of such significantly elevated n_{nm}, the NPF must either be in full progress or must have happened~~

~~within a very few hours prior to the measurement. If CO mixing ratios (as indicator of the recent uplift of polluted air) had a direct impact on the NPF-rate, then the detections of elevated n_{nm} should coincide compactly correlate with correspondingly high CO mixing ratios. Conversely, high CO content does not necessarily imply strong NPF, as the limited time the particles persist in the nucleation mode does not allow for distinguishing a currently proceeding event of moderate NPF-rate from a strong NPF burst, which has occurred hours ago (cf. Section 4.5).~~

5.2 NPF and air mass origin in the boundary layer

The assignment of certain measurement sections of elevated n_{nm} to possible source regions ~~locations on the ground as possible~~of NPF precursors ~~source areas~~ is carried out in two steps:

(1) The backward trajectories were traced down to the boundary layer (BL) for each measurement point (cf. Section 3.3) at which NPF was detected ~~according to the passed criterion~~ (Figure 9~~Figure 9~~ a and b). In this way, the geographical position of the last BL contact of the air before the observations (1 Hz resolution) of elevated n_{nm} ($\gtrsim$ 300 mg^{-1}) is obtained throughout the StratoClim 2017 mission (Panel a). In addition, the geographical position of the trajectories' fastest uplift during their transport history was determined (Panel b).

(2) The ERA-5 reanalysis data were examined with regard to the transport time of the trajectories between the position in the BL and the coordinates of the measurement point (Figure 10~~Figure 10~~ ~~a~~ and b). The transport time is then coupled with the geographical position of the last BL contact of the air before the NPF observations (Panel a) and the position of the trajectories' fastest uplift in their transport history (Panel b).

~~The top two panels of Figure 9 (a and c) illustrate the geographic position of the air's last BL contact prior to the observations (1-Hz resolved) of elevated n ($\gtrsim$ 300 mg^{-1}) throughout the entire StratoClim 2017 mission. The bottom panels of Figure 9 (b and d) show the geographical coordinates where the air mass experienced the fastest uplift in its transport history towards each point of n detection. Of course, the accuracy of the individual coordinates should not be overestimated, for the reasons described in Section 3.3 and since the local resolutions of the observational data from in-situ measurements and of the reanalysis data are not equivalent. Particularly the spatial resolution of the reanalysis data is vertically variable. However, the~~

~~panels of Figure 9 convey two aspects: (1) how widespread the distribution of the air masses origins is within the BL, from where an influence on the composition of the air samples could have occurred, and (2) in which geographical region the high-reaching convection has efficiently lifted the material to the level of air sampling. The numerous NPF observations and the currently highest resolution level of the ERA-5 data set should allow for identifying a systematic relationship, if existing, between the observed NPF and the trajectories' contact to the BL.~~

According to the distribution of the trajectories' latest BL contact ~~(Figure 9 a)~~ with reference to the n_{nm} mixing ratio (Figure 9~~Figure 9~~ a), hardly any systematic structure is visible (the close-up views in Panels a.1 and a.2 provide a new scaling and arrangement of the points of identical data set). The possible source regions are distributed over the entire ~~monsoon~~ region almost independently of the NPF intensity. ~~Some of the trajectories'~~The last BL contact of some trajectories~~point to~~ was at locations far away from the monsoon region (e.g. in the West: the east coast of Africa and the Gulf of Aden; in the East: Indochina, the South China Sea and as far as the Philippine Sea). The entire possible source area of NPF precursors ranges from the north of India and the Arabian Sea, Pakistan, Afghanistan, Southwest China, Taiwan, the Philippines, and the Bay of Bengal. ~~South of ~ 10° N geographic latitude, the number of possible source regions decreases significantly.~~

Locations of ~~strongest~~ fastest vertical updraught are more compactly distributed (Figure 9~~Figure 9~~ b, close-up views in Panels b.1 and b.2) and better reflect the contours of an area where efficient convection~~of~~ frequently occurs within the monsoon region. Fastest updraught with simultaneously increased n_{nm} is found in the Kathiawar region on the Indian west coast towards the Arabian Sea, or in the far north of India (in the areas around Ladakh, Himachal Pradesh, and eastern Punjab). In areas of the central Tibetan Plateau, some sites were identified with elevated n_{nm}, where also the fastest vertical upward transport occurred. Finally, the shape of the Himalayan Mountains is traced by the locations with the fastest vertical air mass transport over a wide range of n_{nm}.

Also the shortest transport times from the BL are found around the Himalayan mountains and their foothills. Whereas the transport times from locations of air's last BL contact, which fall south of 25°N, west of 72°W, or east of 96°W, are rarely shorter than 10 days. In Figure 10~~Figure 10~~ (a and b, cf. also respective close-up view), the contour of the Himalayan mountain chain is

clearly reproduced by the distribution of the data points (transport times of less than ~ 5 days and fastest vertical updraught). Hence, for the duration of the StratoClim 2017 mission, the convective uplift ~~may largely have~~mainly occurred within the AMA. This more compact regional distribution of vertical uplift (Figure 10~~Figure 10~~ b) is possibly related to the occurrence of a *vertical conduit* for upward transport in the monsoon, as conjectured by Bergman et al. (2013). ~~Nevertheless, the almost homogeneous distribution of the *n* mixing ratios within the displayed region of strongest convective uplift does not allow for identifying specific locations as potential source regions of NPF precursors. Furthermore, Figure 9 b~~ Figure 10~~Figure 10~~ also indicates air masses of elevated n_{nm}, which have experienced convective uplift over Tajikistan and northern Afghanistan as well as over regions around the Yellow Sea, the Korean Peninsula or Japan, hence, far away from the AMA system.

~~With regard to the air mass transport time from the BL, the ERA-5 reanalysis data were examined over 50 days prior to the in-situ measurements (Section 3.3). For transport times exceeding 25 days, however, the data points in the Panels c and d of Figure 9 are displayed in grey. According to Figure 9 c, the air masses with the shortest transport times from the BL are found compactly around the region of the Himalayan mountain chain and its foothills. In Figure 9 c and d, the contour of the Himalayan chain is clearly reflected by the distribution of the data points (transport times of less than ~ 5 days and fastest vertical updraught). The highest *n* mixing ratios were not detected in air from this region (Figure 9 a). The distribution shown in Figure 9 c also indicates that in air masses from remote locations (Gulf of Aden, Arabian Sea; or Philippine Sea, South China Sea, Bay of Bengal) also strongly elevated *n* (> 10^4 mg^{-1}) were detected after comparatively long transport times of up to 25 days. Several other cases of elevated *n* are visible in Figure 9 a, for which the transport times from the BL even exceeded 25 days (grey points in Figure 9 c).~~ Both graphics, Figure 9~~Figure 9~~ and Figure 10~~Figure 10~~, ~~finally~~ show~~s~~ that the region of the air's last BL contact and the location of the fastest vertical uplift do not necessarily coincide. Similarly, the locations of the fastest updraught do not always match the shortest transport times, but for most cases in the immediate vicinity of the Himalayas this correlation is clearly visible from the StratClim 2017 data set. Ultimately, it cannot be excluded that, within the free troposphere, the air is subject to loading from various source regions (not

exclusively from the location of the last BL contact) prior to its convective uplift. Of course, this finding ~~may~~ complicates an unambiguous apportioning of NPF to specific source regions of precursors in the BL.

The vertical distribution of the n_{nm} mixing ratios as a function of the air mass transport time from the BL is shown in Figure 11~~Figure 11~~:

1) Above 380 K, almost all observations of enhanced n_{nm} are associated with air mass transport times of more than 12 days ~~(note that the evaluation of the reanalysis covers up to 50 days of transport time in total)~~. At 380 ± 3 K, none of the detected n_{nm} is connected to air mass transport times of less than 12 days. Several times higher n_{nm} (with 10^3-10^4 mg^{-1}) were detected below 380 K in air masses, which had experienced more than 25 days of transport time from the BL.

2) Below 380 K, the transport times are variably distributed over the altitude range between 350 K and 380 K. The air masses with shortest transport times are located in the height interval between 360 K and 370 K. As shown by a recently published investigation, these air masses have presumably reached the ~ 360 K level (altitude of the main convective outflow) very quickly by an effective convective transport and are then moved further aloft, towards 370 K, with much lower ascent rates (Vogel et al., 2019) due to the prevailing air mass uplift within the AMA.

3) On occasion, very short transport times were found with maximum n_{nm} at altitudes of about 367 K and 370 K. However, the highest n_{nm} are mostly not observed in air with such short transport times. Within 370 ± 3 K, the detected n_{nm} reach ~~almost~~ extreme values (~ 50000 mg^{-1}) in air with transport times of up to 15 days. Above 370 K and below 355 K none of the maximum n_{nm} is associated with transport times of less than 6 days, and here, the highest n_{nm} were detected in air with transport times of up to 25 days. Therefore, based on the observations and the trajectories analysed here, the altitude band of the main convective outflow is limited to a range between 355 – 370 K.

5.3 The relationship between NPF and convective outflow

For the following analysis, which is summarised in Figure 12~~Figure 12~~, the vertical distribution of the mean mixing ratios $\overline{n_{nm}}$ of respective NPF event~~s~~ (cf. Sections 0~~2.1.3~~ and 4.4) are juxtaposed with

a) a measure for the convective contribution to the composition of the probed air mass and

b) the mean transport time within the TTL since their release from the top of individual convective cells (cf. Section 3.4 for both variables).

Figure 12~~Figure 12~~ a broadly confirms the general understanding that the main outflow region of deep convection is well below the tropical tropopause (i.e. at 350 - 370 K) and ~~above~~aloft the ~~the tropopause the~~ air is still rising, but at a much lower vertical velocity. At altitudes above ~ 380 K, the observed NPF events with $\overline{n_{nm}}$ < 2000 mg^{-1} generally remain in the lower range of moderate intensity (cf. Section 0~~2.1.3~~), although there was one of the rare observations of overshooting convection up to levels ~ 385 K where NPF was detected in coincidence with ice cloud elements (cf. Weigel et al. (2021b)). Hence, if in exceptional cases the outflow region of deep convection extends above the 380 K-level, ~~which was even~~as indicated by ~~detected~~the presence of ice cloud elements, then high NPF rates are not necessarily to be expected. Below 380 K, ~~A~~about two thirds of all events ~~that occurred below 380 K~~ are connected to convective influence by more than 75 %. However, a remarkable proportion of observations below 380 K indicates convective contributions of less than 60 % and down to 25 %. Below ~ 375 K, mean mixing ratios $\overline{n_{nm}}$ of 1000-2000 mg^{-1} were associated with 100 % convective contribution, and mixing ratios of more than 10000 mg^{-1} were sometimes observed in air masses with ~ 30 % convective contribution.

For the observed NPF events, Figure 12~~Figure 12~~ b shows the mean age of the probed air masses since their release from the top of individual convective cells. Above ~ 380 K, the air escaped ~~at~~ the convection top mainly 12 days (or more) prior to its probing. Two events at ~ 382 K and at ~ 385 K, respectively ~~(e.g. likely connected to overshooting convection)~~, indicate a more recent convective uplift, within 5 days before the air was sampled. Despite the comparatively short transport times, here, the observed $\overline{n_{nm}}$ remained below 2000 mg^{-1}. At altitudes below ~ 380 K, the air predominantly resided within the TTL region for less than 5 days prior to the observation. Nevertheless, some of the comparatively intensive NPF events (with $\overline{n_{nm}}$ ≈ 7000 – 15000 mg^{-1} at ~~~ 373 K, ~ 365 K, and at~~ ~ 360 K – 375 K) were ~~also~~ observed in air, which has been released from associated clouds' top more than a week (and up to two weeks) prior to the measurements. It should be considered, however, that short air mass transport times within the TTL are indicated also for NPF events with minor convective contribution (< 50 %).

From the StratoClim 2017 data base emerges that NPF occurs at the lower TTL (i.e. below the tropopause) of the AMA in air masses that have been lifted by convection in time intervals ranging from 5 days to about two weeks. However, it remains unclear whether in some of the observed events the air samples were taken at a very advanced stage of NPF. Therefore, it can only be surmised whether or how often the short time period was missed during which NPF is detectable by aircraft-based measurements. Potential uncertainties remain to be considered in connection with the uncertainty of the reanalysis data and the representation of the transport history of the air masses.

6 Potential impact of gravity waves on vapours' supersaturation

~~The NPF precursor substances may primarily originate from sources on the ground and in the BL. The convective uplift doubtlessly constitutes one of the most effective transport mechanisms for lifting the material to altitudes of the lower TTL. As the prerequisite for NPF to take place within the TTL, however, the gaseous precursor material~~

~~a) must survive the convective uplift and must be released in sufficient quantities in the outflow region and at the lower TTL, and~~

~~b) in the TTL region, the NPF precursor material is required to be enriched to sufficient supersaturation.~~

If the lifted precursor material would be suitable for NPF and sufficiently enriched right upon release from the convective outflow~~If the uplifted precursor material was suitable for NPF immediately after its release from the convective outflow~~, the relationship between elevated n_{nm} and convective transport should be clearer than observed (cf. Section 5). The lack of an unambiguous relationship ~~may~~ indicates that the recently transported material is deposed in the TTL but not immediately consumed, e.g., by NPF although the presence of ammonium in the aerosol phase (Höpfner et al. (2019); Wang et al. (2020)) or organics should promote the NPF of H_2SO_4 in the TTL even at low supersaturations (Metzger et al. (2010); Kerminen et al. (2010); Kirkby et al. (2011); Kürten (2019);(Wang et al., 2020)).

The supersaturation required for initiating NPF could temporally ~~also~~ result from local cooling. ~~It is conceivable and the basis of the hypothesis set out hereafter that the NPF process and its~~

~~intensity is locally triggered, e.g., by gravity waves.~~ Gravity waves (GWs) represent low-frequency inertial perturbations of the initial atmospheric state. Such a perturbation is expressed particularly by a change in velocity of the vertical wind component. The passage of a GW is associated with a change in the vertical displacement of an air parcel and thus causes locally an adiabatic heating/cooling by a certain absolute value ΔT.

Piani et al. (2000) provided simulations of GWs initiated by deep convection~~s~~. Their studies reveal a concentric propagation of GWs at altitudes above 15 km and up to ~ 40 km~~, which was effected by convective systems underneath. H~~ with ~~orizontal~~ wavelengths~~-~~ in the horizontal of about 40 km and ~~vertical wavelengths~~ of ~ 4 - 7 km in the vertical~~ were ascertained (*ibid.*)~~. Similar ~~wavelengths~~ results were found to be typical by other simulation studies concerning ~~the~~ GW propagation ~~of GWs, which have been initiated, e.g., by convection~~ at mid-latitudes (Song et al. (2003) and Chun and Kim (2008)) or ~~by~~ in the tropic~~sal convection~~ (Lane and Moncrieff, 2008). Investigations related to GWs in connection with the monsoon are sparse, e.g. Wright and Gille (2011) and Ern and Preusse (2012) used satellite observations (High Resolution Dynamics Limb Sounder) which, however, are limited to detections of GWs with horizontal wavelengths greater than ~ 300 km. Despite the numerous observational studies concerning GW properties (Alexander et al., 2010), the indirect retrieval of GWs' horizontal wavelengths remains uncertain by a factor of two (or more), whereas instrumental limitations inhibit the GW detection at horizontal wavelengths smaller than 100 km.

~~Observations using data sampled on commercial aircraft (Fritts and Nastrom, 1992) reported ~ 1 K2 temperature variances (or rather variance enhancements by a factor 6.1 compared to undisturbed conditions) on passages of convection-induced GWs through the tropopause region.~~ Based on radiosonde measurements (Vincent and Alexander, 2000), a 6-year averaged amplitude of 1.5 K is reported as an effect of GWs, with a single-case example of ~ 4 K-amplitude around 20 km altitude in the tropics. ~~Hence, GW-induced temperature anomalies are observable up to a maximum ΔT of ~ 4 K, although smaller-scale perturbations occur more frequently.~~ ~~GW-induced negative temperature anomalies from an initial state T0 increase a precursor's~~ the ~~saturation ratio~~ of any gaseous substance, and in particular the degree of supersaturation of NPF ~~precursors~~~~and the effect of such an anomaly on the degree of supersaturation applies qualitatively to any gaseous substance~~. ~~Also in the homogeneous heteromolecular nucleation of more complex systems, the respective gas species or gas mixtures convert into particles as soon~~

~~as the supersaturation exceeds the level required for the occurrence of NPF. Such more complex systems of precursor substances, e.g. with ammonia, nitric acid and/or organic components, are most likely involved in the formation process and promote NPF (Kirkby et al. (2011); Kürten (2019); Wang et al. (2020)).~~

Satellite images over the Indian subcontinent (e.g. from MSG-1 or HIMAWARI, cf. https://www.eorc.jaxa.jp/ptree/index.html) indicate quite frequent occurrences of convective plumes in the sampling areas ~~and~~ during the StratoClim 2017 mission period, which occasionally ~~even~~ arranged in chains of convective cells along the Himalayan foothills. The StratoClim flight KTM 6 on 06 August 2017 enabled NPF observations immediately connected to convection, which ~~shot~~penetrated ~~-~~through the flight level on passage at constant flight altitude. The ~~C~~corresponding part of the time series shown in Figure 13~~Figure 13~~ covers the probing period in the air sector over Bangladesh and the Bay of Bengal (cf. Figure 1~~Figure 1~~). Two phases of NPF observations are highlighted (~~oblique~~ hatched areas in Figure 13~~Figure 13~~), immediately before and after the period between 09:20 and 09:30 (UTC), during which the flight altitude changed from 16.2 km to about 13.8 km with subsequent re-ascent to 16.2 km. The manoeuvre above the northern part of the Bay of Bengal also marks the turning point of the mission flight path and the two flanking NPF phases were encountered over the mainland near the coastlines of East India and Bangladesh (cf. Figure 1~~Figure 1~~ b). The outbound and return sections of the flight passed through the same convectively active region, and the same convective system was likely probed at opposite positions.

Within the limits of the displayed time series (Figure 13~~Figure 13~~ a) constant flight altitude and pressure level were maintained, except for the turning manoeuvre, which was disregarded in ~~the~~is therefore not subject of following discussion. The mixing ratios n_6, n_{10} and n_{15} coincidentally exhibited increased values of variable strength (Figure 13~~Figure 13~~ b)~~.~~ ~~The productivity of observed NPF events is derivable from the mixing ratio of the~~ nucleation-mode ~~particles n_{nm} (Figure 13 c),~~ whereas during both NPF phases the particle mixing ratios n_{nm} ~~reached peak values of more than 20000 mg^{-1} or they often remained clearly elevated~~ are elevated (> 10000 mg^{-1}) or peak up to values of more than 20000 mg^{-1}. The course of n_{nm} is not mirrored ~~at all~~ by the CO signal (Figure 13~~Figure 13~~ d), e.g. n_{nm} is at maximum values when CO is still at intermediate levels of ~ 110 nmol mol^{-1}. ~~In accordance with the results discussed in Section 5.1 and illustrated in Figure 8, high n seems not directly coupled to the supply of~~

~~pollutants by convective transport (Figure 13 c and d).~~ ~~Furthermore, i~~In both NPF phases, the peaks of air's CO content (130 - 140 nmol mol^{-1}, Figure 13~~Figure 13~~ d) were accompanied by increasing mixing ratios n_{10}nv by a factor of up to two compared to the background (Figure 13~~Figure 13~~ b), indicating the passage through the convective outflow plume, which also contained non-volatile aerosol material that was lifted together with gaseous pollutants.

During the periods of the NPF observations, however, the ambient air temperature T_{amb} (Figure 13~~Figure 13~~ e) visibly fluctuates in the order of ± 1 K around the respective mean temperature (T_{mean} = 193 K with standard deviation below 1 K). Over the NPF period, the time series of the temperature fluctuation (T_{amb} - T_{mean}, Figure 13~~Figure 13~~ e) exhibits the shape of a wave. ~~In reference to the first NPF phase and assuming an average airspeed of 170 m s^{-1} throughout this period, the time series of the temperature fluctuation covers a peak-to-peak duration, which converts into a horizontal distance of ~ 90 km.~~

Figure 14~~14~~ shows close-ups of the time series covering slightly more than one hour of measurement on level flight, including the two periods of observed NPF (Panels a and b, respectively). The curves exhibit the untreated 1 Hz temperature data set (T_{1Hz}) and the noise-filtered data set (T_{201})~~, for which the 1 Hz data was cleaned of statistical scattering~~. The filtering was applied using a running average over 201 data points (see Appendix B for details). The filtered data (T_{201}) is additionally approximated with an overlaid wave fit (cf. Appendix B and Table 2), which aimed at the requirement to reproduce the temperature variation, in particular during the periods of NPF observation. The noise level over the intervals of the mapped time series holds a fairly constant standard deviation σ of about ± 0.25 K~~.~~. ~~I~~In maxima, the scattering peaks slightly above the 3 σ noise level (i.e. about ± 0.75 K), which likely accounts for the largest proportion of uncertainty in the temperature data for this measurement period. The applied fit functions reproduce the wave-like character of the temperature fluctuation during two NPF events with estimated wavelengths between 70 km and 100 km (for the higher frequency, while in the range of 400 km for the lower frequency). The quality of approximating the noise-reduced data by overlaid wave fit provides ~~strong~~ indications that the observed temperature fluctuation is subject to a wave that coincides ~~surprisingly~~ well with the occurrence of NPF.

It would go beyond the scope of this study to clearly attribute this temperature fluctuation to the GW activity initiated by ~~a~~ one specific or several~~specific~~ convective systems. However, the

amplitude and wavelength of the observed fluctuation correspond qualitatively and quantitatively to the values typical for GWs. Simplified estimates reveal that an increase of the H_2SO_4 saturation ratio by a factor of about 1.75 – 2 readily occurs when the initial ambient temperature (e.g. at $T_0 \approx$ ~~210~~ 190 K) drops by 2 K (cf. Appendix B). If NPF is initialised by a negative temperature anomaly under supersaturated conditions, the newly formed nucleation-mode particles hardly evaporate at re-rising temperatures (e.g. when the GW-induced temperature anomaly becomes positive).

The horizontal extent of GW-induced temperature anomalies, which can range from a few to hundreds of kilometres, is generally comparable with the magnitude of the horizontal extent of observed NPF fields (cf. Sections 0~~2.1.3~~ and 4.3 as well as Figure 5~~Figure 5~~ c). Since the time offset between NPF observation and NPF initiation is not exactly known, it is not straightforward to connect individual NPF events to specific incidents of GW-induced temperature anomalies. Moreover, during the monsoon season, several widely distributed, convective systems may induce GWs at the same time and the resulting, spatially propagating, temperature anomalies could interfere at TTL heights. The amplification of temperature anomalies inherent with such interferences is neither locally resolvable nor quantifiable. Hence, GW-induced temperature anomalies ~~may~~ can additionally promote the occurrence of NPF~~, particularly in cases, in which the enhancement of the NPF precursor saturation ratio, as prerequisite for NPF initiation, is not ascribable to direct (convective) uplift from the surface~~.

~~7~~

~~8~~7 Summary and Conclusions

Between 27 July and 10 August 2017 the airborne StratoClim 2017 mission took place in Kathmandu, Nepal, with eight mission flights (~ 22.5 hours of COPAS measurement time above 10 km, $\theta \gtrsim 350$ K) up to altitudes of 20 km ($\theta \approx 475$ K) with the Russian high-altitude research aircraft M-55 *Geophysica*. The presented analysis comprises the description and discussion of numerous events of New Particle Formation (NPF), which were observed in the UT/LS region of the Asian Monsoon Anticyclone (AMA) over northern India, Nepal and Bangladesh.

~~During the StratoClim 2017 mission, a~~In total, a duration of 2 hours and 38.5 minutes was spent under NPF conditions in the region of the Tropical Tropopause Layer (TTL), where enhanced quantities of nucleation-mode particles of up to ~ 50000 mg^{-1} (≈ 11000 cm^{-3}) were detected at

heights of 15 – 16 km (~ 370 K). The majority of NPF observations with high numbers of nucleation-mode particles (6 nm < d_p < 15 nm) were observed below the tropopause~~at the lower TTL~~ (~ 12-16 km, ~ 355 – 380 K), at the lower TTL ~~and below the tropopause~~. ~~Nevertheless,~~ NPF with ~~enrichments of~~ intermediate (~ 1000 – 2000 mg^{-1}) or low (~ 300 – 500 mg^{-1}) mixing ratios of nucleation-mode particles were also observed ~~at levels~~ around the tropopause (~ 380 K) and up to about 17.5 km altitude (400 K). The frequency of intense NPF observed during StratoClim 2017 exceeds all previous NPF detections with COPAS in the TTL over Brazil, Australia, and West Africa (TROCCINOX 2005, SCOUT-O3 2005, SCOUT-AMMA 2006, cf. Borrmann et al. (2010); Weigel et al. (2011)). The maximum of detected nucleation-mode particles (~ 50000 mg^{-1}, correspondent to ~ 11000 cm^{-3} under ambient conditions at 360 K < θ < 370 K) is in comparable orders of magnitude to the earlier COPAS observations (*ibid*). ~~Moreover, t~~The horizontal extent of the NPF fields during StratoClim 2017, ranging from a few hundred metres to about one hundred kilometres, well compares to previous COPAS observations in the tropics. ~~The frequency of NPF observations during StratoClim 2017 over durations of ~ 10 seconds (< 1.5 km horizontal distance) and with *n* peaking up to 50000 mg^{-1} indicates a very effective and spacious source region of aerosols at TTL levels within the AMA. The numerous encounters of enhanced *n* over several consecutive minutes (cf. Section 4.3 and Figure 4) indicate the NPF occurrence over extended fields of approximately 10 to 100 km (at event durations of 60 - 600 seconds).~~

Mainly due to coagulation, ~~T~~the persistence of nucleation-mode particles (d_p < 15 nm) in the presence of the background aerosol population is ~~largely determined by coagulation and~~ limited to few hours only. Within the supersaturated environment under NPF conditions, co-condensation of gaseous species other than ~~those involved in~~ NPF precursors~~may~~ further promotes the growth of nucleation-mode particles. The comparatively short persistence of the particles in the nucleation-mode size range implies:

- Within 2 hours ~~After~~ after a NPF event, the number concentration of nucleation-mode particles decays due to coagulation by more than one order of magnitude ~~within 2 hours~~.
- About 3-4 hours after a NPF event, the reduced number of nucleation-mode particles impedes the identification of NPF events based on aircraft-borne *in-situ* measurements.

- ~~The interpretation of l~~Low and intermediate ~~amounts~~ numbers of nucleation-mode particles ~~is limited, as they may~~ result from either moderate and just proceeding NPF or from an event with elevated NPF-rate that has phased-out over more than two hours before the measurement.
- Identified NPF events with ~~H~~high amounts of nucleation-mode particles i.e. (> 10000 mg^{-1})~~, however, indicate that NPF had~~ have occurred very shortly (less than one hour) prior to the measurement or ~~was~~ are just proceeding when detected.

The supersaturated conditions, under which NPF occurs~~, however,~~ also favour the co-condensation of gaseous substances (Yu et al., 2017). Whether coagulation or condensation predominantly contributes to the composition of the background aerosol remains open. Most likely, both processes impact the formation and persistence of the ATAL (Vernier et al. (2011a), and see also Höpfner et al. (2019); Mahnke et al. (2021)), which was mainly attributed to the uplift of pollution from the boundary layer ~~by means of balloon-borne and satellite-based observations~~ (Vernier et al. (2018); Brunamonti et al. (2018); Hanumanthu et al. (2020)). ~~In general~~

Generally, a refractory core with diameter greater than 10 nm was detected in almost every second particle above 395 K and up to 475 K. In addition to the local particle source by NPF, additional particulate material is vertically transported ~~This indicates the supply of other particulate material due to~~ by the updraught within the AMA (cf. also Section 6)~~, although meteoric particles from higher altitude~~s ~~whereas at maximum ceiling~~At altitudes above 18 km, ~~during StratoClim 2017~~ the contribution of meteoric particles from further aloft was found by means of *in-situ* aerosol mass spectrometry during StratoClim 2017 (Schneider et al., 2020)~~ may also play a role~~.

~~An~~At altitudes of up to 17.5 km, the fresh particles from NPF are in place for being lifted by a sufficiently effective transport mechanism to indirectly supply ~~of~~ the stratospheric (Junge) aerosol layer ~~(Junge et al., 1961)~~. ~~at an altitude of ~ 25 km by freshly formed particles (at altitudes of up to 17.5 km) seems possible if a sufficiently effective transport mechanism is available.~~ However, whether aerosol material subsides from TTL levels to mid-tropospheric altitudes and possibly contributes to cloud formation, as suggested by Andreae et al. (2018) to happen in the Amazon region, depends on the efficiency of downward transport, and on the

aerosol's capability as CCN. Condensation of gaseous species other than those involved in the NPF process, and internal chemical conversion of various solutes within a particle ~~could~~ influence the aerosols' CCN capabilities. The required transport times to reach altitudes far above or below the TTL ~~appear long (~~range over several days ~~and~~ to weeks~~) compared~~ and stay in contrast to the short persistence (hours) of nucleation-mode particles.

~~Three different approaches were used to correlate the occurrence frequency of most recent NPF (most enhanced *n*) with possible source regions of precursor material in the BL and to find a direct connection of NPF to recent convective uplift and air mass transport times. Exceptionally elevated abundances of particles (about ten to hundred times above the level of background aerosol concentrations) are used as indication for very recent occurrence of NPF. Intermediate or lower number densities of particles could lead to ambiguous conclusions (cf. Section 4.5):~~

Moreover, the StratoClim 2017 measurements revealed:

(1) ~~The measurements indicate~~ that highest n_{nm} values were predominantly found to coincide with intermediate to elevated CO mixing ratios of ~ 100 nmol mol^{-1}. Beyond that ~~level~~, the mixing ratio of nucleation-mode particles (~ 700 – 20000 mg^{-1}) is largely independent of the CO content (between 80 and 145 nmol mol^{-1}) of the air at the lower TTL.

(2) The most intensive uplift of air was confirmed to occur over the Himalayan mountain chain and its foothills. However, particular source regions of NPF precursors were not ascertainable within the BL. ~~Furthermore, n~~No indication was found that the most intense NPF was connected to short durations of air mass transport from the BL into the TTL.

(3) The convective contribution to the air mass composition did not ~~immediately~~ determine the intensity of the observed NPF. The release of the precursor material in the outflow region of the convective top had occurred up to 6 days before the NPF observation. Occasionally, however, air mass residence times of more than 6 days and up to 14 days were found at TTL levels prior to the NPF detection while the entire data set covers residence times from ~ 3 hours to about 26 days.

~~Consequently, f~~For the period of the StratoClim 2017 mission, the observed ~~intensity of~~ NPF rates ~~is~~are not unambiguously attributable to a) a specific source region ~~on the ground or~~ in the BL, or b) the effectiveness of the convective vertical transport, or c) the recent release of NPF-capable material from the convective outflow.

Nevertheless, it ~~should be~~is the convective uplift, which intermittently supplies the lower TTL by NPF precursor material. At altitudes well above tropopause levels, such an immediate supply by convection is lacking and could alternatively only proceed by the slow uplift superimposed on the anticyclonic ascent of the AMA (~ 1 K per day, Vogel et al. (2019); von Hobe et al. (2020)). ~~Generally, the question arises whether air mass transport and supply by convective updraught alone are sufficient to increase precursors' supersaturation such that NPF is initialised.~~

~~At TTL levels in AMA, diabatic cooling by emission of infrared (IR) radiation constitutes a spatially large-scaled process that potentially increases the supersaturation of an NPF precursor system, but which occurs mainly during night hours, i.e. in the absence of solar irradiation.~~ Alternatively, adiabatic cooling~~, however,~~ could induce sufficient supersaturation of a NPF precursor~~ and thus play a role as a trigger for NPF.~~ e.g. due to ~~T~~temperature anomalies associated with gravity waves (GW). Presented case study based on a continuous level flight segment (flight KTM 6 on 06 August 2017), revealed wave-like temperature anomalies with a peak-to-peak amplitude of ΔT = 2 K and a horizontal wavelength of 70 – 100 km, which matched ~~surprisingly~~ well with two independent NPF events. ~~could very well increase the supersaturation of a precursor by that crucial bit above the NPF threshold. Interfering gravity waves, such as those likely initiated during the convectively very active Asian monsoon season, may increase the probability that occurring temperature anomalies are adequately large. Furthermore, the~~Hence, the vertical propagation of GW-induced temperature anomalies ~~could~~ can initialise NPF above tropopause levels, a) where ambient air temperatures re-increase with altitude (from observational data with $\Delta T \approx 1.5$ K per $\Delta\theta = 10$ K), which principally counteracts the supersaturation of a precursor, and b) where in the absence of ~~overshooting~~ deep convection a direct supply of precursor material from below is lacking.

~~The frequency of NPF observed during StratoClim 2017 exceeds all previous NPF detections with COPAS in the TTL over Brazil, Australia and West Africa (TROCCINOX 2005, SCOUT-O3 2005, SCOUT-AMMA 2006, cf. Borrmann et al. (2010); Weigel et al. (2011)). The maximum of detected particles (~ 50000 mg^{-1}, correspondent to ~ 11000 cm^{-3} under ambient conditions at 360 K < θ < 370 K) is in comparable orders of magnitude to the earlier COPAS observations (*ibid*). Moreover, the horizontal extent of the NPF fields during StratoClim 2017, ranging from a few hundred metres to about one hundred kilometres, well compares to previous COPAS observations, although caveats inhere in the distinction of individual but closely adjacent NPF~~

~~fields due to the COPAS measurement resolution in conjunction with the flight speed of the M-55 *Geophysica*.~~

The observations made during StratoClim 2017 ~~indicate~~ demonstrate that frequent NPF with high production of nucleation-mode particles is capable of directly affecting the extent and persistence of the Asian Tropopause Aerosol Layer (ATAL). The continuous supply of freshly formed aerosol material, which coagulates both internally and with the background aerosol, and which itself provides a surface for the condensation of supersaturated gaseous substances, contributes significantly to the available aerosol material that composes the ATAL. In this case, the chemical composition of the ATAL aerosol ~~may~~ includes significant fractions of the material, which was previously involved in the NPF process and the particles' condensational growth, ~~but this~~ which is subject to further investigation using the StratoClim 2017 data set.

Data availability:

The data shown in this study are available at the StratoClim campaign database at

https://stratoclim.icg.kfa-juelich.de/AfcMain/CampaignDataBase

or they may be provided by respective PI upon request

Author contribution

RW evaluated and analysed the data, created the figures, and draft~~t~~ed the manuscript with contributions by CM, MB, and AD. SB participated in the data analyses and the manuscript drafting. The code of the coagulation simulation was provided by BPL, and the code was adapted by MB while the calculations were performed by CM. BV, FP contributed with meteorological re-analyses, BV, SiB, and BL performed the air mass trajectory analyses. SV and FD'A took care of the CO data. UCSE data were delivered by GB. The manuscript was ~~critically~~ reviewed by CM, MB, AD, BV, FP, SV, FD'A, SiB, BL, BPL, and SB.

Competing interests

The authors declare no competing interests.

Acknowledgements

The contributions from the technical staff at the workshops of the MPI for Chemistry and the Institute for Physics of the Atmosphere (Mainz University), as well as the Myasishchev Design Bureau (MDB) were essential. In particular, we acknowledge support of T. Böttger, M. Flanz and W. A. Schneider. We thank Y.-H. Kim, P. Spichtinger, H. Tost, M. Szakáll, A. Theis, and A. Miltenberger, T. Thornberry and the ACCLIP-team for very helpful discussions. Many thanks to T. Peter for the planning of flight KTM 6 on 06 August 2017. ~~In particular, we acknowledge~~

~~support of T. Böttger, M. Flanz and W. A. Schneider.~~ The extraordinary commitment of F. Stroh in realisation of the campaign and the leadership of the entire StratoClim project by M. Rex are gratefully acknowledged. We very much thank the MDB crew and the M-55 Geophysica pilots. Some of our research leading to the presented results received funding from the European Research Council under the European Union's Seventh Framework Program (FP/2007-2013)/ERC Grant Agreement No. 321040 (EXCATRO). The StratoClim project was funded by the EU (FP7/2007–2018 Grant No. 603557) and also supported by the German "Bundesministerium für Bildung und Forschung" (BMBF) under the joint ROMIC-project SPITFIRE (01LG1205A). ~~R. Weigel gratefully acknowledges the support of the Transregio Collaborative Research Centre CRC/TRR301 "TPChange", funded by the German Research Foundation (DFG), enabling for which this study provides preparatory work for subproject B02 "BrIdging Surface emissions, Transport and UTLS Matter (BISTUM").~~ The work presented includes contributions to the China-NSFC-DFG 2020 project ATALtrack (BO 1829/12-1 and VO 1276/6-1). We explicitly thank the officials of the Nepalese government authorities, research institutions, and Tribhuvan Airport as well as of the German Embassy for their extraordinary support and hospitality, which enabled our field campaign and research.

Appendix A : The detection of non-volatile particles with COPAS

COPAS includes a vaporiser based on an established and commonly used technique. One of the four COPAS channels is equipped with a heated stainless steel tube (at ~ 270°C) to vaporise volatile compounds upstream of one of the particle detectors. The specific heating temperature is chosen with the aim to vaporise mainly stratospheric particle species, which typically consist of aqueous solutions of sulphuric acid (H_2SO_4-H_2O) and/or nitric acid (HNO_3-H_2O), which reportedly volatilise at 180°C (Rosen, 1971). In addition, most of volatile and several semi-volatile organic compounds can evaporate at colder temperatures than 270°C. Conversely, this means that an undeterminable proportion of semi-volatile and probably highly oxidised organics, whose role as agents in NPF has been identified by Kurtén et al. (2008) or Riccobono et al. (2014), can pass through the preheater without being significantly altered. Downstream of the heated tube section, the re-condensation of evaporated species is not completely excludable. Due to the high diffusivity of e.g. H_2SO_4 molecules (a factor of up to 0.5 of the diffusivity of H_2O, cf. Tang et al. (2014)), the re-condensation is expected to occur predominantly at the tube's inner walls, since thermophoresis drives the vapour molecules from the previously heated air sample towards the cold walls. Such a re-condensation affects the particles' size not their number, and condensation on the largest of the non-volatile residues is favoured over the smaller ones (i.e. those with $d_p < 10$ nm). The working principle of the COPAS aerosol vaporiser was demonstrated by means of laboratory experiments with pure H_2SO_4-H_2O particles of several sizes and at pressure conditions between 70 – 300 hPa (Weigel et al., 2009); more than 98 % of the sub-micrometre sized H_2SO_4-H_2O particles were volatilised. As the refractory material, which could be detectable with COPAS, is unlikely to be generated by the heater itself, such

instrumental artefacts are largely excluded. To avoid artefacts as a result, e.g., of re-suspension of aerosol material, which had been deposited on the tube's inner walls during previous operations, the sample lines were flush-cleaned with ethanol and distilled water, at least before every second mission flight. Inefficiencies of the vaporiser, e.g. due to diminished heat transfer from the tube's inner wall to the passing aerosol particles, particularly at low atmospheric pressures, would cause the number (fraction) of detected refractory particles to be unexpectedly high (≈100 %) over extended measurement periods, which was not observed throughout the field missions (cf. Borrmann et al. (2010); Weigel et al. (2011)). Conversely, instrumental artefacts inherent with the vaporiser's tube length, e.g. particle loss, would lead to comparatively low number concentrations of detected refractory particles. Diffusional loss effects increase with decreasing pressure, but thermophoresis counteracts the particles' diffusion towards the hot tube walls. With the same vaporiser system, Weigel et al. (2014) observed rising mixing ratios of refractory aerosol, most likely from meteoric ablation, with altitude at stratospheric levels inside the polar vortex, while outside the vortex the amount of refractory aerosols nearly stagnated over the corresponding altitude range, additionally confirming the principle function of the vaporiser.

Appendix B: Case study analysis of observed temperature anomaly

For analysing the observed temperature anomaly in the time intervals of the NPF events a running average is used as filter to suppress the high-frequency noise on the temperature data. The running average over 201 measurement points (i.e. over 100 data points before and 100 data points after each 1 Hz-temperature measurement) is used; Figure A- 1~~1~~ illustrates the effectiveness of the filtering. As a result of subtracting the low-pass filtered temperature data (T_{201}) from the initial 1 Hz-resolved temperature data (T_{1Hz}), the high-frequency noise remains (red dots in Figure A- 1~~1~~). The noise scatters around the zero level with a maximum amplitude of about ± 0.75 K. The filtering by the running mean turns out as equally effective inside and outside the observed NPF events with ~~alleged~~presumed temperature fluctuation. The indicated reference lines for the ± 1 σ and ± 3 σ levels (where σ denotes the standard deviation) illustrate the noise amplitude, which remains fairly constant (during NPF and away from observed NPF events) over the entire period and also almost within the ± 3 σ - range. The course of the T_{201} curves thus represents the temperature fluctuation by excluding the noise, which underlies the measurement. The T_{201} curve is approximated by a~~n overlaid~~ wave fit (T_{Fit})~~, which aims at~~ for

reproducing the temperature fluctuation in the filtered data set (T_{201}) particularly during the periods of NPF observation (cf. Section 6 and Figure 14~~14~~).

The basic form of the ~~overlaid~~wave fit function is:

$$f\ (x, a, b, c, d) = d + a \cdot \sin(b\ x + c)\_ \qquad \textbf{A- 1}$$

with

x = horizontal distance derived from time UTC, day seconds, and mean airspeed,
a = the amplitude
b = the frequency
c = the phase shift
d = the offset

For each of the two time periods with identified NPF, an individual fit was determined with the parameters from Table 2 and each fit consists of a sum of two functions of the type defined in Equation A-1. During the NPF event the difference between the two curves, T_{201} and T_{Fit} (Figure A- 1~~1~~), shows, that the overlaid wave fit approximates the filtered data with a smaller deviation than given with the ± 1 σ - noise level. ~~Moreover, for completeness, t~~The difference between the 1 Hz-temperature signal and the wave fit is also shown in Figure A- 1~~1~~. During the NPF event, the subtraction of the wave fit from the 1 Hz-data has almost the same effect as the subtraction of the filter T_{201} from T_{1Hz}, therefore, in the NPF period, the deviation between the two sets of data (T_{1Hz} - T_{Fit}) corresponds mainly to the noise of the temperature measurement. Away from the NPF event, the deviation of the wave fit from T_{1Hz} and T_{201} increases as the approximation of the temperature data by the wave function was constrained to the NPF period.

Appendix ~~B~~C: The impact of a temperature anomaly on the saturation ratio of H_2SO_4

~~Gravity waves constitute a perturbation in several physical parameters, in particular a perturbation in vertical velocity. Since each vertical velocity causes an adiabatic vertical displacement, t~~The passage of a gravity wave is associated with adiabatic heating/cooling by a certain amount ΔT. According to Vincent and Alexander (2000) (cf. also Section 6), the maximum realistic value of ΔT is ~ 4 K. Smaller temperature perturbations occur more frequently. An air parcel at pressure p_0 and temperature T_0, which is vertically and adiabatically displaced, changes its pressure and temperature to the new values p and $T = T_0 + \Delta T$. The question arises as to how temperature anomalies influence the occurrence of NPF. In this context, NPF is initialised when

the saturation of a nucleating gas or gas mixture exceeds a certain level. Pure sulphuric acid is certainly not the exclusive gas species involved in NPF, but if temperature anomalies sufficiently affect the saturation ratio of pure H_2SO_4, then additional agents such as ammonium (Höpfner et al., 2019) or organics (Kürten, 2019) could more readily favour the initiation of NPF.

Adiabaticity of the process is presumed and by approximating the gas constant $\mathbf{R}$ and the heat capacity $\mathbf{c}_p$ with the values for dry air ($\mathbf{R} \approx \mathbf{R}_a$, and $\mathbf{c}_p \approx \mathbf{c}_{pa}$), the ideal gas equation can be converted such that the mixing-ratio q_{H2SO4} of sulphuric acid is related to its partial pressure p_{H2SO4}. Since the conditions within the AMA change rather slowly, the mixing of air masses is considered as negligible. Hence, the concentration of each gas species within the air parcel remains invariant to the vertical displacement. In the following, $p_{H2SO4,\,0}$ is the sulphuric acid partial pressure within the unperturbed air parcel. Denoting the saturation vapour pressure of sulphuric acid by p_{sat}, the ratio of the saturation ratio of the unperturbed air parcel and the displaced air parcel reads as

$$\frac{S}{S_0} := \frac{\frac{p_{H2SO4}}{p_{sat}(T)}}{\frac{p_{H2SO4,0}}{p_{sat}(T_0)}} = \frac{p_{H2SO4}}{p_{H2SO4,0}} \frac{p_{sat}(T_0)}{p_{sat}(T)}$$

$$= \frac{p}{p_0} \frac{p_{sat}(T_0)}{p_{sat}(T)}$$

$$= \left(\frac{T}{T_0}\right)^{\frac{c_{pa}}{R_a}} \frac{p_{sat}(T_0)}{p_{sat}(T)}$$

$$= \left(\frac{T_0 + \Delta T}{T_0}\right)^{\frac{c_{pa}}{R_a}} \frac{p_{sat}(T_0)}{p_{sat}(T_0 + \Delta T)}$$

$$= \left(1 + \frac{\Delta T}{T_0}\right)^{\frac{c_{pa}}{R_a}} \frac{p_{sat}(T_0)}{p_{sat}(T_0 + \Delta T)}$$

$$\approx \frac{p_{sat}(T_0)}{p_{sat}(T_0 + \Delta T)} \quad . \qquad \text{A- 2}$$

Figure A- 2~~2~~ exhibits the quotient $\frac{S}{S_0}$ (~~for~~ i.e. the factorial increase of the saturation ratio S in reference to an initial saturation ratio S_0 at undisturbed conditions, including supersaturated states) for several initial states of ambient air temperature T_0 (from 185 K to 250 K) and for a range of temperature anomalies with ΔT of up to 4 K. It is to be emphasised that these

calculations relate specifically to the impact of temperature anomalies on the supersaturation of pure H_2SO_4. These estimates based on ordinary precursors (i.e. H_2SO_4-H_2O) do not allow for conclusions concerning the NPF efficiency of complex systems of precursor compositions (e.g. including ammonia or organics). The demonstrated effect, however, is qualitatively transferable to any gaseous substance while the nucleation of particles from the gas-phase requires sufficiently high saturation ratios of the respective species or gas mixture and may be of particular interest in the context of the CLOUD experiments at CERN with H_2SO_4 (cf. Stolzenburg et al. (2020)) under variable conditions and various admixtures. ~~Therefore, it is conceivable that NPF is even better promoted by gaseous agents (including ammonia and/or organics) if, in addition, the saturation ratio of the precursor composition is increased by a sudden temperature anomaly due to a passing GW wave.~~

References

Alexander, M. J., Geller, M., McLandress, C., Polavarapu, S., Preusse, P., Sassi, F., Sato, K., Eckermann, S., Ern, M., Hertzog, A., Kawatani, Y., Pulido, M., Shaw, T. A., Sigmond, M., Vincent, R., and Watanabe, S.: Recent developments in gravity-wave effects in climate models and the global distribution of gravity-wave momentum flux from observations and models, Q J Roy Meteor Soc, 136, 1103-1124, 10.1002/qj.637, 2010.

Andreae, M. O., Afchine, A., Albrecht, R., Holanda, B. A., Artaxo, P., Barbosa, H. M. J., Borrmann, S., Cecchini, M. A., Costa, A., Dollner, M., Fütterer, D., Järvinen, E., Jurkat, T., Klimach, T., Konemann, T., Knote, C., Krämer, M., Krisna, T., Machado, L. A. T., Mertes, S., Minikin, A., Pöhlker, C., Pöhlker, M. L., Pöschl, U., Rosenfeld, D., Sauer, D., Schlager, H., Schnaiter, M., Schneider, J., Schulz, C., Spanu, A., Sperling, V. B., Voigt, C., Walser, A., Wang, J., Weinzierl, B., Wendisch, M., and Ziereis, H.: Aerosol characteristics and particle production in the upper troposphere over the Amazon Basin, Atmos Chem Phys, 18, 921-961, 10.5194/acp-18-921-2018, 2018.

Barth, M. C., Stuart, A. L., and Skamarock, W. C.: Numerical simulations of the July 10, 1996, Stratospheric-Tropospheric Experiment: Radiation, Aerosols, and Ozone (STERAO)-Deep Convection experiment storm: Redistribution of soluble tracers, J Geophys Res-Atmos, 106, 12381-12400, Doi 10.1029/2001jd900139, 2001.

Baumgartner, M., Weigel, R., Achatz, U., Harvey, A. H., and Spichtinger, P.: Reappraising the appropriate calculation of a common meteorological quantity: Potential Temperature, Atmos. Chem. Phys. Discuss., 2020, 1-43, 10.5194/acp-2020-361, 2020.

Bergman, J. W., Jensen, E. J., Pfister, L., and Yang, Q.: Seasonal differences of vertical-transport efficiency in the tropical tropopause layer: On the interplay between tropical deep convection, large-scale vertical ascent, and horizontal circulationes, J Geophys Res-Atmos, 117, Artn D05302

10.1029/2011jd016992, 2012.

Bergman, J. W., Fierli, F., Jensen, E. J., Honomichl, S., and Pan, L. L.: Boundary layer sources for the Asian anticyclone: Regional contributions to a vertical conduit, J Geophys Res-Atmos, 118, 2560-2575, 10.1002/jgrd.50142, 2013.

Bianchi, F., Junninen, H., Bigi, A., Sinclair, V. A., Dada, L., Hoyle, C. R., Zha, Q., Yao, L., Ahonen, L. R., Bonasoni, P., Buenrostro Mazon, S., Hutterli, M., Laj, P., Lehtipalo, K., Kangasluoma, J., Kerminen, V. M., Kontkanen, J., Marinoni, A., Mirme, S., Molteni, U., Petäjä, T., Riva, M., Rose, C., Sellegri, K., Yan, C., Worsnop, D. R., Kulmala, M., Baltensperger, U., and Dommen, J.: Biogenic particles formed in the Himalaya as an important source of free tropospheric aerosols, Nat Geosci, 14, 4-9, 10.1038/s41561-020-00661-5, 2021.

Borrmann, S., Kunkel, D., Weigel, R., Minikin, A., Deshler, T., Wilson, J. C., Curtius, J., Volk, C. M., Homan, C. D., Ulanovsky, A., Ravegnani, F., Viciani, S., Shur, G. N., Belyaev, G. V., Law, K. S., and Cairo, F.: Aerosols in the tropical and subtropical UT/LS: in-situ measurements of submicron particle abundance and volatility, Atmos Chem Phys, 10, 5573-5592, 10.5194/acp-10-5573-2010, 2010.

Brock, C. A., Hamill, P., Wilson, J. C., Jonsson, H. H., and Chan, K. R.: Particle Formation in the Upper Tropical Troposphere: A Source of Nuclei for the Stratospheric Aerosol, Science, 270, 1650-1653, 10.2307/2887916, 1995.

Brock, C. A., Schröder, F., Kärcher, B., Petzold, A., Busen, R., and Fiebig, M.: Ultrafine particle size distributions measured in aircraft exhaust plumes, Journal of Geophysical Research: Atmospheres, 105, 26555-26567, 10.1029/2000jd900360, 2000.

1637 Brunamonti, S., Jorge, T., Oelsner, P., Hanumanthu, S., Singh, B. B., Kumar, K. R., Sonbawne, S.,
1638 Meier, S., Singh, D., Wienhold, F. G., Luo, B. P., Boettcher, M., Poltera, Y., Jauhiainen, H., Kayastha,
1639 R., Karmacharya, J., Dirksen, R., Naja, M., Rex, M., Fadnavis, S., and Peter, T.: Balloon-borne
1640 measurements of temperature, water vapor, ozone and aerosol backscatter on the southern
1641 slopes of the Himalayas during StratoClim 2016-2017, Atmos Chem Phys, 18, 15937-15957,
1642 10.5194/acp-18-15937-2018, 2018.

1643 Bucci, S., Legras, B., Sellitto, P., D'Amato, F., Viciani, S., Montori, A., Chiarugi, A., Ravegnani, F.,
1644 Ulanovsky, A., Cairo, F., and Stroh, F.: Deep convective influence on the UTLS composition in the
1645 Asian Monsoon Anticyclone region: 2017 StratoClim campaign results, Atmos. Chem. Phys.
1646 Discuss., 2020, 1-29, 10.5194/acp-2019-1053, 2020.

1647 Campbell, P., and Deshler, T.: Condensation nuclei measurements in the midlatitude (1982–
1648 2012) and Antarctic (1986–2010) stratosphere between 20 and 35 km, Journal of Geophysical
1649 Research: Atmospheres, 119, 2013JD019710, 10.1002/2013jd019710, 2014.

1650 Chirkov, M., Stiller, G. P., Laeng, A., Kellmann, S., von Clarmann, T., Boone, C. D., Elkins, J. W.,
1651 Engel, A., Glatthor, N., Grabowski, U., Harth, C. M., Kiefer, M., Kolonjari, F., Krummel, P. B., Linden,
1652 A., Lunder, C. R., Miller, B. R., Montzka, S. A., Muhle, J., O'Doherty, S., Orphal, J., Prinn, R. G., Toon,
1653 G., Vollmer, M. K., Walker, K. A., Weiss, R. F., Wiegele, A., and Young, D.: Global HCFC-22
1654 measurements with MIPAS: retrieval, validation, global distribution and its evolution over 2005-
1655 2012, Atmos Chem Phys, 16, 3345-3368, 10.5194/acp-16-3345-2016, 2016.

1656 Chun, H.-Y., and Kim, Y.-H.: Secondary waves generated by breaking of convective gravity waves
1657 in the mesosphere and their influence in the wave momentum flux, Journal of Geophysical
1658 Research: Atmospheres, 113, 10.1029/2008jd009792, 2008.

1659 Crumeyrolle, S., Manninen, H. E., Sellegri, K., Roberts, G., Gomes, L., Kulmala, M., Weigel, R., Laj, P.,
1660 and Schwarzenboeck, A.: New particle formation events measured on board the ATR-42 aircraft
1661 during the EUCAARI campaign, Atmos. Chem. Phys., 10, 6721-6735, 10.5194/acp-10-6721-2010,
1662 2010.

1663 Crutzen, P. J., and Lawrence, M. G.: The impact of precipitation scavenging on the transport of
1664 trace gases: A 3-dimensional model sensitivity study, J Atmos Chem, 37, 81-112, Doi
1665 10.1023/A:1006322926426, 2000.

1666 Curtius, J., Weigel, R., Vossing, H. J., Wernli, H., Werner, A., Volk, C. M., Konopka, P., Krebsbach, M.,
1667 Schiller, C., Roiger, A., Schlager, H., Dreiling, V., and Borrmann, S.: Observations of meteoric
1668 material and implications for aerosol nucleation in the winter Arctic lower stratosphere derived
1669 from in situ particle measurements, Atmos Chem Phys, 5, 3053-3069, DOI 10.5194/acp-5-3053-
1670 2005, 2005.

1671 de Reus, M., Borrmann, S., Bansemer, A., Heymsfield, A. J., Weigel, R., Schiller, C., Mitev, V., Frey,
1672 W., Kunkel, D., Kurten, A., Curtius, J., Sitnikov, N. M., Ulanovsky, A., and Ravegnani, F.: Evidence
1673 for ice particles in the tropical stratosphere from in-situ measurements, Atmos Chem Phys, 9,
1674 6775-6792, DOI 10.5194/acp-9-6775-2009, 2009.

1675 Dee, D. P., Uppala, S. M., Simmons, A. J., Berrisford, P., Poli, P., Kobayashi, S., Andrae, U.,
1676 Balmaseda, M. A., Balsamo, G., Bauer, P., Bechtold, P., Beljaars, A. C. M., van de Berg, L., Bidlot, J.,
1677 Bormann, N., Delsol, C., Dragani, R., Fuentes, M., Geer, A. J., Haimberger, L., Healy, S. B., Hersbach,
1678 H., Hólm, E. V., Isaksen, L., Kållberg, P., Köhler, M., Matricardi, M., McNally, A. P., Monge-Sanz, B.
1679 M., Morcrette, J. J., Park, B. K., Peubey, C., de Rosnay, P., Tavolato, C., Thépaut, J. N., and Vitart, F.:
1680 The ERA-Interim reanalysis: configuration and performance of the data assimilation system, Q J
1681 Roy Meteor Soc, 137, 553-597, 10.1002/qj.828, 2011.

Dunne, E. M., Gordon, H., Kürten, A., Almeida, J., Duplissy, J., Williamson, C., Ortega, I. K., Pringle, K. J., Adamov, A., Baltensperger, U., Barmet, P., Benduhn, F., Bianchi, F., Breitenlechner, M., Clarke, A., Curtius, J., Dommen, J., Donahue, N. M., Ehrhart, S., Flagan, R. C., Franchin, A., Guida, R., Hakala, J., Hansel, A., Heinritzi, M., Jokinen, T., Kangasluoma, J., Kirkby, J., Kulmala, M., Kupc, A., Lawler, M. J., Lehtipalo, K., Makhmutov, V., Mann, G., Mathot, S., Merikanto, J., Miettinen, P., Nenes, A., Onnela, A., Rap, A., Reddington, C. L. S., Riccobono, F., Richards, N. A. D., Rissanen, M. P., Rondo, L., Sarnela, N., Schobesberger, S., Sengupta, K., Simon, M., Sipilä, M., Smith, J. N., Stozkhov, Y., Tomé, A., Tröstl, J., Wagner, P. E., Wimmer, D., Winkler, P. M., Worsnop, D. R., and Carslaw, K. S.: Global atmospheric particle formation from CERN CLOUD measurements, Science, 354, 1119-1124, 10.1126/science.aaf2649, 2016.

Ekman, A. M. L., Wang, C., Strom, J., and Krejci, R.: Explicit simulation of aerosol physics in a cloud-resolving model: Aerosol transport and processing in the free troposphere, Journal of the Atmospheric Sciences, 63, 682-696, Doi 10.1175/Jas3645.1, 2006.

Ern, M., and Preusse, P.: Gravity wave momentum flux spectra observed from satellite in the summertime subtropics: Implications for global modeling, Geophys Res Lett, 39, 10.1029/2012gl052659, 2012.

Frey, W., Borrmann, S., Kunkel, D., Weigel, R., de Reus, M., Schlager, H., Roiger, A., Voigt, C., Hoor, P., Curtius, J., Kramer, M., Schiller, C., Volk, C. M., Homan, C. D., Fierli, F., Di Donfrancesco, G., Ulanovsky, A., Ravegnani, F., Sitnikov, N. M., Viciani, S., D'Amato, F., Shur, G. N., Belyaev, G. V., Law, K. S., and Cairo, F.: In situ measurements of tropical cloud properties in the West African Monsoon: upper tropospheric ice clouds, Mesoscale Convective System outflow, and subvisual cirrus, Atmos Chem Phys, 11, 5569-5590, DOI 10.5194/acp-11-5569-2011, 2011.

Froyd, K. D., Murphy, D. M., Lawson, P., Baumgardner, D., and Herman, R. L.: Aerosols that form subvisible cirrus at the tropical tropopause, Atmos Chem Phys, 10, 209-218, DOI 10.5194/acp-10-209-2010, 2010.

Fujiwara, M., Sakai, T., Nagai, T., Shiraishi, K., Inai, Y., Khaykin, S., Xi, H. S., Shibata, T., Shiotani, M., and Pan, L. L.: Lower-stratospheric aerosol measurements in eastward-shedding vortices over Japan from the Asian summer monsoon anticyclone during the summer of 2018, Atmos Chem Phys, 21, 3073-3090, 10.5194/acp-21-3073-2021, 2021.

Garny, H., and Randel, W. J.: Transport pathways from the Asian monsoon anticyclone to the stratosphere, Atmos. Chem. Phys., 16, 2703-2718, 10.5194/acp-16-2703-2016, 2016.

Glatthor, N., Hopfner, M., Baker, I. T., Berry, J., Campbell, J. E., Kawa, S. R., Krysztofiak, G., Leyser, A., Sinnhuber, B. M., Stiller, G. P., Stinecipher, J., and von Clarmann, T.: Tropical sources and sinks of carbonyl sulfide observed from space, Geophys Res Lett, 42, 10082-10090, 10.1002/2015gl066293, 2015.

Hanumanthu, S., Vogel, B., Müller, R., Brunamonti, S., Fadnavis, S., Li, D., Ölsner, P., Naja, M., Singh, B. B., Kumar, K. R., Sonbawne, S., Jauhiainen, H., Vömel, H., Luo, B., Jorge, T., Wienhold, F. G., Dirkson, R., and Peter, T.: Strong variability of the Asian Tropopause Aerosol Layer (ATAL) in August 2016 at the Himalayan foothills, Atmos. Chem. Phys. Discuss., 2020, 1-42, 10.5194/acp-2020-552, 2020.

He, Q., Ma, J., Zheng, X., Yan, X., Vömel, H., Wienhold, F. G., Gao, W., Liu, D., Shi, G., and Cheng, T.: Observational evidence of particle hygroscopic growth in the upper troposphere–lower stratosphere (UTLS) over the Tibetan Plateau, Atmos. Chem. Phys., 19, 8399-8406, 10.5194/acp-19-8399-2019, 2019.

Hermann, M., Heintzenberg, J., Wiedensohler, A., Zahn, A., Heinrich, G., and Brenninkmeijer, C. A. M.: Meridional distributions of aerosol particle number concentrations in the upper troposphere and lower stratosphere obtained by Civil Aircraft for Regular Investigation of the Atmosphere Based on an Instrument Container (CARIBIC) flights, J Geophys Res-Atmos, 108, Artn 4114 10.1029/2001jd001077, 2003.

Hersbach, H., and Dee, D. P.: ERA5 reanalysis is in production, ECMWF Newsletter, 147, 7, 2016.

Hoffmann, L., Günther, G., Li, D., Stein, O., Wu, X., Griessbach, S., Heng, Y., Konopka, P., Müller, R., Vogel, B., and Wright, J. S.: From ERA-Interim to ERA5: the considerable impact of ECMWF's next-generation reanalysis on Lagrangian transport simulations, Atmos Chem Phys, 19, 3097-3124, 10.5194/acp-19-3097-2019, 2019.

Höpfner, M., Ungermann, J., Borrmann, S., Wagner, R., Spang, R., Riese, M., Stiller, G., Appel, O., Batenburg, A. M., Bucci, S., Cairo, F., Dragoneas, A., Friedl-Vallon, F., Hünig, A., Johansson, S., Krasauskas, L., Legras, B., Leisner, T., Mahnke, C., Möhler, O., Molleker, S., Müller, R., Neubert, T., Orphal, J., Preusse, P., Rex, M., Saathoff, H., Stroh, F., Weigel, R., and Wohltmann, I.: Ammonium nitrate particles formed in upper troposphere from ground ammonia sources during Asian monsoons, Nat Geosci, 12, 608-612, 10.1038/s41561-019-0385-8, 2019.

Jacobson, M. Z.: Fundamentals of Atmospheric Modeling, Cambridge University Press., New York, 813 pp., 2005.

Jost, A., Szakáll, M., Diehl, K., Mitra, S. K., and Borrmann, S.: Chemistry of riming: the retention of organic and inorganic atmospheric trace constituents, Atmos. Chem. Phys., 17, 9717-9732, 10.5194/acp-17-9717-2017, 2017.

Kerminen, V. M., Petaja, T., Manninen, H. E., Paasonen, P., Nieminen, T., Sipila, M., Junninen, H., Ehn, M., Gagne, S., Laakso, L., Riipinen, I., Vehkamaki, H., Kurten, T., Ortega, I. K., Dal Maso, M., Brus, D., Hyvarinen, A., Lihavainen, H., Leppa, J., Lehtinen, K. E. J., Mirme, A., Mirme, S., Horrak, U., Berndt, T., Stratmann, F., Birmili, W., Wiedensohler, A., Metzger, A., Dommen, J., Baltensperger, U., Kiendler-Scharr, A., Mentel, T. F., Wildt, J., Winkler, P. M., Wagner, P. E., Petzold, A., Minikin, A., Plass-Dulmer, C., Poschl, U., Laaksonen, A., and Kulmala, M.: Atmospheric nucleation: highlights of the EUCAARI project and future directions, Atmos Chem Phys, 10, 10829-10848, 10.5194/acp-10-10829-2010, 2010.

Kerminen, V. M., Chen, X. M., Vakkari, V., Petäjä, T., Kulmala, M., and Bianchi, F.: Atmospheric new particle formation and growth: review of field observations, Environ Res Lett, 13, Artn 103003 10.1088/1748-9326/Aadf3c, 2018.

Kirkby, J., Curtius, J., Almeida, J., Dunne, E., Duplissy, J., Ehrhart, S., Franchin, A., Gagne, S., Ickes, L., Kurten, A., Kupc, A., Metzger, A., Riccobono, F., Rondo, L., Schobesberger, S., Tsagkogeorgas, G., Wimmer, D., Amorim, A., Bianchi, F., Breitenlechner, M., David, A., Dommen, J., Downard, A., Ehn, M., Flagan, R. C., Haider, S., Hansel, A., Hauser, D., Jud, W., Junninen, H., Kreissl, F., Kvashin, A., Laaksonen, A., Lehtipalo, K., Lima, J., Lovejoy, E. R., Makhmutov, V., Mathot, S., Mikkila, J., Minginette, P., Mogo, S., Nieminen, T., Onnela, A., Pereira, P., Petaja, T., Schnitzhofer, R., Seinfeld, J. H., Sipila, M., Stozhkov, Y., Stratmann, F., Tome, A., Vanhanen, J., Viisanen, Y., Vrtala, A., Wagner, P. E., Walther, H., Weingartner, E., Wex, H., Winkler, P. M., Carslaw, K. S., Worsnop, D. R., Baltensperger, U., and Kulmala, M.: Role of sulphuric acid, ammonia and galactic cosmic rays in atmospheric aerosol nucleation, Nature, 476, 429-U477, 10.1038/nature10343, 2011.

Konopka, P., Ploeger, F., and Müller, R.: Entropy- and static stability-based Lagrangian model grids in: Geophysical Monograph Series: Lagrangian Modeling of the Atmosphere, edited by Lin, J., 200, 99-109, https://doi.org/10.1029/2012GM001253, 2012.

1771 Kremser, S., Thomason, L. W., von Hobe, M., Hermann, M., Deshler, T., Timmreck, C., Toohey, M.,
1772 Stenke, A., Schwarz, J. P., Weigel, R., Fueglistaler, S., Prata, F. J., Vernier, J.-P., Schlager, H., Barnes,
1773 J. E., Antuña-Marrero, J.-C., Fairlie, D., Palm, M., Mahieu, E., Notholt, J., Rex, M., Bingen, C.,
1774 Vanhellemont, F., Bourassa, A., Plane, J. M. C., Klocke, D., Carn, S. A., Clarisse, L., Trickl, T., Neely,
1775 R., James, A. D., Rieger, L., Wilson, J. C., and Meland, B.: Stratospheric aerosol - Observations,
1776 processes, and impact on climate, Rev Geophys, 2015RG000511, 10.1002/2015rg000511, 2016.

1777 Kulmala, M., Vehkamaki, H., Petaja, T., Dal Maso, M., Lauri, A., Kerminen, V. M., Birmili, W., and
1778 McMurry, P. H.: Formation and growth rates of ultrafine atmospheric particles: a review of
1779 observations, J Aerosol Sci, 35, 143-176, 10.1016/j.jaerosci.2003.10.003, 2004.

1780 Kulmala, M., Kontkanen, J., Junninen, H., Lehtipalo, K., Manninen, H. E., Nieminen, T., Petaja, T.,
1781 Sipila, M., Schobesberger, S., Rantala, P., Franchin, A., Jokinen, T., Jarvinen, E., Aijala, M.,
1782 Kangasluoma, J., Hakala, J., Aalto, P. P., Paasonen, P., Mikkila, J., Vanhanen, J., Aalto, J., Hakola, H.,
1783 Makkonen, U., Ruuskanen, T., Mauldin, R. L., Duplissy, J., Vehkamaki, H., Back, J., Kortelainen, A.,
1784 Riipinen, I., Kurten, T., Johnston, M. V., Smith, J. N., Ehn, M., Mentel, T. F., Lehtinen, K. E. J.,
1785 Laaksonen, A., Kerminen, V. M., and Worsnop, D. R.: Direct Observations of Atmospheric Aerosol
1786 Nucleation, Science, 339, 943-946, 10.1126/science.1227385, 2013.

1787 Kürten, A., Bianchi, F., Almeida, J., Kupiainen-Maatta, O., Dunne, E. M., Duplissy, J., Williamson, C.,
1788 Barmet, P., Breitenlechner, M., Dommen, J., Donahue, N. M., Flagan, R. C., Franchin, A., Gordon, H.,
1789 Hakala, J., Hansel, A., Heinritzi, M., Ickes, L., Jokinen, T., Kangasluoma, J., Kim, J., Kirkby, J., Kupc,
1790 A., Lehtipalo, K., Leiminger, M., Makhmutov, V., Onnela, A., Ortega, I. K., Petaja, T., Praplan, A. P.,
1791 Riccobono, F., Rissanen, M. P., Rondo, L., Schnitzhofer, R., Schobesberger, S., Smith, J. N., Steiner,
1792 G., Stozhkov, Y., Tome, A., Trostl, J., Tsagkogeorgas, G., Wagner, P. E., Wimmer, D., Ye, P. L.,
1793 Baltensperger, U., Carslaw, K., Kulmala, M., and Curtius, J.: Experimental particle formation rates
1794 spanning tropospheric sulfuric acid and ammonia abundances, ion production rates, and
1795 temperatures, J Geophys Res-Atmos, 121, 12377-12400, 10.1002/2015jd023908, 2016.

1796 Kürten, A., Li, C., Bianchi, F., Curtius, J., Dias, A., Donahue, N. M., Duplissy, J., Flagan, R. C., Hakala,
1797 J., Jokinen, T., Kirkby, J., Kulmala, M., Laaksonen, A., Lehtipalo, K., Makhmutov, V., Onnela, A.,
1798 Rissanen, M. P., Simon, M., Sipilä, M., Stozhkov, Y., Tröstl, J., Ye, P., and McMurry, P. H.: New
1799 particle formation in the sulfuric acid–dimethylamine–water system: reevaluation of CLOUD
1800 chamber measurements and comparison to an aerosol nucleation and growth model, Atmos.
1801 Chem. Phys., 18, 845-863, 10.5194/acp-18-845-2018, 2018.

1802 Kürten, A.: New particle formation from sulfuric acid and ammonia: nucleation and growth
1803 model based on thermodynamics derived from CLOUD measurements for a wide range of
1804 conditions, Atmos. Chem. Phys., 19, 5033-5050, 10.5194/acp-19-5033-2019, 2019.

1805 Kurtén, T., Loukonen, V., Vehkamaki, H., and Kulmala, M.: Amines are likely to enhance neutral
1806 and ion-induced sulfuric acid-water nucleation in the atmosphere more effectively than
1807 ammonia, Atmos Chem Phys, 8, 4095-4103, DOI 10.5194/acp-8-4095-2008, 2008.

1808 Lane, T. P., and Moncrieff, M. W.: Stratospheric Gravity Waves Generated by Multiscale Tropical
1809 Convection, Journal of the Atmospheric Sciences, 65, 2598-2614, 10.1175/2007jas2601.1, 2008.

1810 Lee, K. O., Dauhut, T., Chaboureau, J. P., Khaykin, S., Kramer, M., and Rolf, C.: Convective hydration
1811 in the tropical tropopause layer during the StratoClim aircraft campaign: pathway of an
1812 observed hydration patch, Atmos Chem Phys, 19, 11803-11820, 10.5194/acp-19-11803-2019,
1813 2019.

1814 Lee, S. H., Wilson, J. C., Baumgardner, D., Herman, R. L., Weinstock, E. M., LaFleur, B. G., Kok, G.,
1815 Anderson, B., Lawson, P., Baker, B., Strawa, A., Pittman, J. V., Reeves, J. M., and Bui, T. P.: New

particle formation observed in the tropical/subtropical cirrus clouds, J Geophys Res-Atmos, 109, Artn D20209

10.1029/2004jd005033, 2004.

Li, D., Vogel, B., Muller, R., Bian, J. C., Gunther, G., Ploeger, F., Li, Q., Zhang, J. Q., Bai, Z. X., Vomel, H., and Riese, M.: Dehydration and low ozone in the tropopause layer over the Asian monsoon caused by tropical cyclones: Lagrangian transport calculations using ERA-Interim and ERA5 reanalysis data, Atmos Chem Phys, 20, 4133-4152, 10.5194/acp-20-4133-2020, 2020.

Mahnke, C., Weigel, R., Cairo, F., Vernier, J.-P., Afchine, A., Krämer, M., Mitev, V., Matthey, R., Viciani, S., D'Amato, F., Ploeger, F., Deshler, T., and Borrmann, S.: The ATAL within the 2017 Asian Monsoon Anticyclone: Microphysical aerosol properties derived from aircraft-borne in situ measurements, Atmos. Chem. Phys. Discuss., acp-2020-1241 2021.

McKenna, D. S., Konopka, P., Grooss, J. U., Günther, G., Müller, R., Spang, R., Offermann, D., and Orsolini, Y.: A new Chemical Lagrangian Model of the Stratosphere (CLaMS) - 1. Formulation of advection and mixing, J Geophys Res-Atmos, 107, Artn 4309

10.1029/2000jd000114, 2002.

Merikanto, J., Spracklen, D. V., Mann, G. W., Pickering, S. J., and Carslaw, K. S.: Impact of nucleation on global CCN, Atmos Chem Phys, 9, 8601-8616, 10.5194/acp-9-8601-2009, 2009.

Metzger, A., Verheggen, B., Dommen, J., Duplissy, J., Prevot, A. S. H., Weingartner, E., Riipinen, I., Kulmala, M., Spracklen, D. V., Carslaw, K. S., and Baltensperger, U.: Evidence for the role of organics in aerosol particle formation under atmospheric conditions, P Natl Acad Sci USA, 107, 6646-6651, 10.1073/pnas.0911330107, 2010.

Murphy, D. M., Cziczo, D. J., Froyd, K. D., Hudson, P. K., Matthew, B. M., Middlebrook, A. M., Peltier, R. E., Sullivan, A., Thomson, D. S., and Weber, R. J.: Single-particle mass spectrometry of tropospheric aerosol particles, J Geophys Res-Atmos, 111, Artn D23s32

Doi 10.1029/2006jd007340, 2006.

Murphy, D. M., Froyd, K. D., Schwarz, J. P., and Wilson, J. C.: Observations of the chemical composition of stratospheric aerosol particles, Q J Roy Meteor Soc, 140, 1269-1278, 10.1002/qj.2213, 2014.

Nieminen, T., Kerminen, V. M., Petaja, T., Aalto, P. P., Arshinov, M., Asmi, E., Baltensperger, U., Beddows, D. C. S., Beukes, J. P., Collins, D., Ding, A. J., Harrison, R. M., Henzing, B., Hooda, R., Hu, M., Horrak, U., Kivekas, N., Komsaare, K., Krejci, R., Kristensson, A., Laakso, L., Laaksonen, A., Leaitch, W. R., Lihavainen, H., Mihalopoulos, N., Nemeth, Z., Nie, W., O'Dowd, C., Salma, I., Sellegri, K., Svenningsson, B., Swietlicki, E., Tunved, P., Ulevicius, V., Vakkari, V., Vana, M., Wiedensohler, A., Wu, Z. J., Virtanen, A., and Kulmala, M.: Global analysis of continental boundary layer new particle formation based on long-term measurements, Atmos Chem Phys, 18, 14737-14756, 10.5194/acp-18-14737-2018, 2018.

Pan, L. L., Honomichl, S. B., Kinnison, D. E., Abalos, M., Randel, W. J., Bergman, J. W., and Bian, J.: Transport of chemical tracers from the boundary layer to stratosphere associated with the dynamics of the Asian summer monsoon, Journal of Geophysical Research: Atmospheres, 121, 14.159-114.174, 10.1002/2016jd025616, 2016.

Park, M., Randel, W. J., Gettelman, A., Massie, S. T., and Jiang, J. H.: Transport above the Asian summer monsoon anticyclone inferred from Aura Microwave Limb Sounder tracers, J Geophys Res-Atmos, 112, Artn D16309

10.1029/2006jd008294, 2007.

Park, M., Randel, W. J., Emmons, L. K., and Livesey, N. J.: Transport pathways of carbon monoxide in the Asian summer monsoon diagnosed from Model of Ozone and Related Tracers (MOZART), J Geophys Res-Atmos, 114, Artn D08303

10.1029/2008jd010621, 2009.

Piani, C., Durran, D., Alexander, M. J., and Holton, J. R.: A Numerical Study of Three-Dimensional Gravity Waves Triggered by Deep Tropical Convection and Their Role in the Dynamics of the QBO, Journal of the Atmospheric Sciences, 57, 3689-3702, 10.1175/1520-0469(2000)057<3689:Ansotd>2.0.Co;2, 2000.

Pisso, I., and Legras, B.: Turbulent vertical diffusivity in the sub-tropical stratosphere, Atmos. Chem. Phys., 8, 697-707, 10.5194/acp-8-697-2008, 2008.

Ploeger, F., Günther, G., Konopka, P., Fueglistaler, S., Müller, R., Hoppe, C., Kunz, A., Spang, R., Grooss, J. U., and Riese, M.: Horizontal water vapor transport in the lower stratosphere from subtropics to high latitudes during boreal summer, J Geophys Res-Atmos, 118, 8111-8127, 10.1002/jgrd.50636, 2013.

Ploeger, F., Gottschling, C., Griessbach, S., Grooss, J. U., Günther, G., Konopka, P., Müller, R., Riese, M., Stroh, F., Tao, M., Ungermann, J., Vogel, B., and von Hobe, M.: A potential vorticity-based determination of the transport barrier in the Asian summer monsoon anticyclone, Atmos Chem Phys, 15, 13145-13159, 10.5194/acp-15-13145-2015, 2015.

Ploeger, F., Konopka, P., Walker, K., and Riese, M.: Quantifying pollution transport from the Asian monsoon anticyclone into the lower stratosphere, Atmos Chem Phys, 17, 7055-7066, 10.5194/acp-17-7055-2017, 2017.

Ploeger, F., Diallo, M., Charlesworth, E., Konopka, P., Legras, B., Laube, J. C., Grooß, J. U., Günther, G., Engel, A., and Riese, M.: The stratospheric Brewer–Dobson circulation inferred from age of air in the ERA5 reanalysis, Atmos. Chem. Phys. Discuss., 2021, 1-27, 10.5194/acp-2020-1253, 2021.

Pommrich, R., Müller, R., Grooss, J. U., Konopka, P., Ploeger, F., Vogel, B., Tao, M., Hoppe, C. M., Günther, G., Spelten, N., Hoffmann, L., Pumphrey, H. C., Viciani, S., D'Amato, F., Volk, C. M., Hoor, P., Schlager, H., and Riese, M.: Tropical troposphere to stratosphere transport of carbon monoxide and long-lived trace species in the Chemical Lagrangian Model of the Stratosphere (CLaMS), Geosci Model Dev, 7, 2895-2916, 10.5194/gmd-7-2895-2014, 2014.

Randel, W. J., and Park, M.: Deep convective influence on the Asian summer monsoon anticyclone and associated tracer variability observed with Atmospheric Infrared Sounder (AIRS), J Geophys Res-Atmos, 111, Artn D12314

10.1029/2005jd006490, 2006.

Riccobono, F., Schobesberger, S., Scott, C. E., Dommen, J., Ortega, I. K., Rondo, L., Almeida, J., Amorim, A., Bianchi, F., Breitenlechner, M., David, A., Downard, A., Dunne, E. M., Duplissy, J., Ehrhart, S., Flagan, R. C., Franchin, A., Hansel, A., Junninen, H., Kajos, M., Keskinen, H., Kupc, A., Kürten, A., Kvashin, A. N., Laaksonen, A., Lehtipalo, K., Makhmutov, V., Mathot, S., Nieminen, T., Onnela, A., Petaja, T., Praplan, A. P., Santos, F. D., Schallhart, S., Seinfeld, J. H., Sipila, M., Spracklen, D. V., Stozhkov, Y., Stratmann, F., Tome, A., Tsagkogeorgas, G., Vaattovaara, P., Viisanen, Y., Vrtala, A., Wagner, P. E., Weingartner, E., Wex, H., Wimmer, D., Carslaw, K. S., Curtius, J., Donahue, N. M., Kirkby, J., Kulmala, M., Worsnop, D. R., and Baltensperger, U.: Oxidation Products of Biogenic Emissions Contribute to Nucleation of Atmospheric Particles, Science, 344, 717-721, 10.1126/science.1243527, 2014.

Rollins, A. W., Thornberry, T. D., Watts, L. A., Yu, P., Rosenlof, K. H., Mills, M., Baumann, E., Giorgetta, F. R., Bui, T. V., Hopfner, M., Walker, K. A., Boone, C., Bernath, P. F., Colarco, P. R., Newman, P. A., Fahey, D. W., and Gao, R. S.: The role of sulfur dioxide in stratospheric aerosol formation evaluated by using in situ measurements in the tropical lower stratosphere, Geophys Res Lett, 44, 4280-4286, 10.1002/2017gl072754, 2017.

Rosen, J. M.: The Boiling Point of Stratospheric Aerosols, J Appl Meteorol, 10, 1044-1046, 10.1175/1520-0450(1971)010<1044:tbposa>2.0.co;2, 1971.

Sahyoun, M., Freney, E., Brito, J., Duplissy, J., Gouhier, M., Colomb, A., Dupuy, R., Bourianne, T., Nowak, J. B., Yan, C., Petäjä, T., Kulmala, M., Schwarzenboeck, A., Planche, C., and Sellegri, K.: Evidence of New Particle Formation Within Etna and Stromboli Volcanic Plumes and Its Parameterization From Airborne In Situ Measurements, Journal of Geophysical Research: Atmospheres, 124, 5650-5668, 10.1029/2018jd028882, 2019.

Santee, M. L., Manney, G. L., Livesey, N. J., Schwartz, M. J., Neu, J. L., and Read, W. G.: A comprehensive overview of the climatological composition of the Asian summermonsoon anticyclone based on 10 years of Aura Microwave Limb Sounder measurements, J Geophys Res-Atmos, 122, 5491-5514, 10.1002/2016jd026408, 2017.

Schneider, J., Weigel, R., Klimach, T., Dragoneas, A., Appel, O., Hünig, A., Molleker, S., Köllner, F., Clemen, H.-C., Eppers, O., Hoppe, P., Hoor, P., Mahnke, C., Krämer, M., Rolf, C., Grooß, J.-U., Zahn, A., Obersteiner, F., Ravegnani, F., Ulanovsky, A., Schlager, H., Scheibe, M., Diskin, G. S., DiGangi, J. P., Nowak, J. B., Zöger, M., and Borrmann, S.: Aircraft-based observation of meteoric material in lower stratospheric aerosol particles between 15 and 68° N, Atmos. Chem. Phys. Discuss., in review, https://doi.org/10.5194/acp-2020-660, 2020.

Sellegri, K., Rose, C., Marinoni, A., Lupi, A., Wiedensohler, A., Andrade, M., Bonasoni, P., and Laj, P.: New Particle Formation: A Review of Ground-Based Observations at Mountain Research Stations, Atmosphere-Basel, 10, Artn 493

10.3390/Atmos10090493, 2019.

Sokolov, L., and Lepuchov, B.: Protocol of interaction between Unit for Connection with Scientific Equipment (UCSE) and on-board scientific equipment of Geophysica aircraft (Second edition), Myasishchev Design Bureau (MDB), 1998.

Song, I.-S., Chun, H.-Y., and Lane, T. P.: Generation Mechanisms of Convectively Forced Internal Gravity Waves and Their Propagation to the Stratosphere, Journal of the Atmospheric Sciences, 60, 1960-1980, 10.1175/1520-0469(2003)060<1960:Gmocfi>2.0.Co;2, 2003.

Stenke, A., Schraner, M., Rozanov, E., Egorova, T., Luo, B., and Peter, T.: The SOCOL version 3.0 chemistry-climate model: description, evaluation, and implications from an advanced transport algorithm, Geosci Model Dev, 6, 1407-1427, 10.5194/gmd-6-1407-2013, 2013.

Stohl, A., Forster, C., Frank, A., Seibert, P., and Wotawa, G.: Technical note: The Lagrangian particle dispersion model FLEXPART version 6.2, Atmos. Chem. Phys., 5, 2461-2474, 10.5194/acp-5-2461-2005, 2005.

Stolzenburg, D., Simon, M., Ranjithkumar, A., Kürten, A., Lehtipalo, K., Gordon, H., Ehrhart, S., Finkenzeller, H., Pichelstorfer, L., Nieminen, T., He, X. C., Brilke, S., Xiao, M., Amorim, A., Baalbaki, R., Baccarini, A., Beck, L., Bräkling, S., Caudillo Murillo, L., Chen, D., Chu, B., Dada, L., Dias, A., Dommen, J., Duplissy, J., El Haddad, I., Fischer, L., Gonzalez Carracedo, L., Heinritzi, M., Kim, C., Koenig, T. K., Kong, W., Lamkaddam, H., Lee, C. P., Leiminger, M., Li, Z., Makhmutov, V., Manninen, H. E., Marie, G., Marten, R., Müller, T., Nie, W., Partoll, E., Petäjä, T., Pfeifer, J., Philippov, M., Rissanen, M. P., Rörup, B., Schobesberger, S., Schuchmann, S., Shen, J., Sipilä, M., Steiner, G.,

Stozhkov, Y., Tauber, C., Tham, Y. J., Tomé, A., Vazquez-Pufleau, M., Wagner, A. C., Wang, M., Wang, Y., Weber, S. K., Wimmer, D., Wlasits, P. J., Wu, Y., Ye, Q., Zauner-Wieczorek, M., Baltensperger, U., Carslaw, K. S., Curtius, J., Donahue, N. M., Flagan, R. C., Hansel, A., Kulmala, M., Lelieveld, J., Volkamer, R., Kirkby, J., and Winkler, P. M.: Enhanced growth rate of atmospheric particles from sulfuric acid, Atmos. Chem. Phys., 20, 7359-7372, 10.5194/acp-20-7359-2020, 2020.

Stroh, F., and the StratoClim group: First detailed airborne and balloon measurements of microphysical, dynamical, and chemical processes in the Asian Summer Monsoon Anticyclone: Overview and First Results of the 2016/2017 StratoClim field campaigns., in preparation for submission to Atmos. Chem. Phys., 2021.

Tang, M. J., Cox, R. A., and Kalberer, M.: Compilation and evaluation of gas phase diffusion coefficients of reactive trace gases in the atmosphere: volume 1. Inorganic compounds, Atmos. Chem. Phys., 14, 9233-9247, 10.5194/acp-14-9233-2014, 2014.

Thomason, L., and Peter, T.: SPARC assessment of stratospheric aerosol properties, WCRP-124, WMO/TD-No. 1295, SPARC Report, 2006.

Thomason, L. W., and Vernier, J. P.: Improved SAGE II cloud/aerosol categorization and observations of the Asian tropopause aerosol layer: 1989-2005, Atmos Chem Phys, 13, 4605-4616, 10.5194/acp-13-4605-2013, 2013.

Tissier, A. S., and Legras, B.: Convective sources of trajectories traversing the tropical tropopause layer, Atmos. Chem. Phys., 16, 3383-3398, 10.5194/acp-16-3383-2016, 2016.

Tzella, A., and Legras, B.: A Lagrangian view of convective sources for transport of air across the Tropical Tropopause Layer: distribution, times and the radiative influence of clouds, Atmos. Chem. Phys., 11, 12517-12534, 10.5194/acp-11-12517-2011, 2011.

Venzac, H., Sellegri, K., Laj, P., Villani, P., Bonasoni, P., Marinoni, A., Cristofanelli, P., Calzolari, F., Fuzzi, S., Decesari, S., Facchini, M. C., Vuillermoz, E., and Verza, G. P.: High frequency new particle formation in the Himalayas, P Natl Acad Sci USA, 105, 15666-15671, 10.1073/pnas.0801355105, 2008.

Vernier, J.-P., Fairlie, T. D., Deshler, T., Ratnam, M. V., Gadhavi, H., Kumar, B. S., Natarajan, M., Pandit, A. K., Raj, S. T. A., Kumar, A. H., Jayaraman, A., Singh, A. K., Rastogi, N., Sinha, P. R., Kumar, S., Tiwari, S., Wegner, T., Baker, N., Vignelles, D., Stenchikov, G., Shevchenko, I., Smith, J., Bedka, K., Kesarkar, A., Singh, V., Bhate, J., Ravikiran, V., Rao, M. D., Ravindrababu, S., Patel, A., Vernier, H., Wienhold, F. G., Liu, H., Knepp, T. N., Thomason, L., Crawford, J., Ziemba, L., Moore, J., Crumeyrolle, S., Williamson, M., Berthet, G., Jégou, F., and Renard, J.-B.: BATAL: The Balloon Measurement Campaigns of the Asian Tropopause Aerosol Layer, B Am Meteorol Soc, 99, 955-973, 10.1175/bams-d-17-0014.1, 2018.

Vernier, J. P., Thomason, L. W., and Kar, J.: CALIPSO detection of an Asian tropopause aerosol layer, Geophys Res Lett, 38, Artn L07804

10.1029/2010gl046614, 2011a.

Vernier, J. P., Thomason, L. W., Pommereau, J. P., Bourassa, A., Pelon, J., Garnier, A., Hauchecorne, A., Blanot, L., Trepte, C., Degenstein, D., and Vargas, F.: Major influence of tropical volcanic eruptions on the stratospheric aerosol layer during the last decade, Geophys Res Lett, 38, Artn L12807

1992 Doi 10.1029/2011gl047563, 2011b.

1993 Vernier, J. P., Fairlie, T. D., Natarajan, M., Wienhold, F. G., Bian, J., Martinsson, B. G., Crumeyrolle,
1994 S., Thomason, L. W., and Bedka, K. M.: Increase in upper tropospheric and lower stratospheric
1995 aerosol levels and its potential connection with Asian pollution, J Geophys Res-Atmos, 120,
1996 1608-1619, 10.1002/2014jd022372, 2015.

1997 Viciani, S., D'Amato, F., Mazzinghi, P., Castagnoli, F., Toci, G., and Werle, P.: A cryogenically
1998 operated laser diode spectrometer for airborne measurement of stratospheric trace gases,
1999 Applied Physics B, 90, 581-592, 10.1007/s00340-007-2885-2, 2008.

2000 Viciani, S., Montori, A., Chiarugi, A., and D'Amato, F.: A Portable Quantum Cascade Laser
2001 Spectrometer for Atmospheric Measurements of Carbon Monoxide, Sensors, 18, 2380,
2002 doi:10.3390/s18072380, 2018.

2003 Vincent, R. A., and Alexander, M. J.: Gravity waves in the tropical lower stratosphere: An
2004 observational study of seasonal and interannual variability, Journal of Geophysical Research:
2005 Atmospheres, 105, 17971-17982, 10.1029/2000jd900196, 2000.

2006 Vogel, B., Günther, G., Müller, R., Grooss, J. U., Hoor, P., Krämer, M., Müller, S., Zahn, A., and Riese,
2007 M.: Fast transport from Southeast Asia boundary layer sources to northern Europe: rapid uplift
2008 in typhoons and eastward eddy shedding of the Asian monsoon anticyclone, Atmos Chem Phys,
2009 14, 12745-12762, 10.5194/acp-14-12745-2014, 2014.

2010 Vogel, B., Müller, R., Günther, G., Spang, R., Hanumanthu, S., Li, D., Riese, M., and Stiller, G. P.:
2011 Lagrangian simulations of the transport of young air masses to the top of the Asian monsoon
2012 anticyclone and into the tropical pipe, Atmos Chem Phys, 19, 6007-6034, 10.5194/acp-19-6007-
2013 2019, 2019.

2014 von der Weiden, S. L., Drewnick, F., and Borrmann, S.: Particle Loss Calculator - a new software
2015 tool for the assessment of the performance of aerosol inlet systems, Atmos Meas Tech, 2, 479-
2016 494, DOI 10.5194/amt-2-479-2009, 2009.

2017 von Hobe, M., Ploeger, F., Konopka, P., Kloss, C., Ulanowski, A., Yushkov, V., Ravegnani, F., Volk, C.
2018 M., Pan, L. L., Honomichl, S. B., Tilmes, S., Kinnison, D. E., Garcia, R. R., and Wright, J. S.: Upward
2019 transport into and within the Asian monsoon anticyclone as inferred from StratoClim trace gas
2020 observations, Atmos. Chem. Phys. Discuss., 2020, 1-31, 10.5194/acp-2020-891, 2020.

2021 Wang, M., Kong, W., Marten, R., He, X.-C., Chen, D., Pfeifer, J., Heitto, A., Kontkanen, J., Dada, L.,
2022 Kürten, A., Yli-Juuti, T., Manninen, H. E., Amanatidis, S., Amorim, A., Baalbaki, R., Baccarini, A.,
2023 Bell, D. M., Bertozzi, B., Bräkling, S., Brilke, S., Murillo, L. C., Chiu, R., Chu, B., De Menezes, L.-P.,
2024 Duplissy, J., Finkenzeller, H., Carracedo, L. G., Granzin, M., Guida, R., Hansel, A., Hofbauer, V.,
2025 Krechmer, J., Lehtipalo, K., Lamkaddam, H., Lampimäki, M., Lee, C. P., Makhmutov, V., Marie, G.,
2026 Mathot, S., Mauldin, R. L., Mentler, B., Müller, T., Onnela, A., Partoll, E., Petäjä, T., Philippov, M.,
2027 Pospisilova, V., Ranjithkumar, A., Rissanen, M., Rörup, B., Scholz, W., Shen, J., Simon, M., Sipilä, M.,
2028 Steiner, G., Stolzenburg, D., Tham, Y. J., Tomé, A., Wagner, A. C., Wang, D. S., Wang, Y., Weber, S. K.,
2029 Winkler, P. M., Wlasits, P. J., Wu, Y., Xiao, M., Ye, Q., Zauner-Wieczorek, M., Zhou, X., Volkamer, R.,
2030 Riipinen, I., Dommen, J., Curtius, J., Baltensperger, U., Kulmala, M., Worsnop, D. R., Kirkby, J.,
2031 Seinfeld, J. H., El-Haddad, I., Flagan, R. C., and Donahue, N. M.: Rapid growth of new atmospheric
2032 particles by nitric acid and ammonia condensation, Nature, 581, 184-189, 10.1038/s41586-020-
2033 2270-4, 2020.

2034 Wehner, B., Werner, F., Ditas, F., Shaw, R. A., Kulmala, M., and Siebert, H.: Observations of new
2035 particle formation in enhanced UV irradiance zones near cumulus clouds, Atmos Chem Phys, 15,
2036 11701-11711, 10.5194/acp-15-11701-2015, 2015.

Weigel, R., Hermann, M., Curtius, J., Voigt, C., Walter, S., Bottger, T., Lepukhov, B., Belyaev, G., and Borrmann, S.: Experimental characterization of the COndensation PArticle counting System for high altitude aircraft-borne application, Atmos Meas Tech, 2, 243-258, 10.5194/amt-2-243-2009, 2009.

Weigel, R., Borrmann, S., Kazil, J., Minikin, A., Stohl, A., Wilson, J. C., Reeves, J. M., Kunkel, D., de Reus, M., Frey, W., Lovejoy, E. R., Volk, C. M., Viciani, S., D'Amato, F., Schiller, C., Peter, T., Schlager, H., Cairo, F., Law, K. S., Shur, G. N., Belyaev, G. V., and Curtius, J.: In situ observations of new particle formation in the tropical upper troposphere: the role of clouds and the nucleation mechanism, Atmos Chem Phys, 11, 9983-10010, 10.5194/acp-11-9983-2011, 2011.

Weigel, R., Volk, C. M., Kandler, K., Hosen, E., Gunther, G., Vogel, B., Grooss, J. U., Khaykin, S., Belyaev, G. V., and Borrmann, S.: Enhancements of the refractory submicron aerosol fraction in the Arctic polar vortex: feature or exception?, Atmos Chem Phys, 14, 12319-12342, DOI 10.5194/acp-14-12319-2014, 2014.

Weigel, R., Mahnke, C., Baumgartner, M., Krämer, M., Spichtinger, P., Spelten, N., Afchine, A., Rolf, C., Viciani, S., D'Amato, F., Tost , H., Belyaev, G. V., and Borrmann, S.: In-Situ observation of New Particle Formation (NPF) in the tropical tropopause layer of the 2017 Asian Monsoon Anticyclone: Part II - NPF inside ice clouds, Atmos. Chem. Phys. Discuss., acp-2020-1285, 2021b.

Weigelt, A., Hermann, M., van Velthoven, P. F. J., Brenninkmeijer, C. A. M., Schlaf, G., Zahn, A., and Wiedensohler, A.: Influence of clouds on aerosol particle number concentrations in the upper troposphere, J Geophys Res-Atmos, 114, Artn D01204

10.1029/2008jd009805, 2009.

Williamson, C., Kupc, A., Wilson, J., Gesler, D. W., Reeves, J. M., Erdesz, F., McLaughlin, R., and Brock, C. A.: Fast time response measurements of particle size distributions in the 3-60 nm size range with the nucleation mode aerosol size spectrometer, Atmos Meas Tech, 11, 3491-3509, 10.5194/amt-11-3491-2018, 2018.

Williamson, C. J., Kupc, A., Axisa, D., Bilsback, K. R., Bui, T., Campuzano-Jost, P., Dollner, M., Froyd, K. D., Hodshire, A. L., Jimenez, J. L., Kodros, J. K., Luo, G., Murphy, D. M., Nault, B. A., Ray, E. A., Weinzierl, B., Wilson, J. C., Yu, F., Yu, P., Pierce, J. R., and Brock, C. A.: A large source of cloud condensation nuclei from new particle formation in the tropics, Nature, 574, 399-403, 10.1038/s41586-019-1638-9, 2019.

WMO: Meteorology -- A three-dimensional science, WMO Bull, 134--138, 1957.

WMO: International Meteorological Tables, WMO-No.188.TP97, edited by: Letestu, S., Secretariat of the World Meteorological Organization, Geneva, Switzerland, 1966.

Wright, C. J., and Gille, J. C.: HIRDLS observations of gravity wave momentum fluxes over the monsoon regions, Journal of Geophysical Research: Atmospheres, 116, 10.1029/2011jd015725, 2011.

Yu, F. Q., Luo, G., Bates, T. S., Anderson, B., Clarke, A., Kapustin, V., Yantosca, R. M., Wang, Y. X., and Wu, S. L.: Spatial distributions of particle number concentrations in the global troposphere: Simulations, observations, and implications for nucleation mechanisms, J Geophys Res-Atmos, 115, Artn D17205

10.1029/2009jd013473, 2010.

Yu, P., Rosenlof, K. H., Liu, S., Telg, H., Thornberry, T. D., Rollins, A. W., Portmann, R. W., Bai, Z., Ray, E. A., Duan, Y., Pan, L. L., Toon, O. B., Bian, J., and Gao, R.-S.: Efficient transport of

2080 tropospheric aerosol into the stratosphere via the Asian summer monsoon anticyclone,
2081 Proceedings of the National Academy of Sciences, 114, 6972-6977, 10.1073/pnas.1701170114,
2082 2017.

2083 Yu, P. F., Toon, O. B., Neely, R. R., Martinsson, B. G., and Brenninkmeijer, C. A. M.: Composition and
2084 physical properties of the Asian Tropopause Aerosol Layer and the North American
2085 Tropospheric Aerosol Layer, Geophys Res Lett, 42, 2540-2546, 10.1002/2015gl063181, 2015.

2086 Zhang, Y., McMurry, P. H., Yu, F. Q., and Jacobson, M. Z.: A comparative study of nucleation
2087 parameterizations: 1. Examination and evaluation of the formulations, J Geophys Res-Atmos,
2088 115, Artn D20212

2089 10.1029/2010jd014150, 2010.

2090

Figure captions

Figure 1~~Figure 1~~: (a) Flight patterns ~~conducted throughout~~of the StratoClim 2017 mission over Nepal, India, ~~and~~ Bangladesh, and the Bay of Bengal. (b) Regions with elevated number concentrations of nucleation-mode particles (N_{nm}, ambient conditions) of sizes in the diameter range 6 nm < d_p < 15 nm ~~as observed by means of~~from COPAS measurements are indicated by the colour-code and by symbol size along the fight tracks.

Figure 2~~Figure 2~~: Synopsis of vertical profiles of the total number concentration (median with 10th, 25th, 75th, 90th, and 99th percentiles) of sub-micrometre sized particles as a function of potential temperature obtained from condensation nuclei (CN) detections over (a) Brazil (TROCCINOX, 2005), over (b) West Africa (SCOUT-AMMA, 2006) and over (c) the Indian subcontinent (StratoClim 2017). During TROCCINOX (a) and SCOUT-AMMA (b) the number concentrations N_4 at lower heights (θ < 350 K) were measured aboard the DLR Falcon (cf. Borrmann et al. (2010) and Weigel et al. (2011)). All high-altitude measurements (θ > 350 K) from the M-55 *Geophysica* and the entire StratoClim 2017 data set result from COPAS measurements. (c) The median profile of $N_{5.3}$ from repeated measurements (over the years 2004 – 2007) with the NMASS multi-channel CN counter over Central America (aboard the NASA WB-57F, data courtesy of J. C. Wilson, Denver University, 2011). All number concentrations are given at ambient conditions.

Figure 3~~Figure 3~~: (a) 1 Hz-resolved particle mixing ratios n_6 and n_{10} (grey-shaded COPAS data points) with n_6 median profile from StratoClim 2017 together with COPAS data from other tropical regions (over Brazil, TROCCINOX 2005 and over West Africa, SCOUT-AMMA 2006, cf. (Borrmann et al., 2010)). The median profile of measurements in the tropics over the Americas (Brock et al., 1995) is ~~is added~~coloured in green. (b) The vertical distribution of the mixing ratio of nucleation-mode particle ($n_{nm} = n_{6\text{-}15}$) in compliance with the NPF criterion (cf. Section 0~~2.1.3~~). (c) The 1 Hz-resolved mixing ratio of non-volatile particles (i.e. thermostable at ~ 270°C) from COPAS measurements throughout StratoClim 2017 with corresponding median profile, including 25th and 75th percentile. Herein, the n_6 median profile is ~~recalled~~ implied from Panel a for comparison ~~from Panel a~~. (d) The fraction f ($= n_{10}\text{nv}/n_{10} \cdot 100$) of non-volatile particles with median, and with 25th and 75th percentiles. ~~Median data points are connected with lines to guide the reader's eyes.~~

Figure 4~~Figure 4~~: Frequency of the duration of observed NPF events ~~(cf. Section 2.1.3 for definition)~~ during the ~~entire~~ StratoClim 2017 mission. (a) as frequency distribution of the NPF duration, (b) as vertical profile as a function of mean potential temperature and coloured with reference to the mean mixing ratio $\overline{n_{nm}}$ of the nucleation-mode particles.

Figure 5~~Figure 5~~: (a) Diurnal variation of the occurrence frequency of NPF events ~~(cf. Section 2.1.3 for definition)~~. (b) The diurnal distribution of NPF events' mean particle mixing ratio $\overline{n_{nm}}$ with standard deviation σ, coloured by flight date, and (c) in colours of the (logarithmic) duration of respective event. Note, the mean horizontal distance is derived from the event duration based on a mean flight speed of 154 m s^{-1} (σ = ± 39 m s^{-1}, variable flight attitude remains unconsidered) and is understood as equivalent horizontal extension of a NPF event.

Figure 6~~Figure 6~~: Mean particle mixing ratio $\overline{n_{nm}}$ of individual NPF events as function of (left column) the vertical distance from the mean lapse-rate tropopause ($\overline{\Delta\theta}$), and of (right column) the equivalent latitude (90° represents the centre of the AMA as projected to polar coordinates). Data points are coloured by flight date (Panels a and b) and by CO mixing ratios (Panels c and d).

(e) The mean particle mixing ratio $\overline{n_{nm}}$ as function of the equivalent latitude is colour-coded by the values $\overline{\Delta\theta}$ (colour scale on the left of panel (e)).

Figure 7~~Figure 7~~: Results of a coagulation simulation based on the assumption of a distinct and expired burst-like event. The simulation's initial particle size distribution (black circles; horizontal bars indicate the width of each size bin) is merged from data of three COPAS detectors (for N_6, N_{10}, and N_{15}) and of the UHSAS-A (65 nm < d_p < 1 µm) as detected during NPF encountered on 04 August 2017, between 04:04:40 and 04:05:06 UTC. (a): The processing particle size distribution (coloured lines) over several hours. (b): The concentration of nucleation-mode particles (N_{nm}) over the simulation's run time and its fractional contribution to the total particle number concentration (N_{total}). Furthermore, the simulated decay of variably multiplied N_{nm} (by factors 0.1, 10, and 100) as initial input of the simulation under constant background conditions (dashed lines).

Figure 8~~Figure 8~~: Particle mixing ratio of fine-mode particles n_6 (grey dots in the background) and of nucleation-mode particles n_{nm} (colour-coded with reference to the potential temperature) in relationship to the CO mixing ratio. The median n_{nm} with the 25th and 75th percentile is shown in bin widths of 2.5 nmol mol^{-1} of the CO mixing ratio (black dots)~~, which are connected by lines to guide the eyes of the reader.~~

Figure 9~~Figure 9~~: From backward trajectory analyses by means of the chemistry transport model ClaMS and based on ERA-5 data in Panel a) the geographic position of the last boundary layer (BL) contact of the NPF-connected air mass backward trajectories, in Panel b) the geographic position of the maximum ascent rate. Subpanels a.1 and a.2 (b.1 and b.2) provide 2-level zoom-ins of the respective main Panel a) or b) based on the same data set. The backward trajectories were analysed over the last 50 days prior to the NPF detection as starting point of each trajectory. Here, the data points are coloured with reference to the (logarithmic) mixing ratio n_{nm} of nucleation-mode particles, grey data points indicate transport times > 25 days.

Figure 10~~Figure 10~~: ~~A~~structured as in Figure 9~~Figure 9~~, in Panel a) the last boundary layer (BL) contact of the NPF-connected air mass backward trajectories and in Panel b) the maximum ascent rate of these trajectories (for details of ~~from backward~~the trajectory analyses~~ with the chemistry transport model ClaMS based on ERA-5 data over the last 50 days prior to the NPF detection. Subpanels a.1 and a.2 (b.1 and b.2) provide 2-level zoom-ins of the respective main Panel a (b) based on the same data set~~ with ClaMS, cf. Figure 9~~Figure 9~~). Here, t~~T~~he data points are coloured to the air mass transport time since the last BL contact, grey data points indicate transport times > 25 days.

Figure 11~~Figure 11~~: Vertical profile of the 1 Hz-resolved particle mixing ratio of nucleation-mode particles n_{nm} colour-coded by the air mass transport time (days) from the boundary layer (BL). F~~-~~or details of ClaMS analyses, cf. Figure 9~~Figure 9~~ andFigure 10~~Figure 10~~~~By means of the chemistry transport model CLaMS and based on ERA-5 data the backward trajectories were analysed over the last 50 days prior to the NPF detection as starting point of each trajectory, grey data points indicate transport times > 25 days~~.

Figure 12~~Figure 12~~: Vertical profile of the event-wise mean particle mixing ratio of nucleation-mode particles $\overline{n_{nm}}$ with standard deviation σ (bars) as a function of the mean potential temperature (± σ). (a) The data points are colour-coded by the proportion of convective

contribution to the air sample. (b) The data points are coloured by the time (days) since the release of the air mass at the top of a convective cell.

Figure 13~~Figure 13~~: Time series of data sampled during a section of a StratoClim 2017 flight (KTM 6) on 06 August 2017. Except the manoeuvre period between 09:20 and 09:30 (UTC), a ~~strictly~~ constant altitude and pressure level (Panel a) were maintained. Particle mixing ratios n_6, n_{10} and n_{15} and n_{10}nv (Panel b), the mixing ratio of the nucleation-mode particles n_{nm} (Panel c), the CO mixing ratio (Panel d), the ambient air temperature (T_{amb}), and the temperature fluctuation (T_{amb} - T_{mean}) (Panel e) feature different characteristics and sequence during two NPF phases (oblique hatched areas).

Figure 14~~14~~: Close-up view of the two sections of StratoClim 2017 flight (KTM #6) on 06 August 2017 over time ranges of more than 1 hour of flight time, respectively, including the two identified NPF periods (horizontal bar in panels a and b). For analysing the ~~character of~~ observed temperature anomaly, the 1 Hz-resolved temperature data are filtered by the noise-reducing running average over 201 data points (T_{201}). The ~~overlaid~~ wave fit (T_{Fit}) is approximated to the noise-filtered data set within the period of identified NPF (cf. Appendix B for details). The overlaid fit function ~~adequately~~ approximates the characteristic structure of the observed temperature anomaly only within the two NPF periods.

Figure A- 1~~1~~: For the time intervals shown in Figure 14~~14~~: the difference between the 1 Hz-data (T_{1Hz}) and the filtered data with 201-seconds running average (T_{201}) reveals the high-frequency noise of the temperature measurement (red data points). The dashed reference lines indicate the standard deviation (± 1 σ and ± 3 σ) of the noise signal within given time intervals. The effectiveness of the wave fit approximation to the filtered data set during the NPF periods is represented by the difference T_{201}-T_{Fit}. During NPF this deviation is small while away from NPF the wave fit increasingly deviates from the temperature measurement. The deviation of the overlaid wave fit from the untreated 1 Hz signal is shown with the differences T_{1Hz}-T_{Fit}: during NPF mainly the noise signal remains.

Figure A- 2~~2~~: Simulated influence of temperature anomalies (up to ~ 4 K) on the quotient of saturation ratios S/S_0 of pure sulphuric acid (H_2SO_4) in reference to any initial saturation ratio S_0 (including supersaturation), ~~i.e. the factorial increase of the saturation ratio S in reference to an initial saturation ratio S_0 at undisturbed conditions (including supersaturated states),~~ over a range of initial air temperatures at which NPF was observed during StratoClim 2017.

Figures

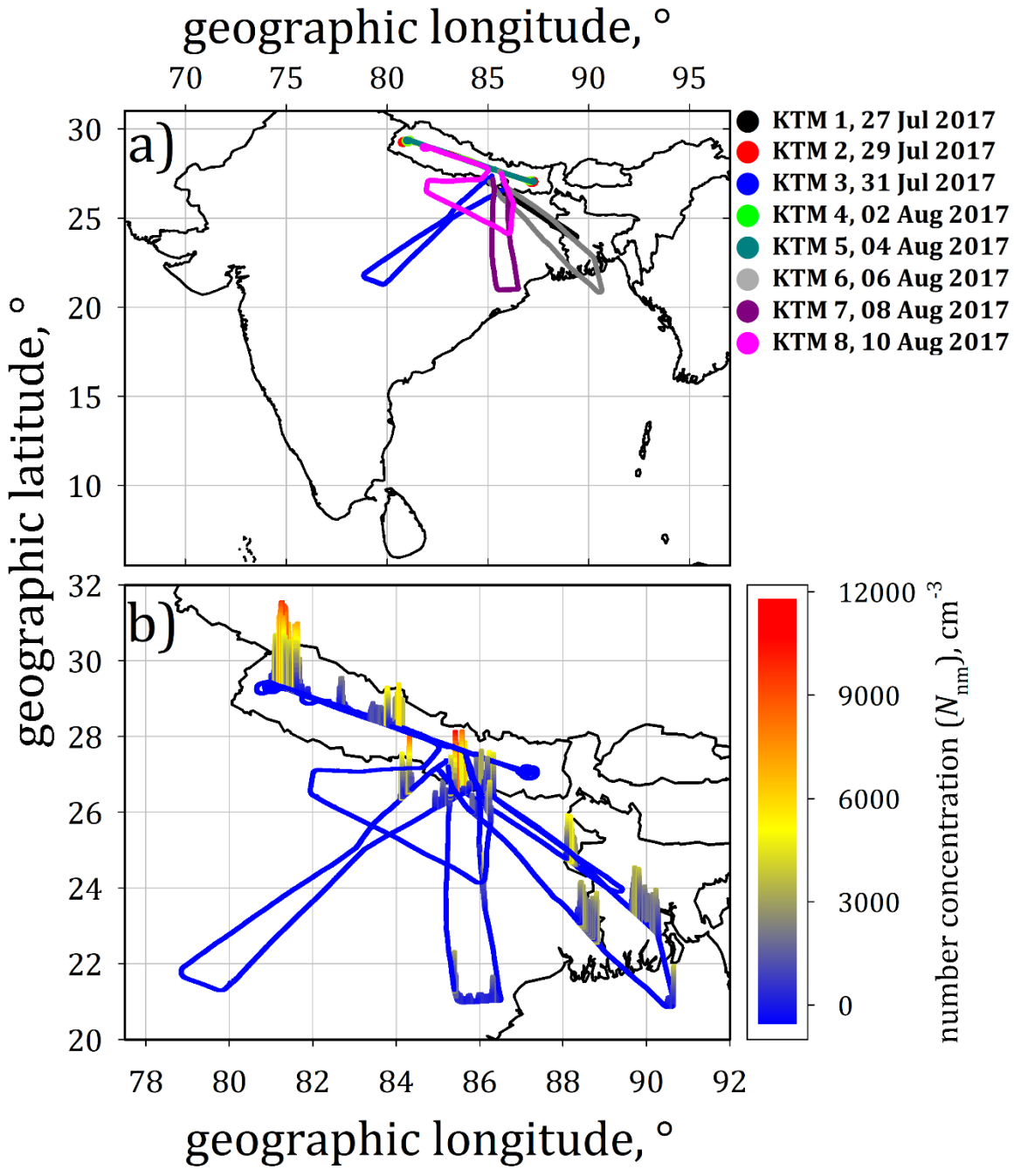

Figure 1

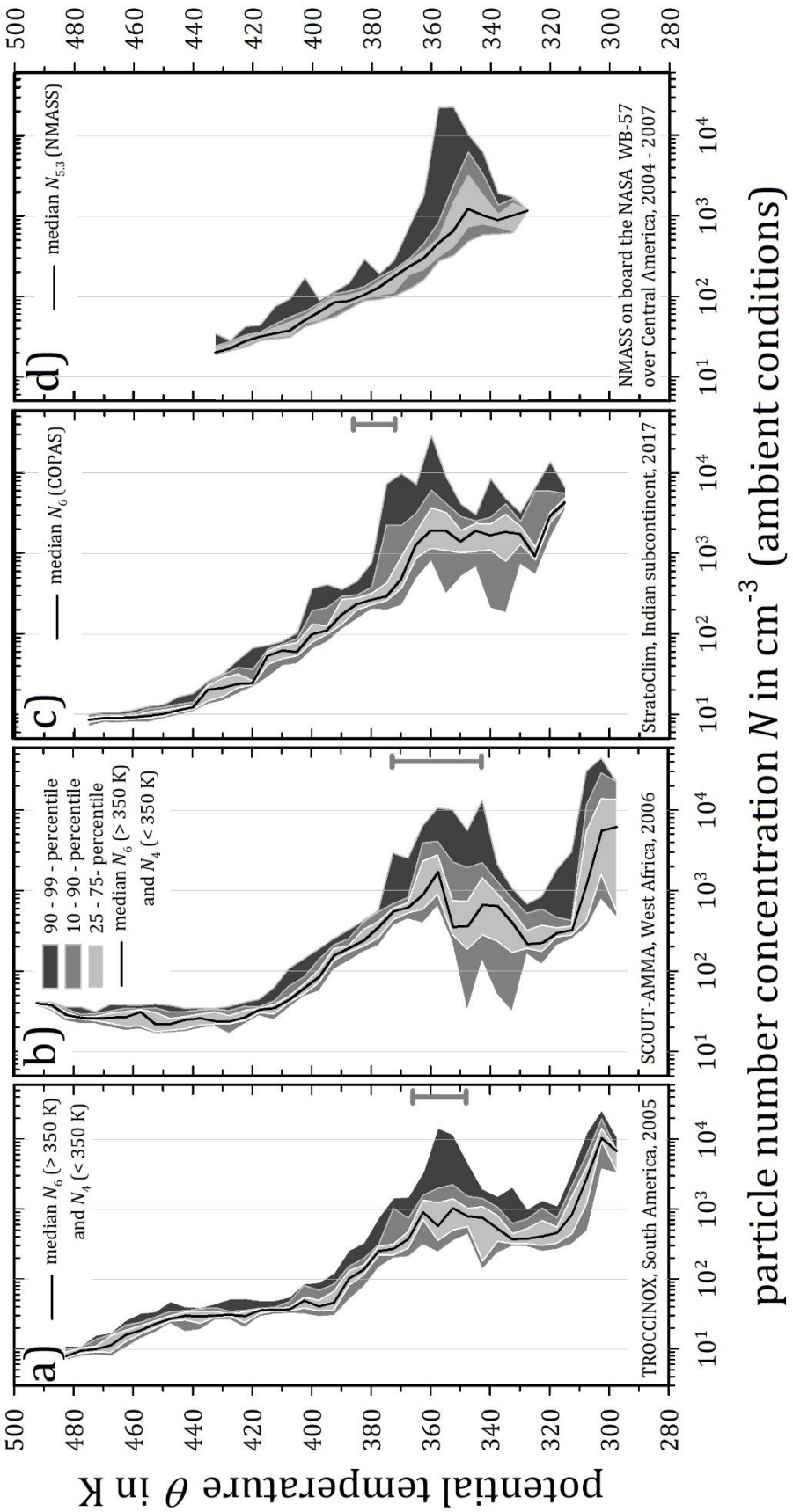
a)
b)
c)
d)
median N_6 (> 350 K) and N_4 (< 350 K)
90 - 99 - percentile
10 - 90 - percentile
25 - 75- percentile
median N_6 (> 350 K) and N_4 (< 350 K)
median N_6 (COPAS)
median $N_{5.3}$ (NMASS)
TROCCINOX, South America, 2005
SCOUT-AMMA, West Africa, 2006
StratoClim, Indian subcontinent, 2017
NMASS on board the NASA WB-57 over Central America, 2004 - 2007
potential temperature θ in K
particle number concentration N in cm^{-3} (ambient conditions)

Figure 2

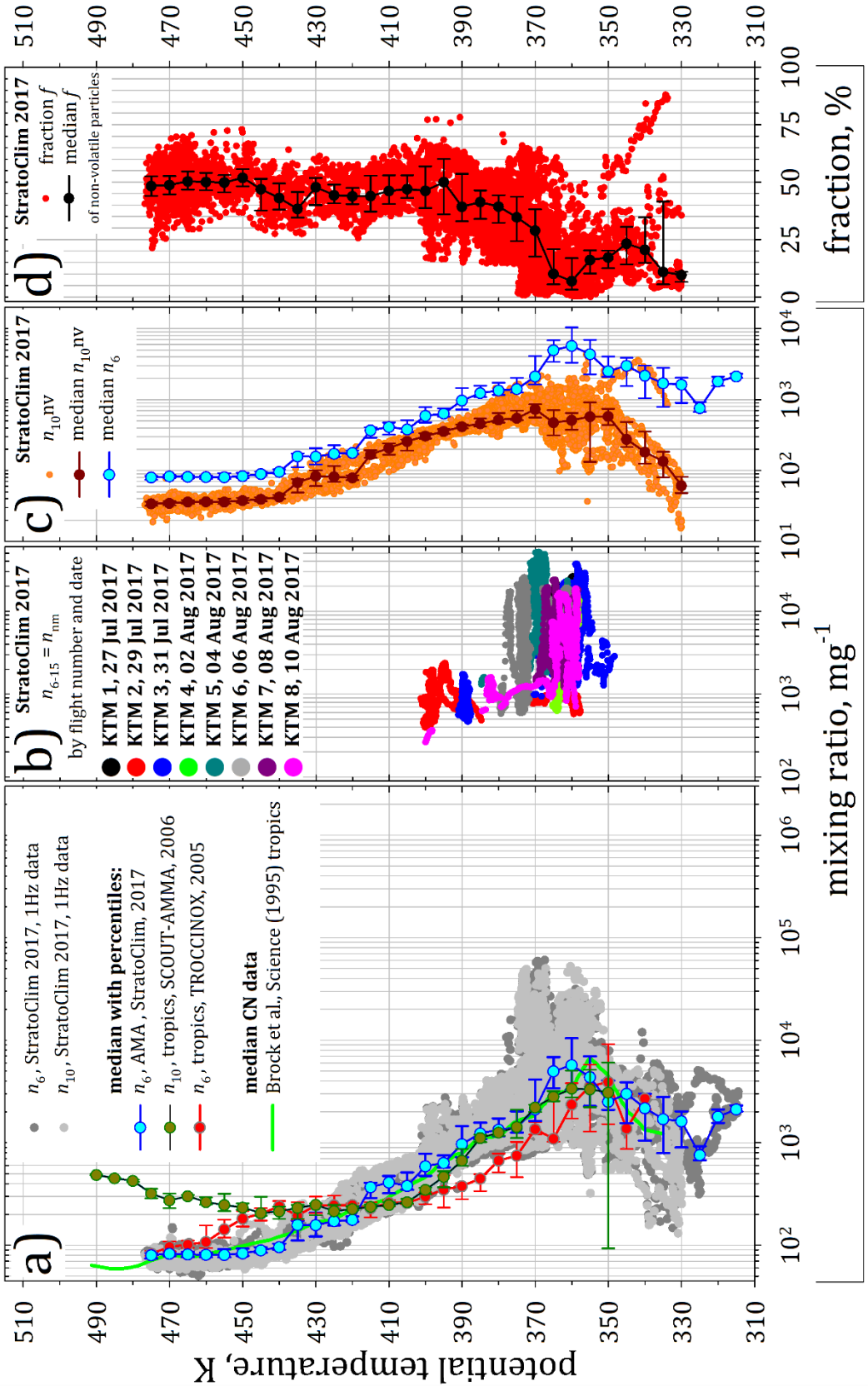
a)
b)
c)
d)
potential temperature, K
mixing ratio, mg^{-1}
fraction, %
n_6, StratoClim 2017, 1Hz data
n_{10}, StratoClim 2017, 1Hz data
median with percentiles:
n_6, AMA , StratoClim, 2017
n_{10}, tropics, SCOUT-AMMA, 2006
n_6, tropics, TROCCINOX, 2005
median CN data
Brock et al., Science (1995) tropics
StratoClim 2017
$n_{6\text{-}15} = n_{nm}$
by flight number and date
KTM 1, 27 Jul 2017
KTM 2, 29 Jul 2017
KTM 3, 31 Jul 2017
KTM 4, 02 Aug 2017
KTM 5, 04 Aug 2017
KTM 6, 06 Aug 2017
KTM 7, 08 Aug 2017
KTM 8, 10 Aug 2017
StratoClim 2017
n_{10}nv
median n_{10}nv
median n_6
StratoClim 2017
fraction f
median f
of non-volatile particles

Figure 3

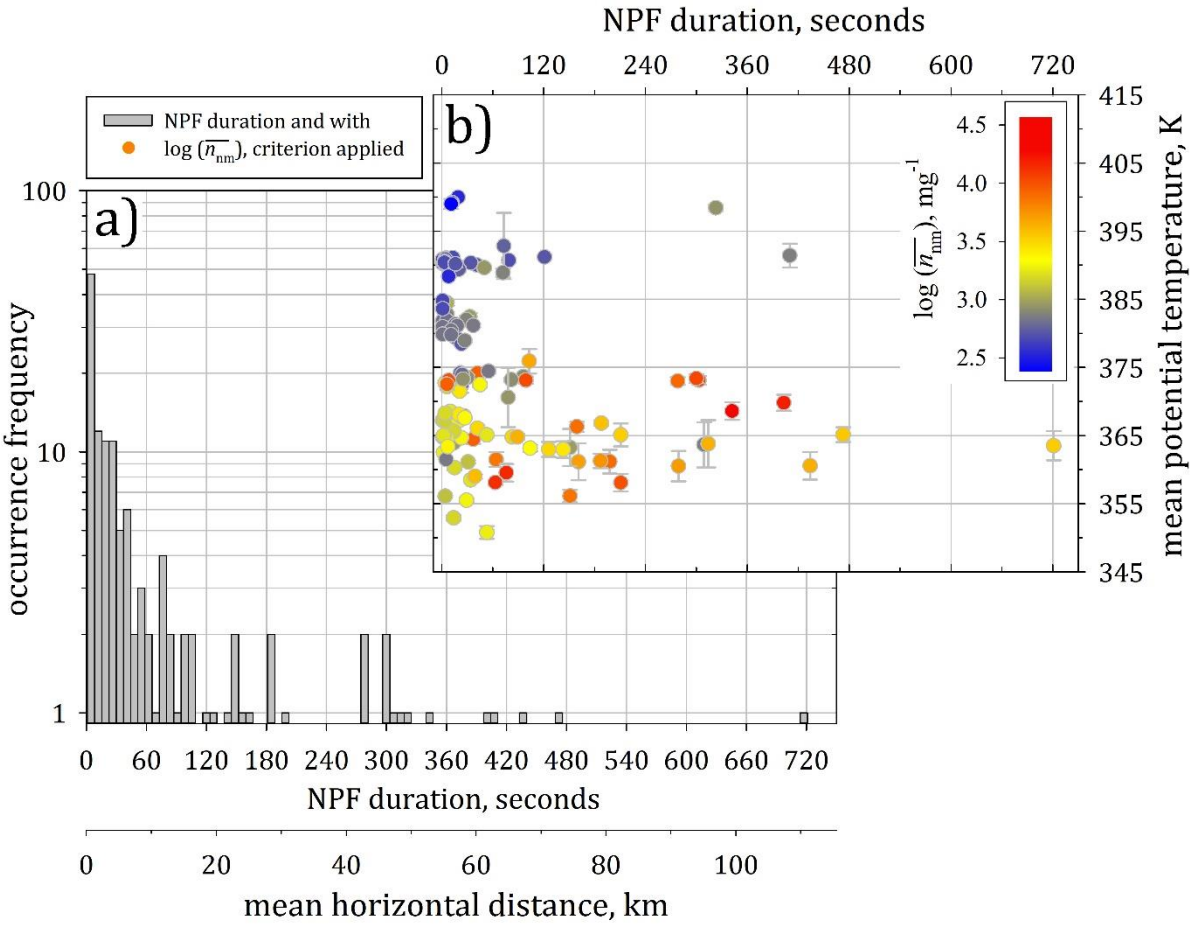
NPF duration, seconds
0
120
240
360
480
600
720
NPF duration and with
log ($\overline{n_{nm}}$), criterion applied
b)
a)
100
10
1
occurrence frequency
0
60
120
180
240
300
360
420
480
540
600
660
720
NPF duration, seconds
0
20
40
60
80
100
mean horizontal distance, km
415
405
395
385
375
365
355
345
mean potential temperature, K
4.5
4.0
3.5
3.0
2.5
log ($\overline{n_{nm}}$), mg^{-1}

Figure 4

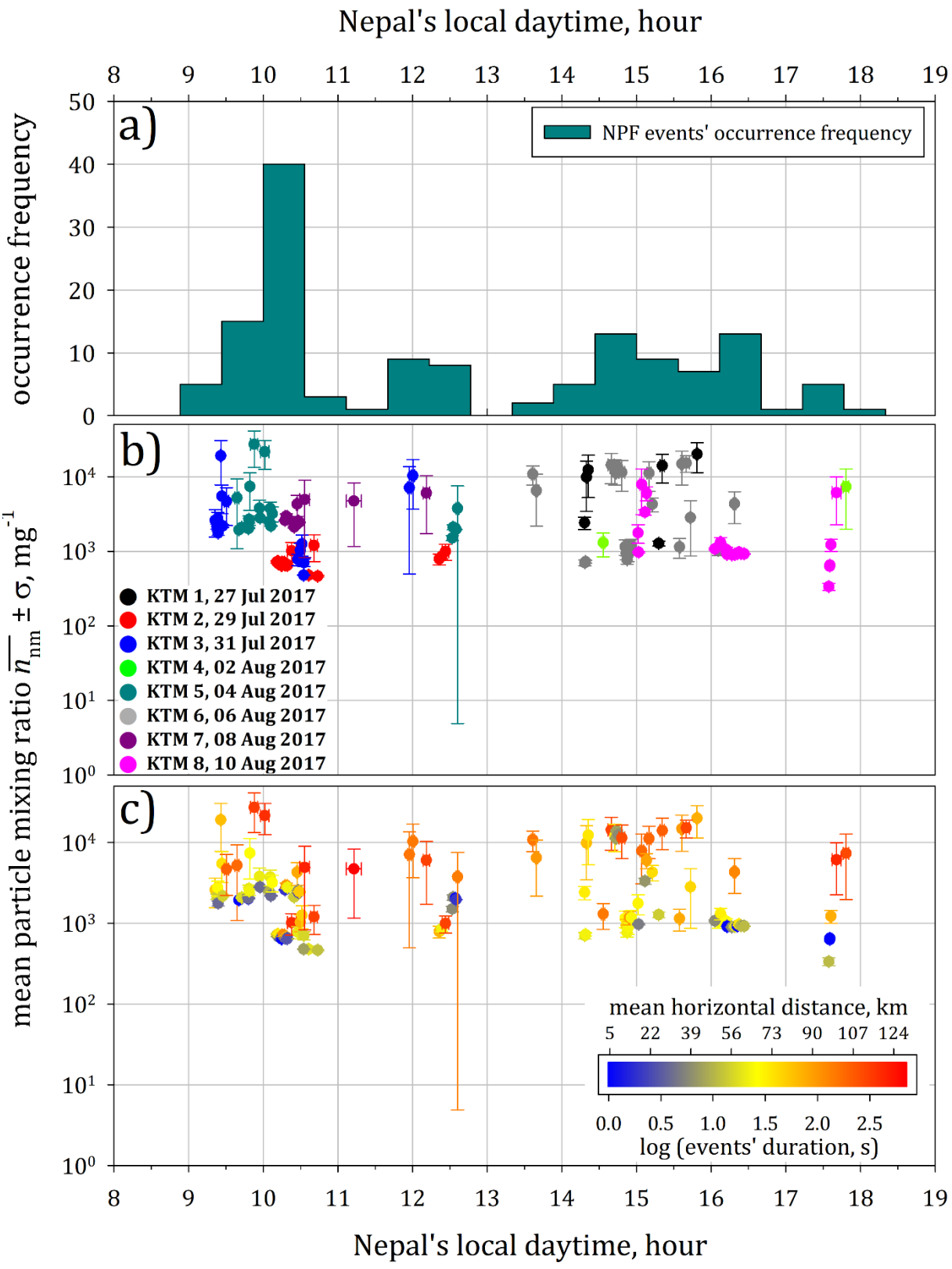
Nepal's local daytime, hour
a)
NPF events' occurrence frequency
occurrence frequency
b)
KTM 1, 27 Jul 2017
KTM 2, 29 Jul 2017
KTM 3, 31 Jul 2017
KTM 4, 02 Aug 2017
KTM 5, 04 Aug 2017
KTM 6, 06 Aug 2017
KTM 7, 08 Aug 2017
KTM 8, 10 Aug 2017
mean particle mixing ratio $\overline{n_{nm}} \pm \sigma$, mg^{-1}
c)
mean horizontal distance, km
5 22 39 56 73 90 107 124
0.0 0.5 1.0 1.5 2.0 2.5
log (events' duration, s)
Nepal's local daytime, hour

Figure 5

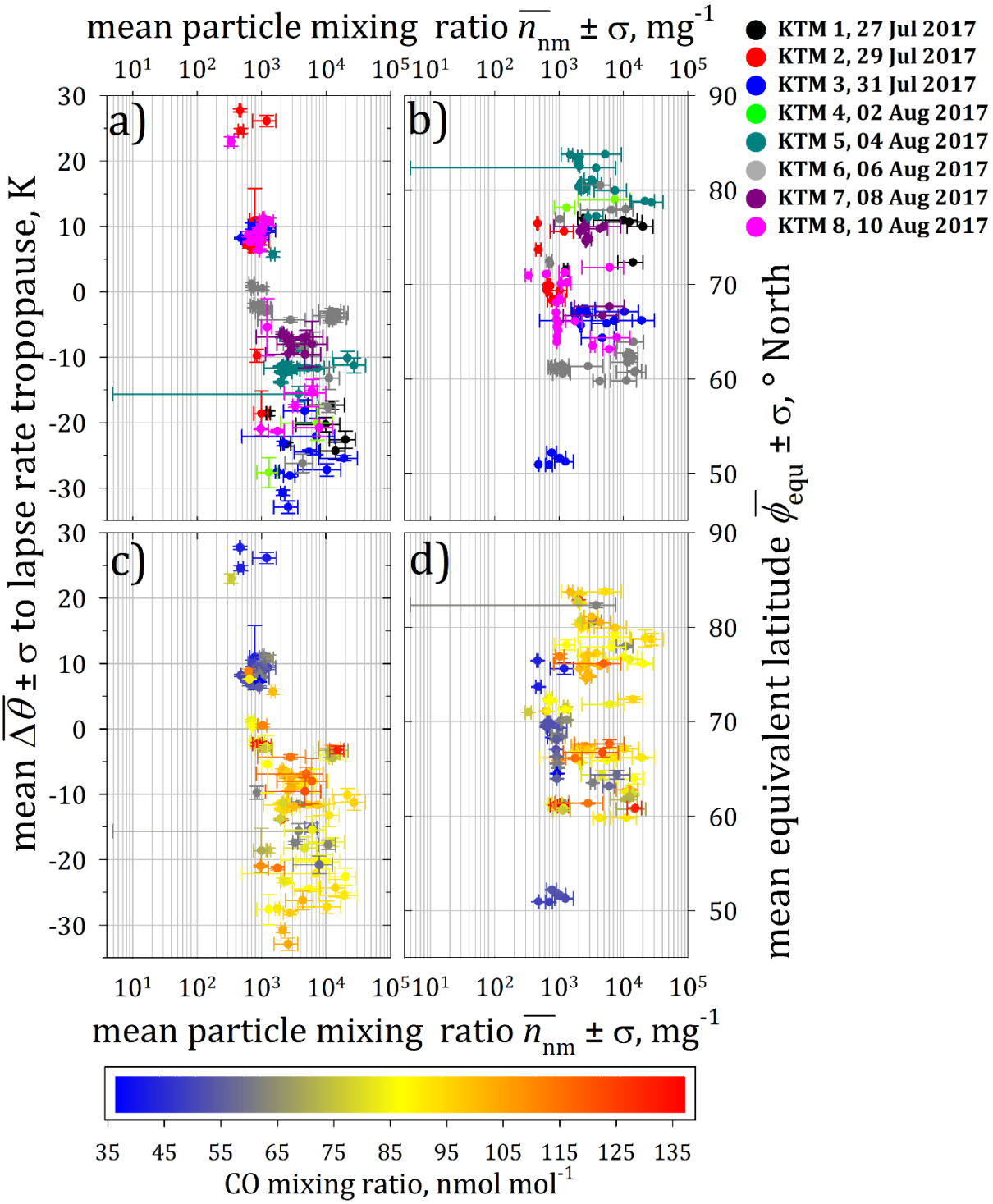
mean particle mixing ratio $\overline{n}_{nm} \pm \sigma$, mg^{-1}
10^1 10^2 10^3 10^4 10^5
a)
b)
c)
d)
30 20 10 0 -10 -20 -30
90 80 70 60 50
mean $\overline{\Delta\theta} \pm \sigma$ to lapse rate tropopause, K
mean equivalent latitude $\overline{\phi}_{equ} \pm \sigma$, ° North
KTM 1, 27 Jul 2017
KTM 2, 29 Jul 2017
KTM 3, 31 Jul 2017
KTM 4, 02 Aug 2017
KTM 5, 04 Aug 2017
KTM 6, 06 Aug 2017
KTM 7, 08 Aug 2017
KTM 8, 10 Aug 2017
35 45 55 65 75 85 95 105 115 125 135
CO mixing ratio, nmol mol^{-1}

Figure 6

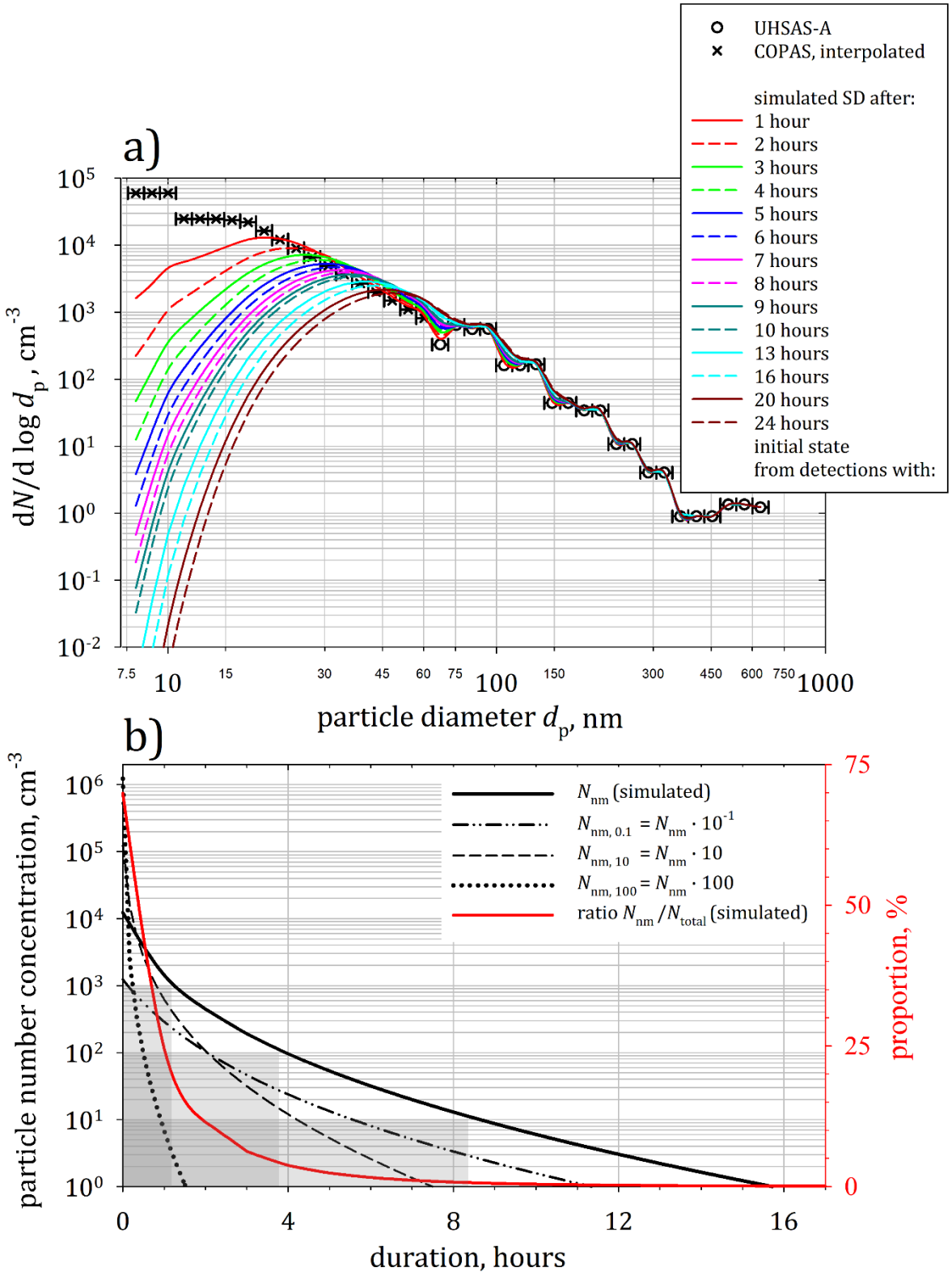
a)
UHSAS-A
COPAS, interpolated
simulated SD after:
1 hour
2 hours
3 hours
4 hours
5 hours
6 hours
7 hours
8 hours
9 hours
10 hours
13 hours
16 hours
20 hours
24 hours
initial state
from detections with:
dN/d log d_p , cm^-3
particle diameter d_p, nm
b)
particle number concentration, cm^-3
proportion, %
N_nm (simulated)
N_nm, 0.1 = N_nm · 10^-1
N_nm, 10 = N_nm · 10
N_nm, 100 = N_nm · 100
ratio N_nm / N_total (simulated)
duration, hours

Figure 7

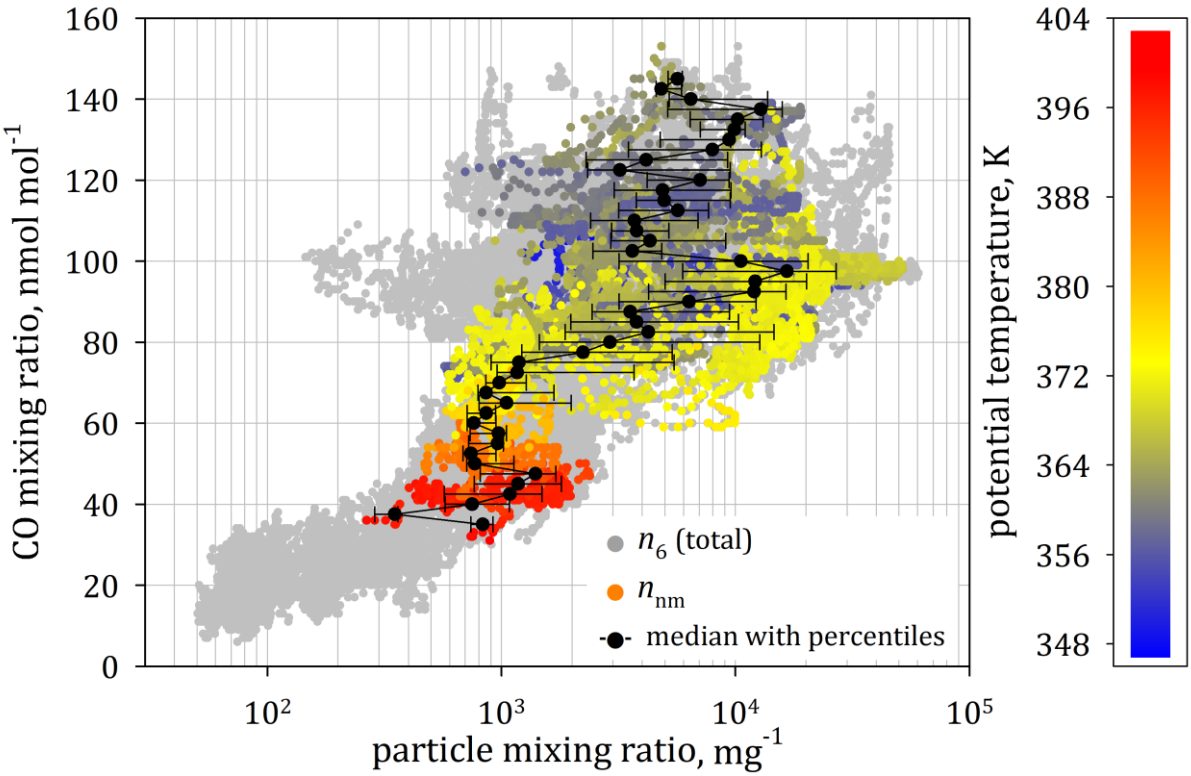
CO mixing ratio, nmol mol-1
160
140
120
100
80
60
40
20
0
10²
10³
10⁴
10⁵
particle mixing ratio, mg-1
n6 (total)
nnm
median with percentiles
potential temperature, K
404
396
388
380
372
364
356
348

Figure 8

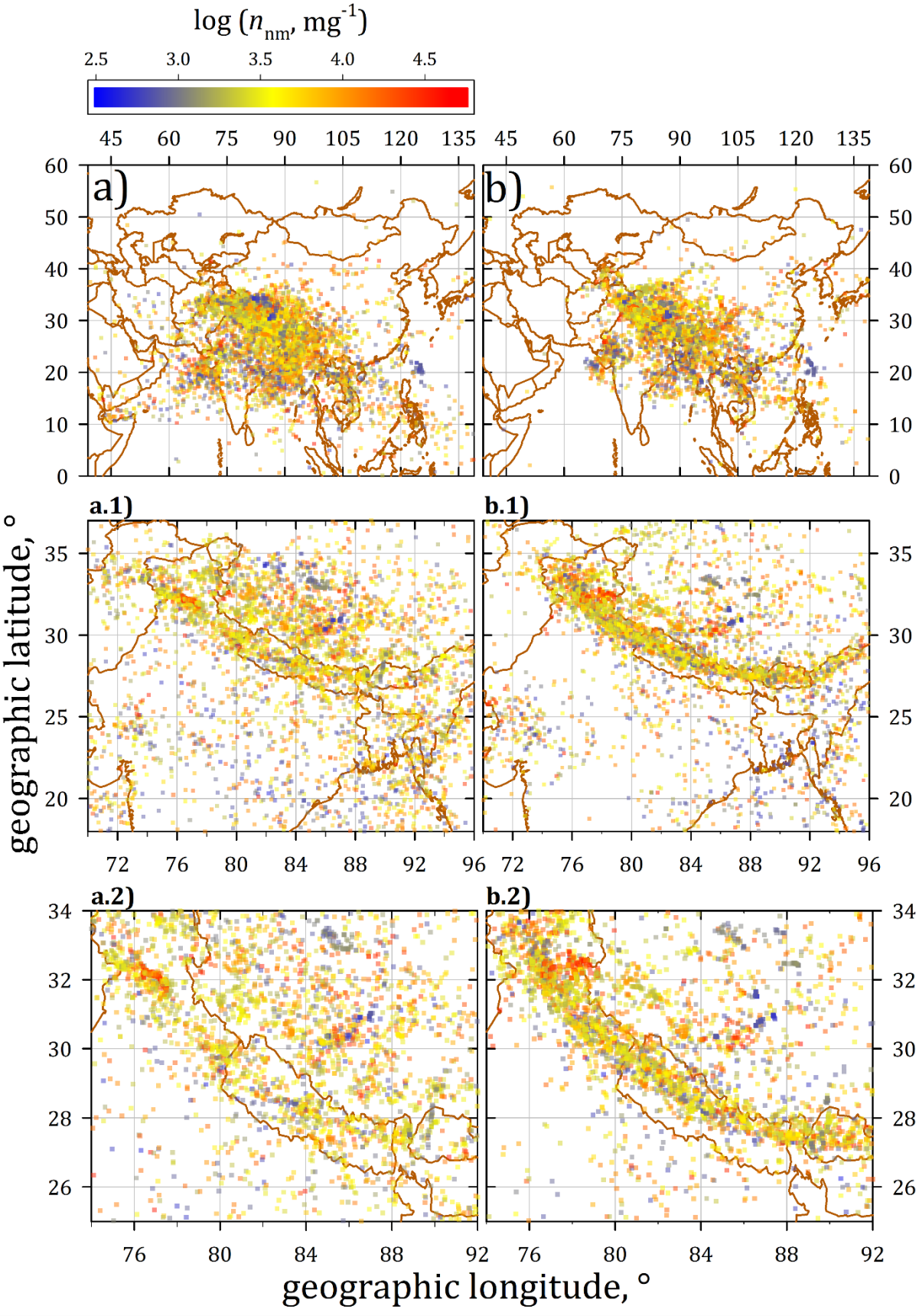
log (n_{nm}, mg^{-1})
2.5
3.0
3.5
4.0
4.5
a)
b)
a.1)
b.1)
a.2)
b.2)
geographic latitude, °
geographic longitude, °

Figure 9

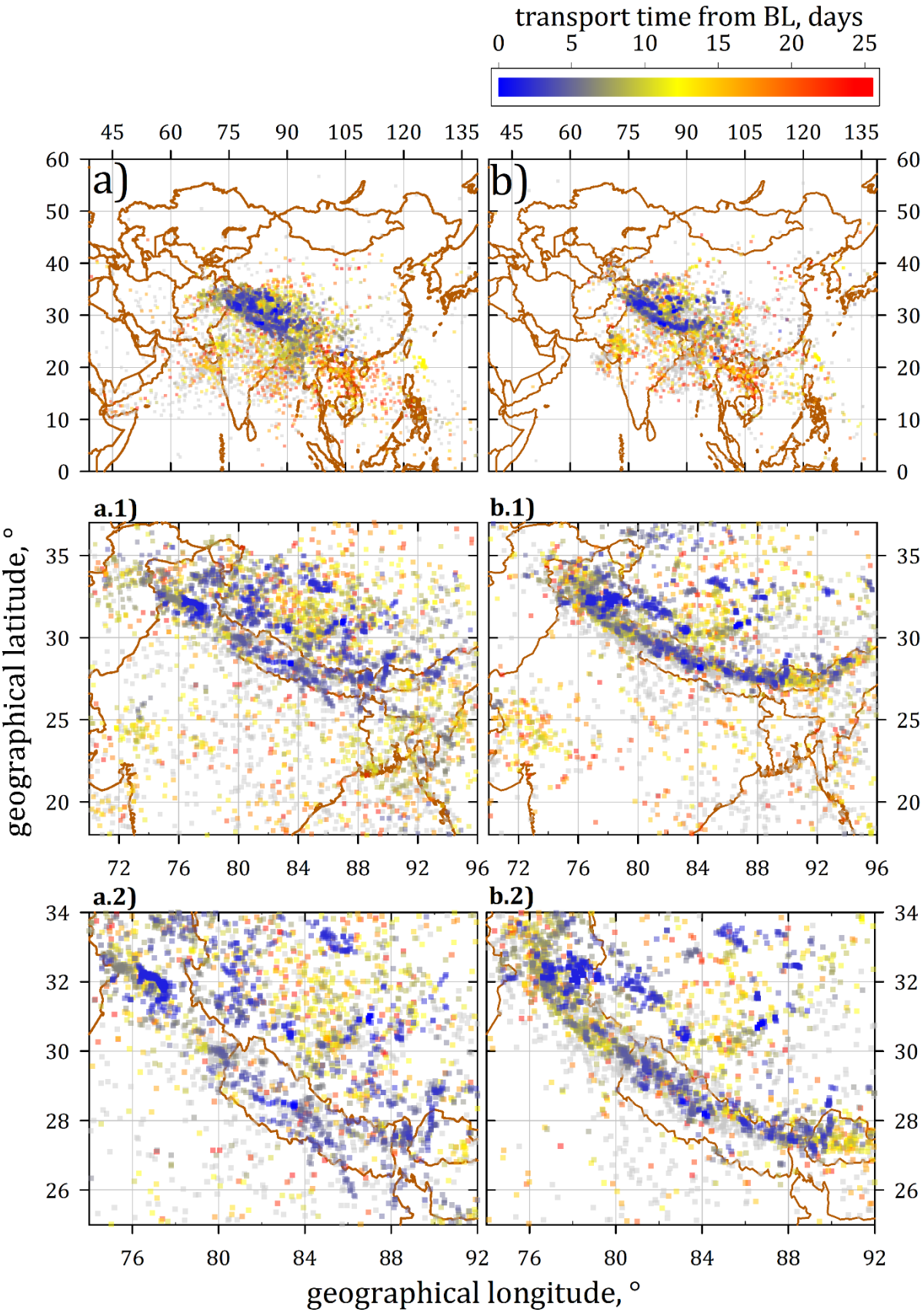
transport time from BL, days
0
5
10
15
20
25
a)
b)
a.1)
b.1)
a.2)
b.2)
geographical latitude, °
geographical longitude, °

Figure 10

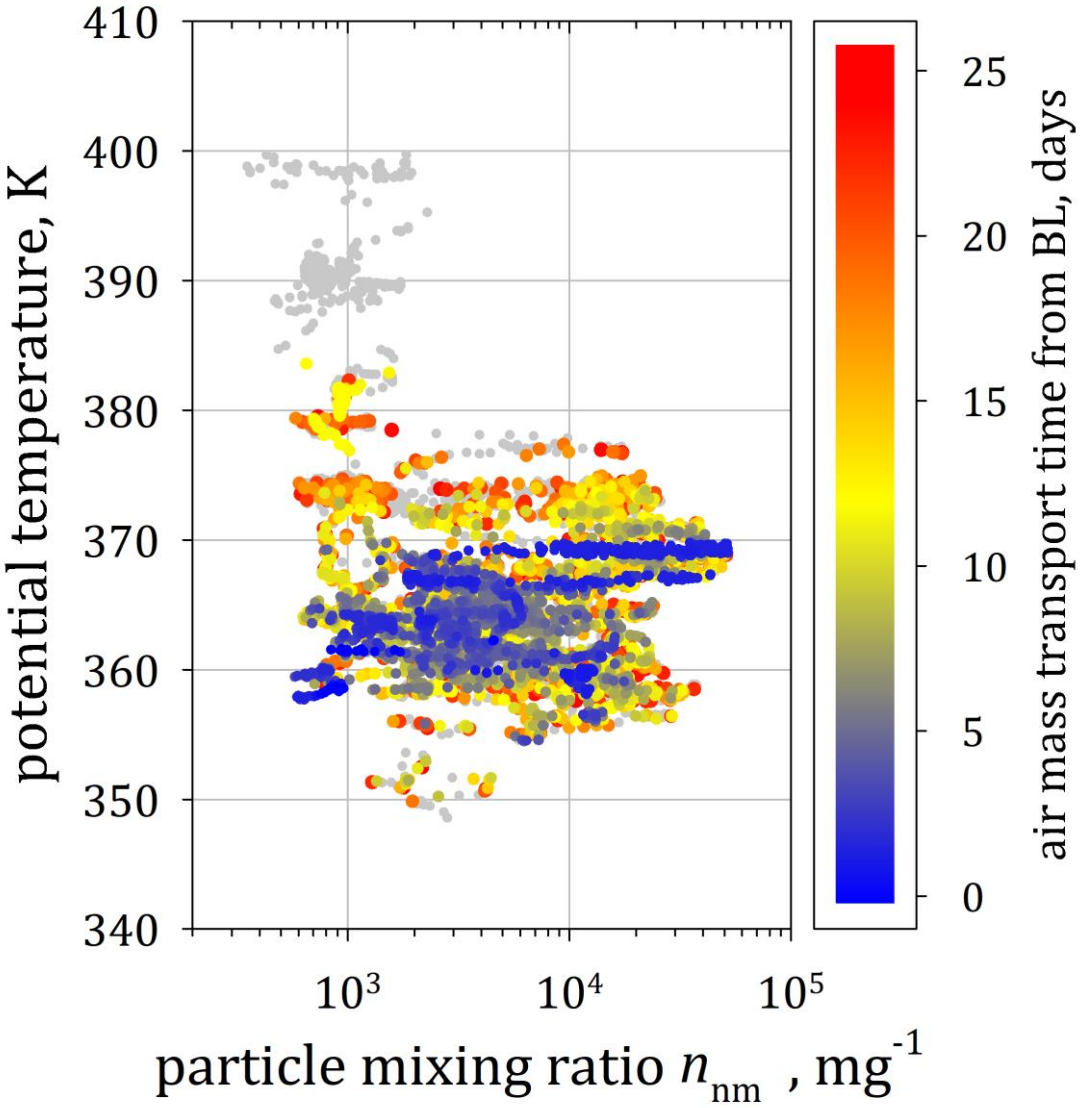
410
400
390
380
370
360
350
340
potential temperature, K
10^3
10^4
10^5
particle mixing ratio n_{nm} , mg^{-1}
25
20
15
10
5
0
air mass transport time from BL, days

Figure 11

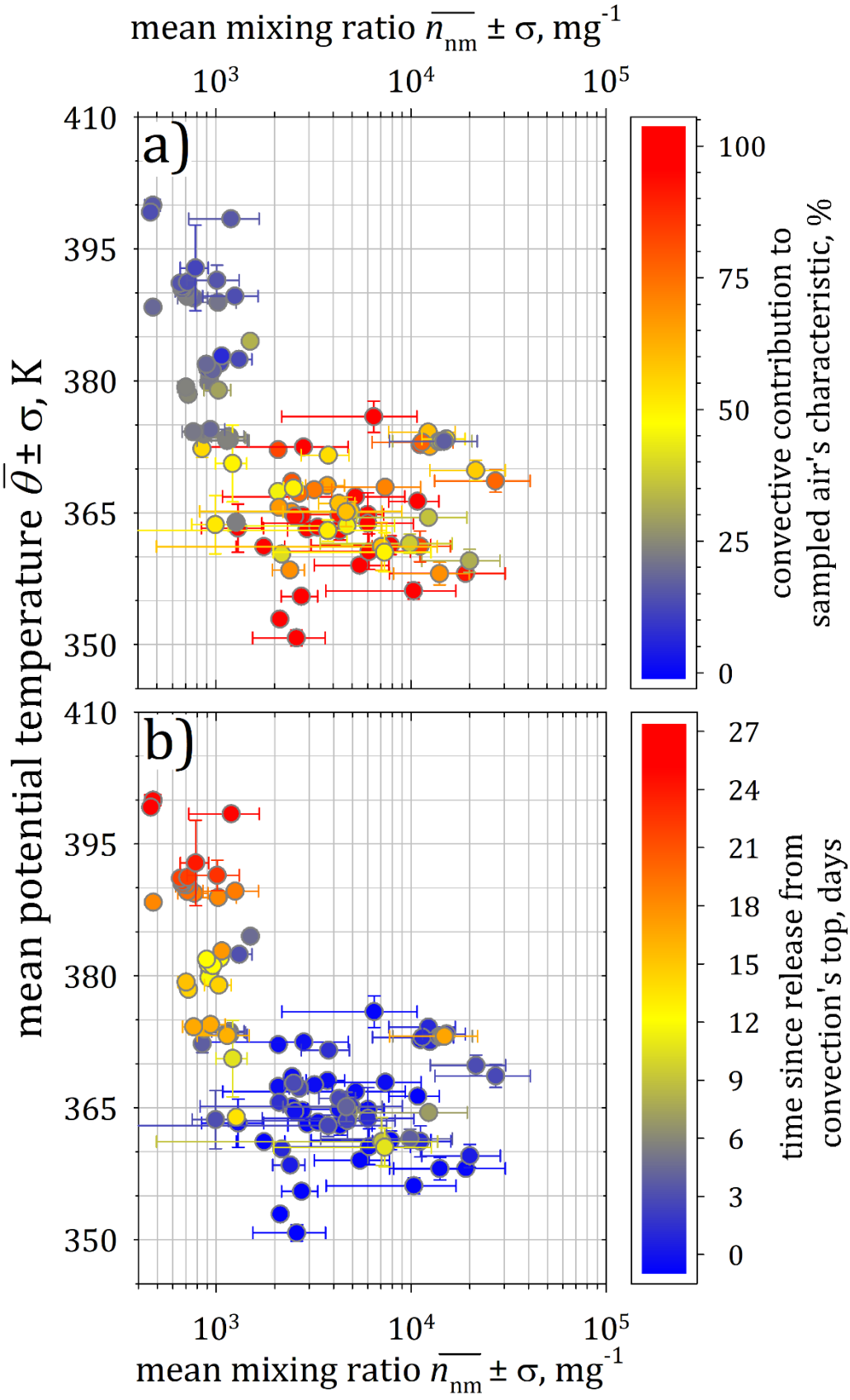
mean mixing ratio $\overline{n_{nm}} \pm \sigma$, mg^{-1}
10^3
10^4
10^5
a)
b)
410
395
380
365
350
mean potential temperature $\overline{\theta} \pm \sigma$, K
100
75
50
25
0
convective contribution to sampled air's characteristic, %
27
24
21
18
15
12
9
6
3
0
time since release from convection's top, days

Figure 12

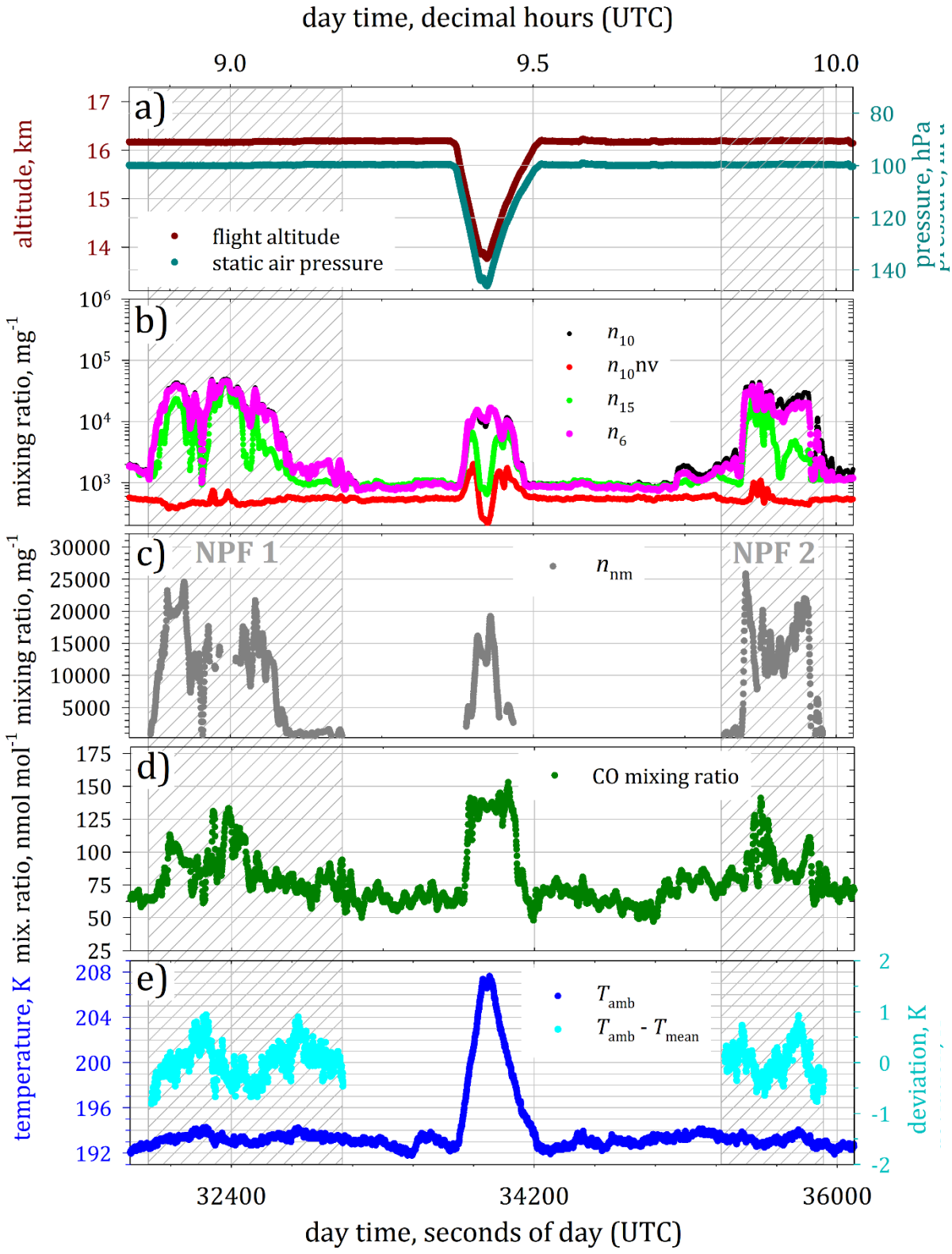
day time, decimal hours (UTC)
9.0
9.5
10.0
a)
altitude, km
pressure, hPa
flight altitude
static air pressure
b)
mixing ratio, mg-1
n_{10}
n_{10}nv
n_{15}
n_6
c)
NPF 1
NPF 2
n_{nm}
d)
CO mixing ratio
e)
temperature, K
mix. ratio, nmol mol-1
deviation, K
T_{amb}
T_{amb} - T_{mean}
32400
34200
36000
day time, seconds of day (UTC)

Figure 13

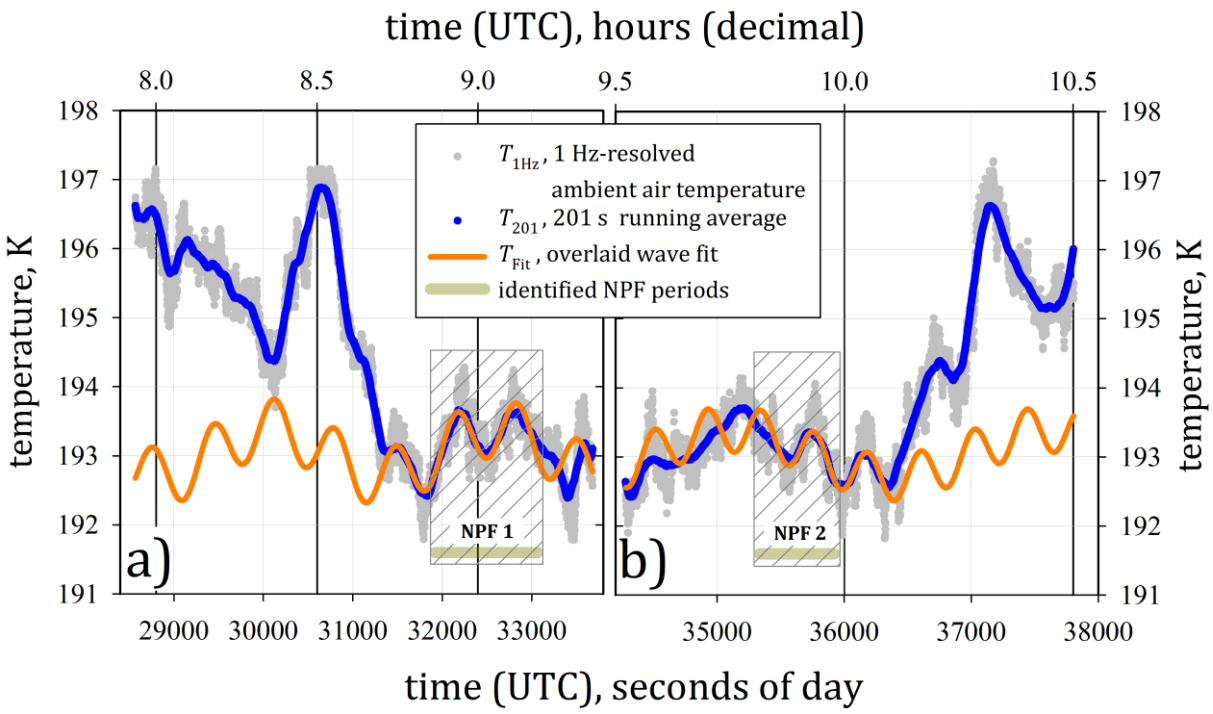
time (UTC), hours (decimal)
8.0
8.5
9.0
9.5
10.0
10.5
198
197
196
195
194
193
192
191
temperature, K
T_{1Hz}, 1 Hz-resolved ambient air temperature
T_{201}, 201 s running average
T_{Fit}, overlaid wave fit
identified NPF periods
NPF 1
NPF 2
a)
b)
29000
30000
31000
32000
33000
35000
36000
37000
38000
time (UTC), seconds of day

Figure 14

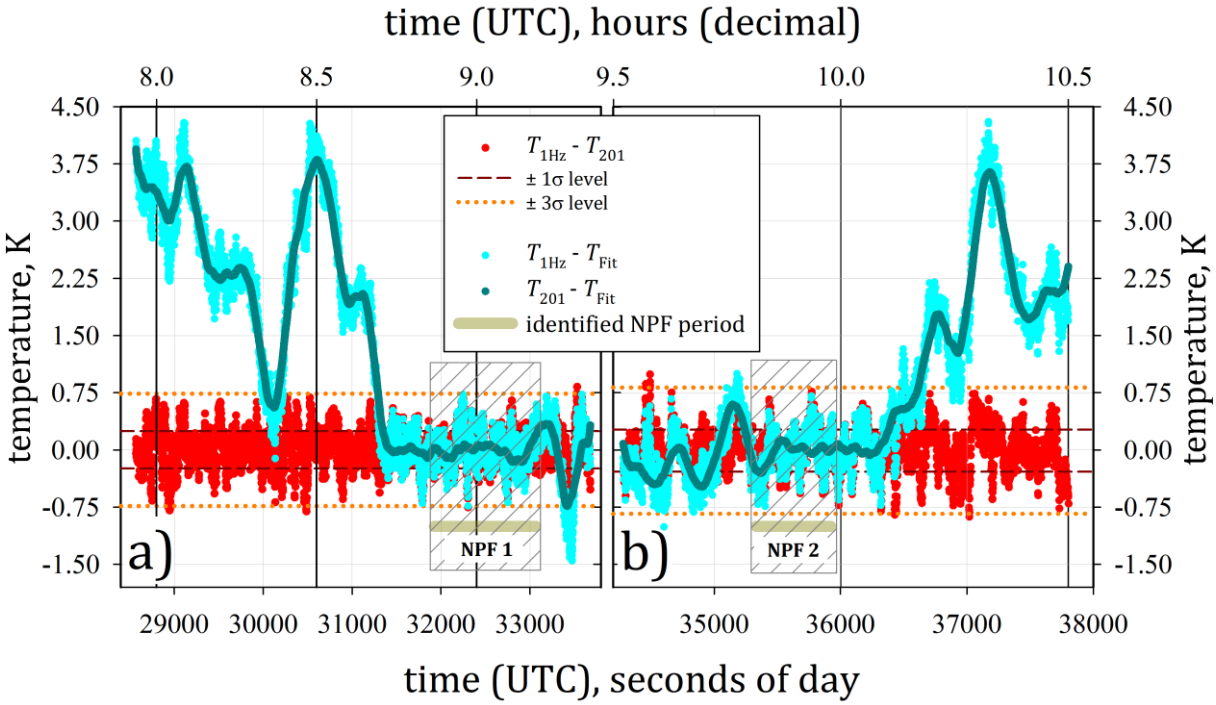
time (UTC), hours (decimal)
8.0
8.5
9.0
9.5
10.0
10.5
4.50
3.75
3.00
2.25
1.50
0.75
0.00
-0.75
-1.50
temperature, K
T_{1Hz} - T_{201}
± 1σ level
± 3σ level
T_{1Hz} - T_{Fit}
T_{201} - T_{Fit}
identified NPF period
a)
b)
NPF 1
NPF 2
29000
30000
31000
32000
33000
35000
36000
37000
38000
time (UTC), seconds of day

Figure A- 1

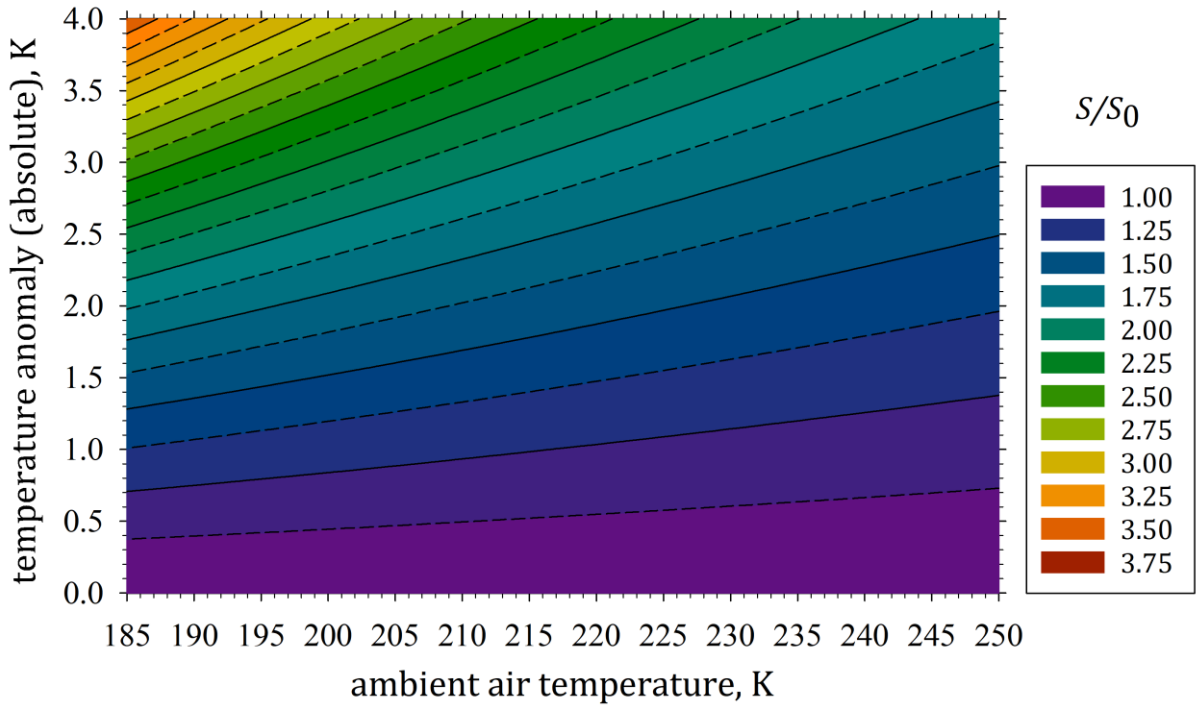
temperature anomaly (absolute), K
4.0
3.5
3.0
2.5
2.0
1.5
1.0
0.5
0.0
185 190 195 200 205 210 215 220 225 230 235 240 245 250
ambient air temperature, K
S/S_0
1.00
1.25
1.50
1.75
2.00
2.25
2.50
2.75
3.00
3.25
3.50
3.75

Figure A- 2

Tables

pressure, hPa	particle diameter, nm										$\bar{\Lambda}_{6\text{-}15}$, %	κ_L (dimensionless)
	6	7	8	9	10	11	12	13	14	15		
	particle size dependent transmission efficiency, %											
80	60	65	70	74	77	79	81	82.5	84	85	**24.25**	1.32
150	70	75	77.5	81	83	84.5	86.5	87.5	88.5	89	**17.75**	1.22
300	77.5	81.5	84	86.5	88	89.5	90.5	91.5	92	92.5	**12.65**	1.14
400	80	83	85	87.5	89	90.5	91.5	92	92.8	93.5	**11.52**	1.13

Table 1

~~Re-calculated p~~Pressure-dependent corrections κ_L for number concentrations of nucleation-mode particles due to particle losses ($\bar{\Lambda}_{6\text{-}15}$) in the aerosol line configuration (both COPAS instruments attached to a single aerosol inlet) as deployed during StratoClim 2017, by using the Particle Loss Calculator (von der Weiden et al., 2009) modified for low pressure applications. $\kappa_L = 100/(100-\bar{\Lambda}_{6\text{-}15})$, correspondingly to Weigel et al. (2009).

	$T_{Fit} = f\,(x,a,b,c,d) + f'\,(x,a',b',c',d')$							
	a	b	c	d	a'	b'	c'	d'
NPF period 1	0.35	0.0025	1.75	193.05	0.42	0.00925	-0.6	0
NPF period 2	0.35	0.0025	1.75	193.05	0.33	0.015	-0.8	0

Table 2

List of parameters of the ~~overlaid~~ wave fit to identify the wave-character of two temperature anomalies, which were coincidently observed with two NPF events, respectively, during the StratoClim flight KTM# 6 on 06 August 2017.